DESIGN AND FABRICATION OF INTEGRATED OPTICAL WAVEGUIDES AND SIDEWALL BRAGG GRATINGS

A Dissertation

by

XIN WANG

Submitted to the Office of Graduate and Professional Studies of
Texas A&M University
in partial fulfillment of the requirements for the degree of

DOCTOR OF PHILOSOPHY

Chair of Committee,	Christi K. Madsen
Committee Members,	Ohannes Eknoyan
	Robert Nevels
	Alexey Belyanin
Head of Department,	Chanan Singh

December 2014

Major Subject: Electrical Engineering

ABSTRACT

In this dissertation, a novel design platform with arsenic tri-sulfide (As_2S_3) on titanium-diffused lithium niobate substrate (Ti:$LiNbO_3$) is introduced to provide physical foundation for integrated optical device applications. $LiNbO_3$ possesses excellent birefringence, electro-optical and acousto-optical effects that enable its high efficiency in nonlinear parametric frequency conversions and flexible tuning capabilities. Secondly, high-quality, low-loss channel waveguide can be made by thin-film metal diffusion or proton exchange with high reproducibility. The mode area size of the channel waveguide is close to single-mode fiber, leading to negligible coupling loss. As_2S_3 has a large index that provides strong mode confinement and tight bending radii for high integration densities. Both materials exhibit broad transparency: 0.4-5.0 μm for $LiNbO_3$ and 0.63-11.0 μm for As_2S_3, making it possible to extend their applications to mid-infrared (3-20 μm) regime.

On this design platform, a hybrid waveguide structure is optimized for efficient mid-infrared radiation at 4.0-4.9 μm by phase-matched difference frequency generation (DFG). The hybrid waveguide is designed for single mode operation. A normalized power conversion efficiency of $20.52\%W^{-1}cm^{-2}$ is theoretically predicted on a 1 mm-long waveguide pumped at 50 mW, which is the highest efficiency record for $LiNbO_3$. Using a tunable pump at 1.38-1.47 μm or signal at 1.95-2.15 μm, a tuning range at 4.0-4.9 μm is achieved. Such hybrid optical waveguides are feasible for mid-infrared emission with mW powers and sub-nanometer linewidths.

Besides, sidewall Bragg gratings in As_2S_3-Ti:$LiNbO_3$ waveguides are fabricated by electron beam lithography and metal liftoff process. Spectrum measurements are in good agreement with numerical fittings. The measured rejection bandwidth is at 2.4-6.7 nm. Coupling coefficients ranging from 2.5 mm^{-1} to 8.9 mm^{-1} are obtained by altering the grating depth. A transmission peak with a 3-dB bandwidth of ~0.25 nm is observed on a 432 μm -long phase-shifted grating. Such integrated sidewall gratings are useful for various optical devices including optical filters, switches, modulators, lasers, sensors, and wavelength division multiplexing (WDM).

In addition, optical refractive index sensors are designed with phase-shifted sidewall gratings in slot waveguide based on silicon-on-insulator (SOI) platform. The designed optical sensors have a minimum detection limit on the order of 10^{-6}, a linear response and a compact device dimension as small as 11.7 μm offering the capabilities for optical sensor array deployment and lab-on-a-chip integration.

DEDICATION

To my family.

ACKNOWLEDGEMENTS

I would like to thank my committee chair and advisor, Dr. Christi K. Madsen, for her superb guidance, utmost encouragement and constant help for my graduate study and research. I would also like to thank my other committee members, Dr. Ohannes Eknoyan, Dr. Alexey Belyanin, and Dr. Robert Nevels, for their time and efforts in guiding and supporting me throughout the course of this research.

I am grateful to my friends and photonic signal processing group members, Xin Xia, W. Tim Snider, Xiaomin Song, Jacob Webb, Yifeng Zhou, Qi Chen, Jae Kim, Ran Huang, Yuxiao Liu, Chen Zhang, and Dwayne Denton for their help and discussions. Thanks to ISSE staff, Larry Rehn, Jim Gardner, Robert Atkins, and Dennie Spears for their help and support, and to Dr. Long Chang at the Nanofabrication Facility Center at University of Houston for fruitful discussions. I also want to extend my gratitude to my friends and colleagues in MIRTHE (Mid-InfraRed Technologies for Health and the Environments), a National Science Foundation Engineering Research Center (NSF-ERC). Thanks to Elaine Lalanne, Hong Cai and Dr. Anthony M. Johnson from UMBC for their help and discussions about experimental measurements for nonlinear wavelength conversions. Thanks to Yu Song, Chao Lu, Dr. Claire Gmachl and Dr. Craig Arnold from Princeton University for their valuable discussions on my research projects at MIRTHE summer workshops.

Finally, special thanks to my parents, my brothers and sister for their support and encouragement and to my girlfriend for her patience and love.

TABLE OF CONTENTS

Page

ABSTRACT ii

DEDICATION iv

ACKNOWLEDGEMENTS v

TABLE OF CONTENTS vi

LIST OF FIGURES viii

LIST OF TABLES xii

CHAPTER

I INTRODUCTION 1

1.1 Background 1
1.2 Motivation 4
1.3 Thesis Organization 7

II THEORETICAL REVIEW 9

2.1 Electromagnetic Theory 9
2.2 Optical Waveguide 14
2.2.1 Step-index waveguide 15
2.2.2 Graded-index waveguide 19
2.2.3 Hybrid waveguide 22
2.2.4 Slot waveguide 24
2.3 Coupled-mode Theory 26
2.4 Transfer Matrix Method 33
2.5 Nonlinear Optics 34
2.6 Electro-optical Effect 39

III FABRICATION PROCESS 43

3.1 Ti-diffused $LiNbO_3$ Waveguide 43

CHAPTER Page

3.2 As_2S_3 Sidewall Bragg Gratings 49
3.3 As_2S_3 Vertical Tapers 58

IV RESULTS AND DISCUSSION 60

4.1 Mid-infrared DFG Waveguides 61
4.1.1 Type-I waveguide design 61
4.1.2 Type-I conversion efficiency 66
4.1.3 Type-IV waveguide design 69
4.1.4 Type-IV conversion efficiency 71
4.2 Sidewall Gratings in As_2S_3-Ti:$LiNbO_3$ Waveguide 77
4.2.1 Design and simulation 77
4.2.2 Experimental measurements 89
4.2.3 Mid-infrared 96
4.3 Sidewall Gratings in SOI Slot Waveguide 100
4.3.1 Sidewall grating in slot waveguide 100
4.3.2 Resonance-shift sensor 108
4.3.3 Intensity-measurement sensor 112

V SUMMARY AND CONCLUSIONS 118

5.1 Summary 118
5.2 Conclusions 120

REFERENCES 123

APPENDIX A 137

LIST OF FIGURES

FIGURE Page

2.1 Reflection and refraction of a plane wave at two dielectric interface 14

2.2 Planar step-index dielectric waveguide with a film thickness of t 15

2.3 Symmetric step-index planar waveguide with $n_1 = n_3$ 18

2.4 Graded-index symmetric planar waveguide 20

2.5 (a) TE and (b) TM mode intensity profiles of Ti:$LiNbO_3$ waveguide 21

2.6 A hybrid optical waveguide with As_2S_3 on Ti-diffused $LiNbO_3$ 22

2.7 Mode intensity profile of a TE-like mode for a hybrid As_2S_3-Ti:$LiNbO_3$ optical waveguide 23

2.8 (a) Horizontal and (b) vertical slot waveguide 25

2.9 (a) Cross-sectional view of silicon-on-insulator slot waveguide superimposed with electric field contours and (b) transverse electrical field distributions 25

2.10 Power transfer as a function of the phase-mismatch 28

2.11 (a) Cross-sectional and (b) top view of sidewall gratings 29

2.12 Grating profiles approximated by harmonic components 31

2.13 Effect of the number of harmonics on coupling coefficient 31

2.14 Effect of the field resolution on coupling coefficient 32

2.15 Evolution of photon flux densities of the signal and up-converted wave 39

2.16 The index ellipsoid for $LiNbO_3$ crystal 40

3.1 Fabrication process for Ti-diffused $LiNbO_3$ waveguide 44

3.2 Configuration of DC/RF magnetron sputtering deposition system 46

3.3 Configuration of electron beam evaporation system [74] 47

3.4 Fabrication process for As_2S_3 sidewall gratings 51

3.5 (a) Before and (b) after tungsten deposition on the samples 53

3.6 Tungsten cross align marks after liftoff process 53

3.7 SEM images for dose test on 3% PMMA resist 55

3.8 SEM images of sidewall gratings after Cr liftoff process 56

3.9 Fabricated (a) As_2S_3 linear tapers and (b) As_2S_3 sidewall gratings 57

3.10 Schematics of self-designed shadow-mask deposition assembly 58

3.11 Measured surface profile of a fabricated vertical taper 59

4.1 Schematics of (a) hybrid As_2S_3-Ti:$LiNbO_3$ waveguide and (b) the equivalent ridge waveguides model 62

4.2 Refractive indices of the waveguide materials 63

4.3 Mode effective indices of the final designed hybrid waveguide 64

4.4 Electric field distributions of (a) pump, (b) signal and (c) idler waves 64

4.5 (a) Dispersion and (b) phase mismatch at different buffer thickness 65

4.6 (a) Power of idler wave and (b) DFG conversion efficiency 68

4.7 Mode intensity profiles of (a) pump, (b) signal and (c) idler waves 69

4.8 Transverse electric field amplitude profiles at different t_2 70

4.9 Effect of the buffer layer thickness on the phase-mismatch 72

4.10 DFG idler power of the designed hybrid waveguide pumped at 50 mW 72

4.11 Tuning mid-infrared idler wave with tunable (a) pump and (b) signal 73

4.12 Conversion efficiency and linewidth of output idler as a function of waveguide length at 50 mW pump powers 74

4.13 (a) Cross-sectional view of hybrid As_2S_3-Ti:$LiNbO_3$ waveguide. (b) Mode intensity profile at 1.55 μm with W_0 = 3.2 μm. (c) Top view of sidewall gratings 78

4.14 (a) Effective indices of As_2S_3 strip and the hybrid As_2S_3-Ti:$LiNbO_3$ waveguide with varying As_2S_3 width. (b) Electric field profiles in two-stage taper. Here L_{t1} = 300 μm, W_{t1} = 0.6 μm, L_{t2} = 100 μm, W_{t2} =1.6 μm; W_1 =3.2 μm, and t =280 nm 79

4.15 Schematics of integrated sidewall gratings in hybrid optical waveguide 81

4.16 Coupling coefficients for various grating profiles 82

4.17 (a) Reflectance and (b) bandwidth under weak coupling 83

4.18 (a) Reflectance and (b) bandwidth under strong coupling 84

4.19 (a) Single and (b) multiple phase-shifted sidewall gratings 85

4.20 Resonant cavities based on sidewall gratings 87

4.21 Illustration of EO-tunable phase-shifted gratings 88

4.22 EO-tunable phase-shifted sidewall gratings 88

4.23 Experimental measurement setup with optical vector analyzer 90

4.24 (a) Measured reflectance at N = 1200. (b) Zoom-in at 1545-1550 nm 91

4.25 (a) Measured reflectance at ΔW = 400 nm. (b) Zoom-in at 1544-1551 nm 92

4.26 Measured bandwidth of fabricated sidewall gratings 93

4.27 Measured transmittance at ΔW = 800 nm 93

4.28 Measured and fitted reflectance at N = 800 and ΔW = 400 nm 94

4.29 Measured and calculated coupling coefficients 95

4.30 Measured reflectance of phase-shifted gratings at ΔW = 800 nm 96

4.31 Intensity mode profile at (a) 1.55 μm and (b) 2.05 μm 97

4.32 Experimental measurement setup at mid-infrared..... 98

4.33 Measured transmittance of mid-infrared Ti waveguide 99

4.34 Fabricated mid-infrared As_2S_3 sidewall gratings on Ti:$LiNbO_3$ 99

4.35 Schematics of (a) slot waveguide and (b) phase-shifted sidewall gratings..... 102

4.36 Effective index of slot waveguide filled with different materials 103

4.37 Transmission spectrum for uniform and phase-shifted sidewall gratings..... 104

4.38 Confinement factor of slot waveguide filled with different materials 105

4.39 Electric field profile of slot waveguide filled with different materials 106

4.40 Coupling coefficients of sidewall gratings in slot waveguide..... 108

4.41 Superimposed transmission spectrum of phase -shifted sidewall gratings 109

4.42 (a) Transmission spectrum and (b) zoom in of transmission peaks for the designed resonance-shift sensor. (c) The resonance peak λ_B as a function of n_{slot} 111

4.43 (a) Coupled phase-shifted sidewall gratings and their transmission spectrum for (b) different L_{gg} with $N = 12$ and (c) different N with $L_{gg} = 2 \cdot L_g$ 113

4.44 (a) Transmission spectrum of the intensity-measurement sensor. (b) Transmission light intensity at reference wavelength λ_R as a function of n_{slot}..... 115

LIST OF TABLES

TABLE		Page
1.1	Optical Waveguides Based on Various Material Platforms	2
4.1	Conversion Efficiencies (CE) of Some Mid-IR DFG Waveguides	75
4.2	Simulation Parameters for Titanium-diffused Waveguides	97
4.3	Performance Parameters of Some Integrated Refractive Index Sensors	11

CHAPTER I

INTRODUCTION

1.1 Background

The study of optics is perhaps one of human's oldest scientific endeavors. Modern interest in light for communications dates from the first demonstration of laser in 1960. This device opened up a new portion of the electromagnetic spectrum with the frequencies 10000 times higher than those in radio communication systems, offering a giant increase in an available bandwidth from 10 GHz to 100 THz. The progressive research and development in low-loss optical fibers, compact single-mode semiconductor lasers, erbium-doped fiber amplifiers, and dense wavelength division multiplexing (DWDM) has led to optical communication systems that can transmit information at a rate of over 100 billion bits per second (100 Gbps) over 80 km with an error rate of only one per billion bits [1].

Driven by the ever-demanding of higher capacity, higher miniaturization and more functionalities, along with the rapid development of micro and nanofabrication technologies, integrated optical devices are attracting more and more attention due to the flexible integration capabilities with other optical, electro-optical, and electrical active and passive components on the same monolithic chip. Some common passive optical components are power splitters, reflectors, switches, couplers, filters, and polarizers. Active optical components include lasers, amplifiers, modulators, photo-detectors, and nonlinear wavelength converters [2, 3]. In particular, optical waveguides are key

components for guiding, coupling and routing in optical communication systems. Different types of material platforms such as silicon-on-insulator (SOI) [4], silicon nitride (SiN) [5], III-V materials such as GaAs and InP [6], chalcogenide glass (ChG) [7], $LiNbO_3$ [8] and polymers [9] are employed to fabricate low-loss optical waveguides at 1.55 μm, as summarized in Table 1.1. Each waveguide has its own benefits. Semiconductor waveguides have much smaller dimensions and higher core confinement due to their larger index contrast. Since the light is much more confined in a smaller area, less scattering loss is induced around sharp bending structures. Polymer and chalcogenide glass (ChG) waveguide can be simply fabricated by nano-imprint lithography, greatly lowering manufacturing cost. Chalcogenide glass waveguides exhibit ultra-low loss in a broad spectrum up to mid-infrared (mid-IR) and a large nonlinear coefficient. High-quality channel waveguide in $LiNbO_3$ can be prepared by thin film titanium-diffusion or annealed proton-exchange process (APE) with an excellent reproducibility. Such channel waveguides possess good thermal-optic, electro-optic tuning capabilities as well as a mode diameter comparable to that of a single-mode fiber (SMF), making the fiber-waveguide coupling loss extremely small (< 0.5 dB/facet).

Table 1.1 Optical Waveguides Based on Various Material Platforms.

	SOI	**SiN**	**III-V**	**Polymer**	**ChG**	**$LiNbO_3$**
Index contrast	~60%	30%	~70%	10%	~20%	< 0.03%
Dimension	~400 nm	< 1 μm	~2 μm	< 3 μm	~3 μm	~8-10 μm
Propagation loss /cm	0.2 dB	0.75 dB	0.5 dB	0.25 dB	0.26 dB	0.3 dB

By combining different materials, hybrid waveguide structures are constructed to realize unique functionalities that cannot be accomplished by a single material platform. For instance, semiconductor laser [10], amplifier [11] and photo-detector [12] have been developed with directed-bonded III-V quantum wells on silicon substrate. Silicon-organic hybrid integration was also reported to enhance optical nonlinearity by eliminating free career generation in silicon [13]. Most recently, arsenic tri-sulfide (As_2S_3) on titanium-diffused $LiNbO_3$ (Ti: $LiNbO_3$) have been demonstrated as a hybrid platform for various integrated optical devices such as low-loss mid-infrared waveguides [14], high-Q microring resonators [15], dispersion-engineered waveguides for four-wave mixing (FWM) [16], integrated sidewall Bragg gratings [17], electro-optic tunable Mach-Zehnder interferometer [18] and linear photonic frequency discriminator [19].

Other than integrated optical waveguides, integrated Bragg gratings are also extensively employed for numerous applications in optical communication and sensing systems. They are found at the transmitting end, receiving end and intermediate points in optical transmission systems. As integrated optical sensors, Bragg grating-based devices exhibit a lot of benefits such as higher sensitivity, larger dynamic range, smaller size and lower cost. Recently, sidewall Bragg gratings integrated in an optical waveguide are drawing plentiful attention due to their strong coupling strength, compactness, lab-on-a-chip integration capabilities, easy control of corrugation, and ease of fabrication. Unlike surface gratings with a fixed grating depth, integrated sidewall gratings with complex grating profiles can be written by a single lithography. Array of such sidewall gratings

can be deployed to implement multiple-channel components for optical communication systems and sensing systems.

1.2 Motivation

Mid-IR lasers with the emission wavelength at 3-20 μm are critical components for a diverse array of applications such as remote trace gas sensing, free space communication, industrial process monitoring, medical diagnostics, chemical analysis, and high-resolution spectroscopy. Therefore, the research on novel efficient mid-IR emission is quire desired. Numerous approaches are developed for efficient mid-IR emission; nevertheless, each approach has its own drawbacks. Gas lasers (CO, CO_2) have an incomplete spectral coverage, limiting their sensing applications [20]. Lead salt diode lasers and lead-chalcogenide vertical external cavity surface emitting lasers (VECSELs) usually produce low power levels and rely on the cryogenic cooling for continuous-wave (CW) operation [21, 22]. Based on semiconductor heterostructures, rapid progress is being made in the development of quantum cascade lasers (QCLs) and interband cascade lasers (ICLs); however, challenges still exist in design, growth, processing, room-temperature operation and packaging of these semiconductor injection lasers [23-26]. As a viable alternative, nonlinear optical frequency down-conversion based on difference frequency generation (DFG) in phase-matched optical waveguides can be employed for efficient mid-IR emission [27-32]. In DFG, an idler wave at mid-IR is generated from pump and signal waves at near-infrared (near-IR). As a result of continuing improvements of high-power tunable near-IR lasers in conjugation with the

optical nonlinear materials, CW tunable mid-IR lasers can be configured so as that the high performance characteristics of near-IR lasers such as precise wavelength resolution, narrow emission linewidth, and large tuning range can be transferred to the mid-IR idler output [33]. Based on the above As_2S_3 on Ti-diffused $LiNbO_3$ platform, a novel hybrid waveguides were designed for efficient mid-infrared emission at 4.0-4.9 μm via phase-matched DFG with two near-infrared pump waves.

Fabrication and measurement of sidewall gratings integrated in different types of waveguide, including silicon nanowire [34], slot waveguide [35], ridge waveguide [36], low-loss silicon nitride waveguide [37] and polymer waveguide [38], have been reported. Although the fabrication for both As_2S_3 waveguide and Ti waveguide has been well established, little attention is paid to writing integrated As_2S_3 sidewall gratings on Ti-diffused $LiNbO_3$. Unlike aforementioned hybrid waveguide devices where lateral gaps between Ti waveguide and As_2S_3 strips were introduced to enhance side-coupling for adiabatic tapers [15, 18, 19], double-side corrugated As_2S_3 strips (i.e., sidewall gratings) were precisely aligned, with the assistance of tungsten align marks, down the midline of Ti-diffused waveguide for optimal mode confinement for the hybrid optical waveguide. In this dissertation, the design, fabrication and measurement of integrated sidewall Bragg gratings based on the hybrid As_2S_3 on Ti-diffused $LiNbO_3$ platform were discussed in details. Spectral response of uniform sidewall gratings, phase-shifted sidewall gratings, optical cavities formed by two sidewall gratings were systematically analyzed with coupled-mode theory and transfer matrix method. The coupling

coefficients, reflection bandwidth and electro-optical tuning properties of such sidewall gratings were also discussed.

Optical sensors play critical roles in biomedicine, forensic diagnostics, microbiology, drug screening, environment monitoring, and food quality control. Huge progress is being made in integrated optical sensors based on silicon planar waveguides, which can be fabricated by CMOS-compatible technologies allowing for mass production. Different sensing mechanisms such as interferometers [39, 40], surface plasmon resonances (SPRs) [41, 42], guided-mode resonances (GMRs) [43-45], photonic crystals (PCs) [46], integrated Bragg gratings in waveguide [47, 48] and microring resonators [49-51] are reported. Although conventional strip or rib waveguides are commonly used in these optical sensors, slot waveguide, formed by placing two strip waveguides in parallel with a nanometer gap, has drawn more and more interests due to its high confinement of electric field in low-index materials [52-54]. In fact, a great variety of optical devices utilizing slot waveguide structure have been designed and proposed, which include directional couplers [55], optical modulators [56], optical switches [57], electrically pumped light-emitting devices [58] and microring resonators [59]. In particular, optical label-free sensing based on single slot waveguide [60], multiple slot waveguides [61], bent slot waveguide [62] and slot waveguide microring resonator [63-66] have also been reported. In this dissertation, two compact refractive index sensors based on the phase-shifted sidewall Bragg gratings in slot waveguide were designed with transfer matrix method [67]. It was theoretically demonstrated that such refractive index sensors have a high sensitivity, a linear response over a wide detection range, and a

compact device dimension as small as 11.7 μm, offering the capabilities for integration with other electronics, sources and detectors on a same monolithic chip [66, 68].

To briefly summarize, this dissertation covers the design of novel hybrid waveguides for efficient mid-infrared emission by phase-matched difference frequency generation. Fabrication and measurement of integrated sidewall gratings are discussed in details. Two types of compact optical refractive index sensors with high sensitivity and wide dynamic range are proposed based on phase-shifted sidewall gratings in silicon-on-insulator (SOI) slot waveguide.

1.3 Thesis Organization

Following the introduction in Chapter I, the electromagnetic principles integrated optical waveguides, coupled-mode theory, transfer matrix method, nonlinear optical wavelength conversion by four-wave mixing and difference-frequency generation, and experimental measurement setups are briefly reviewed in Chapter II. These provide the theoretical foundations for the design of integrated optical waveguides and sidewall Bragg gratings in what follows.

In Chapter III, the fabrication processes for Ti-diffused $LiNbO_3$ waveguide by photolithography, As_2S_3 sidewall gratings by electron-beam lithography and metal liftoff, and As_2S_3 vertical tapers by shadow mask sputtering deposition were introduced. Tungsten crosses, revealed by metal liftoff, were used for layer-to-layer alignment purpose during electron-beam lithography. The dosage and baking condition of positive-tone electron beam resist (3% PMMA) were optimized to obtain smooth sidewalls.

In Chapter IV, a novel hybrid waveguide design for efficient mid-infrared emission by modal phase-matched difference frequency generation was firstly investigated. The maximum power conversion efficiency was theoretically predicted by taking waveguide loss into account. Experimental measurement results on fabricated integrated sidewall gratings were then presented, followed by detailed discussion and analysis. Finally, two compact highly-sensitive optical refractive index sensors based on phase-shifted sidewall gratings in silicon slot waveguide were proposed.

A brief summary and conclusion of this dissertation were given in Chapter V.

CHAPTER II

THEORETICAL REVIEW

2.1 Electromagnetic Theory

The behaviors of electromagnetic waves are governed by electromagnetism theory if quantum effects are negligible. To analyze wave propagation and its interaction with a medium, we begin with a statement of Maxwell's equations in differential form [3].

$$\nabla \times E(r,t) = -\frac{\partial}{\partial t} B(r,t) \tag{2.1}$$

$$\nabla \times H(r,t) = \frac{\partial}{\partial t} D(r,t) + J(r,t) \tag{2.2}$$

$$\nabla \cdot D(r,t) = \rho(r,t) \tag{2.3}$$

$$\nabla \cdot B(r,t) = 0 \tag{2.4}$$

In the above equations, ***E*** and ***H*** represent, respectively, the electric and magnetic fields, and ***D*** and ***B*** the electric and magnetic displacements. ***J*** and $\boldsymbol{\rho}$ are the current and charge sources. The position vector ***r*** defines a particular location in space (*x, y, z*) at which the field is being measured. An auxiliary continuity equation that relates the current and charge sources ***J*** and $\boldsymbol{\rho}$ is shown in Eq. (2.5).

$$\nabla \cdot J(r,t) + \frac{\partial}{\partial t} \rho(r,t) = 0 \tag{2.5}$$

It is noted that Eq. (2.1)-(2.4) are not all independent. Indeed, only Eq. (2.1), (2.2), and (2.5) are needed to derive Eq. (2.3) and (2.4) by taking the divergence of Eq. (2.1), and (2.2). Eq. (2.1) describes Faraday's law of induction where electric field is induced

from time-varying magnetic fields, while Eq. (2.2) explains Ampere's law with Maxwell's addition where magnetic field is induced from electric currents and time-varying electric field. Eq. (2.3) and Eq. (2.4) describe, respectively, Gauss's law and Gauss's law for magnetism where electric fields emanate from electric charges and magnetic fields as closed field lines not due to magnetic monopoles [69].

Additional constraints provided by constitutive relations are needed to solve the Maxwell's equations. These constitutive relations characterize a given material on a macroscopic level and are expressed in terms of permeability μ and permittivity ε.

$$D(r,t) = \varepsilon E(r,t) + P(r,t) \tag{2.6}$$

$$H(r,t) = \frac{1}{\mu} B(r,t) - M(r,t) \tag{2.7}$$

Where $\boldsymbol{P}$ is the polarization field and $\boldsymbol{M}$ is the magnetization field, which are defined in terms of microscopic found charges and bound current, respectively [69]. Considering a special case in the absence of magnetic or dielectric materials, the constitutive relations are simple:

$$D = \varepsilon_0 E; \quad H = \frac{1}{\mu_0} B \tag{2.8}$$

Where $\mu_0 = 4\pi\times10^{-7}$ H/m, and $\varepsilon_0 = 8.85\times10^{-12}$ F/m are vacuum permeability and vacuum permittivity, respectively.

In an isotropic linear material where $\boldsymbol{P}$ is proportional to $\boldsymbol{E}$, and $\boldsymbol{M}$ is proportional to $\boldsymbol{B}$, the constitutive relations are also straightforward and related to the susceptibility χ of the material.

$$D = \varepsilon_0(\chi+1)E; \quad H = \frac{1}{\mu_0(\chi+1)}B \tag{2.9}$$

Assume source-free isotropic media and $\boldsymbol{E}$ and $\boldsymbol{B}$ are time-harmonic fields that vary at a sinusoidal frequency ω, the partial derivative $\partial/\partial t$ in Maxwell's equations can be simply replaced by $j\omega$. This leads to vector wave equation that represents three equations of identical form, one for each component of the $\boldsymbol{E}$ field. For example, the $\boldsymbol{E_x}$ component satisfies Eq. (2.10).

$$\left(\frac{\partial^2}{\partial x^2}+\frac{\partial^2}{\partial y^2}+\frac{\partial^2}{\partial z^2}\right)E_x(r)-\omega^2\mu\varepsilon E_x(r)=0 \tag{2.10}$$

A possible plane-wave solution to Eq. (2.10) is of the form

$$E_x(r) = E_{x0}e^{-j(k_x x+k_y y+k_z z)} \tag{2.11}$$

where $\boldsymbol{E_{x0}}$ is an arbitrary constant. Since all three components of the $\boldsymbol{E}$ field satisfy Eq. (2.12), substitution of their solutions yields the dispersion relation.

$$k_x^2+k_y^2+k_z^2=\omega^2\mu\varepsilon\equiv k^2 \tag{2.12}$$

Here, $\boldsymbol{k} = 2\pi/\lambda$ is called wave vector with λ denoting the wavelength. Without loss of generality, assume the electric field along z-axis, so that $\boldsymbol{k} = \boldsymbol{k_z}$.

$$E(z,t) = E_0e^{-j(\omega t-kz)} \tag{2.13}$$

Then, the phase velocity is defined by

$$v\equiv\frac{dz}{dt}=\frac{\omega}{k}=\frac{1}{\sqrt{\mu\varepsilon}} \tag{2.14}$$

In free space, the phase velocity is equal to the speed of light, $c = 2.99795\times10^8$ m/s. In a medium, the phase velocity is characterized by its refractive index n or relative permittivity ε_r.

$$v = \frac{c}{n} = \frac{\sqrt{\mu_0\varepsilon_0}}{\sqrt{\mu\varepsilon}}c = \frac{c}{\sqrt{\varepsilon_r}} \tag{2.15}$$

Poynting vector $\boldsymbol{S}$ is defined, in Eq. (2.16), to represent the magnitude and direction of the power flux at any point. It has the unit of power per unit area. Poynting's theorem is interpreted as follows: The power generated within an arbitrary volume V minus conduction losses is equal to the time rate of increase of stored energy within V plus the net power flowing out of V throughout the surface [3].

$$S \equiv E \times H \tag{2.16}$$

Absorption of light by a medium is characterized by a complex refractive index with the imaginary part representing the loss coefficient. The intensity of light propagating through the medium follows Beer-Lambert law in Eq. (2.21).

$$\tilde{n} = n + j\alpha \tag{2.17}$$

$$I = \left|E_0\right|^2 \exp(-\frac{2n\omega\alpha}{c}z) \tag{2.18}$$

Any integrated-optics components must have physical dimensions of finite extent; and this geometry is described by the distribution of dielectric constant or refractive index. To understand how a component operates, we must know how spatial variation in dielectric constant modifies the properties of optical radiation. Therefore, materials dispersion and boundary conditions at two dielectric interfaces need to be considered.

The material dispersion is caused by the nature of wavelength dependence of refractive index, which can be modeled by Sellmeier Equation, given as

$$n^2(\lambda) = 1 + \sum_i \frac{B_i \lambda^2}{\lambda^2 - C_i} \tag{2.19}$$

where B_i and C_i are experimentally determined Sellmeier coefficients. For many common optical materials, such coefficients can be found in the online database [70].

The boundary conditions that relate the fields across the interface of two dielectric media are given by Eq. (2.20). We can conclude that the tangential components of $\boldsymbol{E}$ and $\boldsymbol{H}$ must be continuous across the dielectric interface at all points along the boundary.

$$\begin{aligned} \hat{n} \cdot (B_1 - B_2) = 0; \quad & n \cdot (D_1 - D_2) = 0 \\ \hat{n} \times (E_1 - E_2) = 0; \quad & n \times (H_1 - H_2) = 0 \end{aligned} \tag{2.20}$$

The reflection and refraction of incident wave can be explained using the boundary conditions. Consider a plane wave propagating through a half-space characterized by μ_1, ε_1 and incident upon an interface with another half-space region denoted by μ_2 and ε_2, as illustrated in Fig. 2.1. The incident, reflected and transmitted wave electric fields are:

$$E_{i,r,t}(r) = A_{i,r,t} \exp(-jk_{i,r,t} \cdot r) \tag{2.21}$$

$$k_i = k_r = \omega\sqrt{\mu_1 \varepsilon_1} \; ; k_t = \omega\sqrt{\mu_2 \varepsilon_2} \tag{2.22}$$

Tangential component of the incident, reflected and refracted wave vectors are same,

$$k_i \sin(\theta_i) = k_r \sin(\theta_r) = k_t \sin(\theta_t) \tag{2.23}$$

Combining Eq. (2.22) and (2.23) yields

$$\theta_i = \theta_r \tag{2.24}$$

$$\frac{\sin(\theta_i)}{\sin(\theta_t)} = \sqrt{\frac{\mu_2 \varepsilon_2}{\mu_1 \varepsilon_1}} = \frac{n_2}{n_1} \tag{2.25}$$

Equation (2.25) is known as Snell's law. When light is incident from a high-index medium to a low- index medium ($n_1 > n_2$), if the incident angle is larger than a critical value (i.e., $\theta_i \geq \theta_c$), no light is transmitted and the light is totally reflected back into the high-index medium, this is referred to total internal reflection, the mechanism of guiding the light in optical waveguides. The critical angle required for total internal reflection is given as

$$\theta_c = \sin^{-1}\left(\frac{n_2}{n_1}\right). \tag{2.26}$$

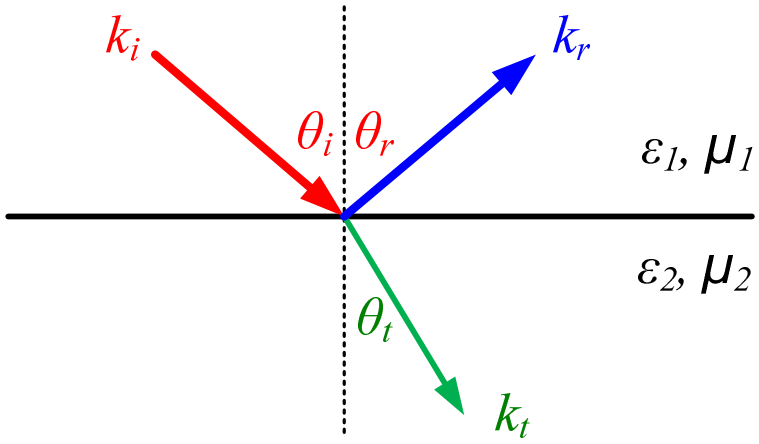

Fig. 2.1. Reflection and refraction of a plane wave at two dielectric interface.

2.2 Optical Waveguide

As the key component in integrated optical circuits as the transmission medium in local and long-haul optical communication systems, an optical waveguide is a physical

structure that guides electromagnetic waves within the optical spectrum. Optical waveguide can be classified according to their geometry (planar, strip, ridge, slot), mode pattern (single-mode, multi-mode), distribution of refractive index (step-index, gradient index), and material (glass, polymer, semiconductor).

2.2.1 Step-index waveguide

Simplest planar optical waveguide is a step-index dielectric waveguide that consists of a high-index layer sandwiched by two low-index regions, as illustrated in Fig. 2.2. Generally, we have $n_2 > n_3 > n_1$. If $n_1 = n_3$, it is symmetric, otherwise it is asymmetric. Assume lossless, isotropic and homogeneous material in absence of source, the allowed mode can be determined using the Wave Equation in Eq. (2.10).

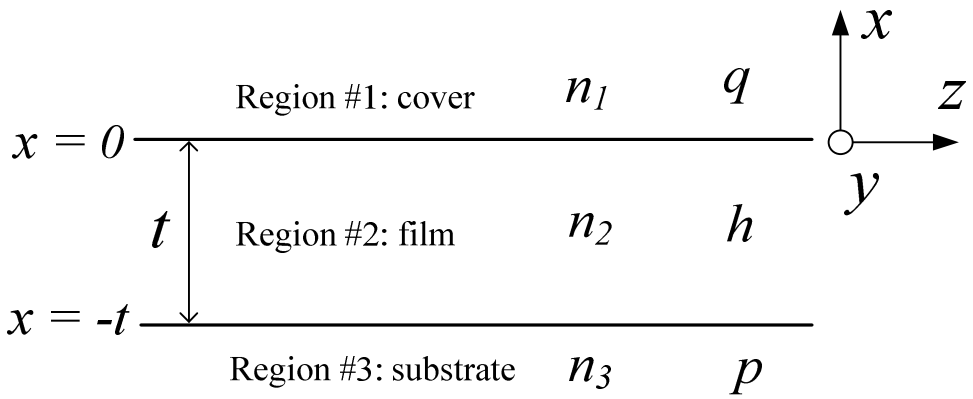

Fig. 2.2. Planar step-index dielectric waveguide with a film thickness of t.

Define the wave vector in vacuum as $k_0 = \omega/c$, and consider the propagating wave in infinite directions along y-axis and z-axis

$$E(r) = E(x, y)e^{j\beta z} \tag{2.27}$$

The wave equation in all three directions becomes

$$\frac{\partial^2 E(x)}{\partial x^2} + (k_0 n_i^2 - \beta^2) E(x) = 0 \tag{2.28}$$

If the electric field ***E*** is parallel to *y*-axis, this mode is called transverse electric (TE) mode or TE-polarized. If the magnetic field ***H*** is parallel to *y*-axis, the mode is called transverse magnetic (TM) mode or TM-polarized.

For TE polarization, plug in $\boldsymbol{E} = \boldsymbol{E_y(x)}$ in Eq. (2.28). If $n_2 > n_3 > n_1$ is fixed for a given angular frequency, only variable is β. Thus, the behavior of shapes of electric field $\boldsymbol{E_y(x)}$ depends on the value of $k_0 n_i$ relative to β. Only discrete values of β give oscillatory distribution in Region #2 and evanescent wave in Region #1 and #3, each β indicates an allowed mode for guided propagation in the waveguide. For guided mode propagation, $k_0 n_3 < \beta < k_0 n_2$ has to be satisfied.

Define

$$q \equiv (\beta^2 - k_0^2 n_1^2)^{1/2};\ h \equiv (k_0^2 n_2^2 - \beta^2)^{1/2};\ p \equiv (\beta^2 - k_0^2 n_3^2)^{1/2} \tag{2.29}$$

Then, the solution to Eq. (2.28) is of the form

$$E_y(x) = \begin{cases} Ae^{-qx} & x > 0 \\ B\cos(hx) + C\sin(hx) & 0 \geq x \geq -t \\ De^{p(x+t)} & x < -t \end{cases} \tag{2.30}$$

Using the boundary conditions at interfaces $x = 0$ and $x = -t$, it yields

$$E_y(x) = \begin{cases} C'e^{-qx}, & x > 0 \\ C'[\cos(hx) - \frac{q}{h}\sin(hx)], & 0 \geq x \geq -t \\ C'[\cos(ht) + \frac{q}{h}\sin(ht)]e^{p(x+t)}, & x < -t \end{cases} \tag{2.31}$$

The constant C' is determined by the convention that one unit power (1 Watt) is used per unit meter (1 Meter) width along *y*-axis

$$P_z = \frac{1}{2}\frac{\beta}{\omega\mu}\int_0^1 dy \int_{-\infty}^{\infty} \left|E_y(x)\right|^2 dx = 1 \text{ Watt} \tag{2.32}$$

The characteristic equation (or eigenvalue equation) is also derived from boundary conditions

$$\tan(ht) = \frac{p+q}{h-\frac{pq}{h}} \tag{2.33}$$

Note only discrete values of h (i.e., eigenvalue) are allowed in Eq. (2.39) and thus discrete β values are allowed. Each β value determines a mode denoted by subscript m. Effective mode index is defined as $n_{eff} = \beta_m/k_0$. Each mode has own C' value

$$C'_m = 2h_m\sqrt{\frac{\omega\mu}{\left|\beta_m\right|(h_m^2+q_m^2)(t+1/q_m+1/p_m)}} \tag{2.34}$$

For TM polarization, plug in $\boldsymbol{H} = \boldsymbol{H_y(x)}$ to Eq. (2.10), the solution is

$$H_y(x) = \begin{cases} -C''e^{-qx}, & x > 0 \\ C''[-\frac{h}{q}\cos(hx)+\sin(hx)], & 0 \geq x \geq -t \\ -C''[\frac{h}{q}\cos(ht)+\sin(ht)]e^{p(x+t)}, & x < -t \end{cases} \tag{2.35}$$

Where

$$C'' = 2\sqrt{\frac{\omega\varepsilon_0}{\beta t'}} \tag{2.36}$$

$$t' = \frac{\left(\frac{n_2^2}{n_1^2}q\right)^2 + h^2}{\left(\frac{n_2^2}{n_1^2}q\right)^2}\left[\frac{t}{n_2^2} + \frac{\frac{q^2+h^2}{n_1^2 q}}{\left(\frac{n_2^2}{n_1^2}q\right)^2 + h^2} + \frac{\frac{p^2+h^2}{n_3^2 p}}{\left(\frac{n_2^2}{n_3^2}p\right)^2 + h^2}\right] \tag{2.37}$$

The characteristic equation is

$$\tan(ht) = \frac{\frac{n_2^2}{n_3^2}p + \frac{n_2^2}{n_1^2}q}{h - \left(\frac{n_2^2}{n_3 n_1}\right)^2 \frac{pq}{h}} \tag{2.38}$$

For a symmetric planar waveguide ($n_1 = n_3 < n_2$), as shown in Fig. 2.3, the axis of the waveguide structure symmetry is used as coordinate system.

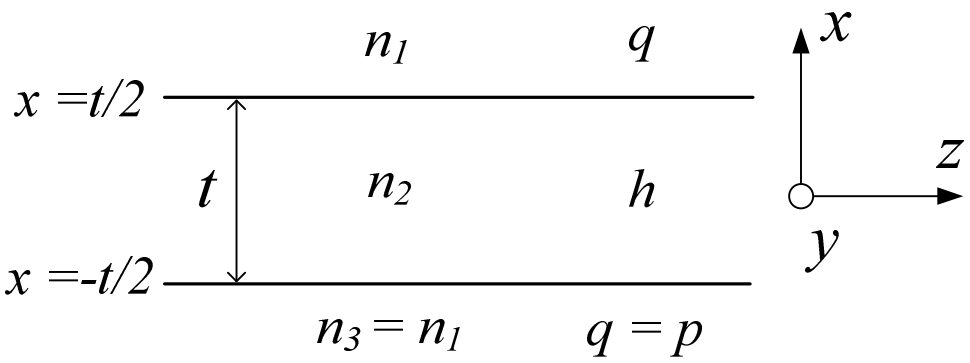

Fig. 2.3. Symmetric step-index planar waveguide with $n_1 = n_3$.

The TE polarization solution is

$$E_y(x) = \begin{cases} A' e^{-q(x-t/2)} & x > \dfrac{t}{2} \\ A' \dfrac{\cos(hx)}{\cos(ht/2)} \text{ or } A' \dfrac{\sin(hx)}{\sin(ht/2)} & \dfrac{t}{2} \geq x \geq -\dfrac{t}{2} \\ \pm A' e^{q(x+t/2)} & x < -\dfrac{t}{2} \end{cases} \tag{2.39}$$

Here *cos(hx)* and "+" sign are adopted for even modes (*m = 0, 2, 4, ⋯*), while *sin(hx)* and "-" sign are used for odd modes (*m = 1, 3, 5, ⋯*). The field amplitude constant is

$$A' = 2\sqrt{\frac{\omega\mu}{\beta(t + 2/q)}} \tag{2.40}$$

The characteristic equation is

$$\tan(h\frac{t}{2}) = \begin{cases} +\dfrac{q}{h} & \text{(even modes)} \\ -\dfrac{h}{q} & \text{(odd modes)} \end{cases} \tag{2.41}$$

Alternatively, the characteristic equation for uniform step-index waveguides can also be represented by Eq. (2.42) where ψ_{21} and ψ_{23} indicate the phase changes experienced at upper and lower interfaces.

$$2h_m t + \psi_{21} + \psi_{23} = 2m\pi \quad (m = 0, 1, 2, \cdots) \tag{2.42}$$

2.2.2 Graded-index waveguide

Fig. 2.4 shows a symmetric graded-index planar waveguide with a varying index distribution along *x*-axis: $n_2 = n_2(x)$. This makes it difficult to identify abrupt boundary conditions. Consequently, the closed-form of characteristic equation becomes an integral equation where $x_{t\pm}$ are turning points for total internal reflection.

$$2\int_{x_{t-}}^{x_{t+}} \sqrt{k_0^2 n_2^2(x) - \beta_m^2}\, dx + \psi_{21} + \psi_{23} = 2m\pi \quad (m = 0, 1, 2, \cdots) \tag{2.43}$$

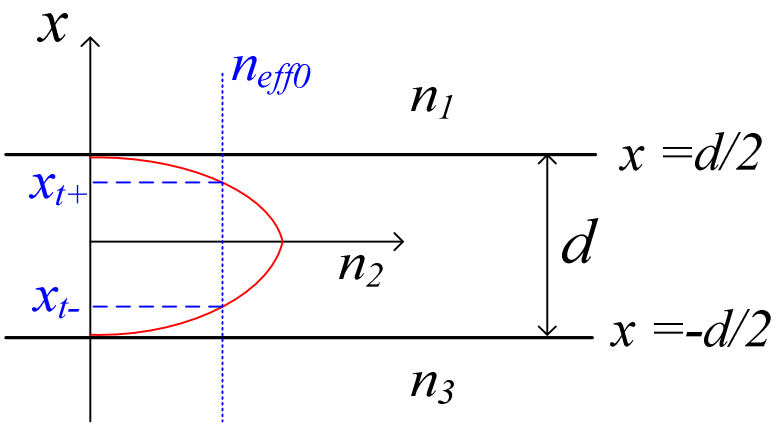

Fig. 2.4. Graded-index symmetric planar waveguide.

Ti-diffused $LiNbO_3$ waveguides are good examples of the graded-index waveguides with refractive index varying along both vertical and horizontal directions. Assuming anisotropic diffusion on a *x*-cut, *y*-propagation substrate, the 2D refractive index *n(x,z)* is given by

$$n^2(x,z) = n_b^2 + [n_s^2(z) - n_b^2] \cdot f(\frac{x}{D}) \cdot g(\frac{2z}{w}) \tag{2.44}$$

Here, n_b and n_s are the bulk index and surface index, respectively; *f(x)* is Gaussian function and *D* is the diffusion depth; *g(z)* is error function and *w* is the strip width before diffusion. The maximum index change is on the surface and the optical mode is confined in the diffusion region. The bulk refractive index is 2.28 for ordinary refractive index (*y*-axis) at 1550 nm wavelength and is 2.13 for extraordinary refractive index (*z*-

axis). Note that the index distribution is Gaussian along x-axis, but surface index is not constant because of isotropic sideway diffusion. The eigenvalue integral equation is

$$k_0(n_0^2-n_b^2)\int_{z_{t-}}^{z_{t+}}\sqrt{\frac{[n_{eff}^2(z)-n_b^2](n_0^2-n_b^2)}{(n_s^2-n_b^2)^2}-\frac{(n_{eff}^m)^2-n_b^2}{n_0^2-n_b^2}}dz=(m+\frac{1}{2})\pi \qquad (2.45)$$

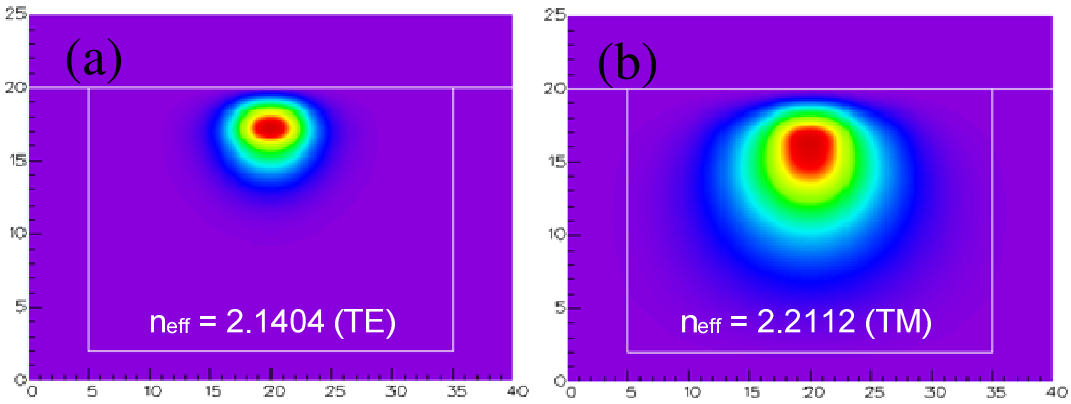

Fig. 2.5. (a) TE and (b) TM mode intensity profiles of Ti:$LiNbO_3$ waveguide.

Figure 2.5 plots mode intensity profiles, calculated by commercial software Fimmwave, for Ti-diffused waveguides on x-cut y-propagating $LiNbO_3$ substrate. In calculation, the width and thickness of Ti strip before diffusion are w = 7 μm and t = 95 nm. Assuming the diffusion is performed at 1025 ºC for 10.5 hours, the resulting vertical and horizontal diffusion depths are 5.37 μm and 4.46 μm, respectively. The effective indices of fundamental mode (m = 0) are 2.1404 for TE and 2.2112 for TM at 1.55 μm. Note that TM mode area is significantly larger than TE mode.

2.2.3 Hybrid waveguide

Hybrid waveguides are constructed by combining waveguides of different materials in order to accomplish more desirable functionalities such as flexible tuning, efficient coupling, dispersion engineering, and nonlinear process enhancement. Fig. 2.6 shows an example of hybrid waveguide made by chalcogenide As_2S_3 on Ti-diffused $LiNbO_3$.

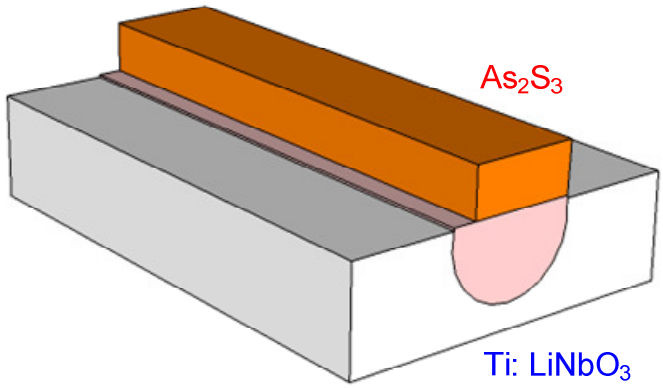

Fig. 2.6. A hybrid optical waveguide with As_2S_3 on Ti-diffused $LiNbO_3$.

The advantages of this hybrid waveguide are manifold. First, $LiNbO_3$ exhibits excellent birefringence, thermal-optic and electro-optical properties. Second, high-quality channel waveguide can be fabricated by titanium diffusion or annealed proton exchange process. The mode size of such channel waveguides is comparable to a single mode fiber, leading to negligible fiber-coupling loss. Third, As_2S_3 possesses a large index contrast that provides strong mode confinement and tight bend radii for high integration densities. Finally, both materials have broad transparency spectrum up to

mid-infrared: 0.4-5 μm for $LiNbO_3$, 0.63-11 μm for As_2S_3, making them attractive for mid-infrared applications.

In contrast to the Ti-diffused channel waveguide and As_2S_3 rectangular waveguide, the modes in hybrid waveguides are much more complicated due to interactions between modes supported by each individual waveguide. The modes in a hybrid waveguide are no longer pure TE or TM, but a mixture of TE and TM. Rigorous analysis on interacting modes may be conducted by supermode theory [71].

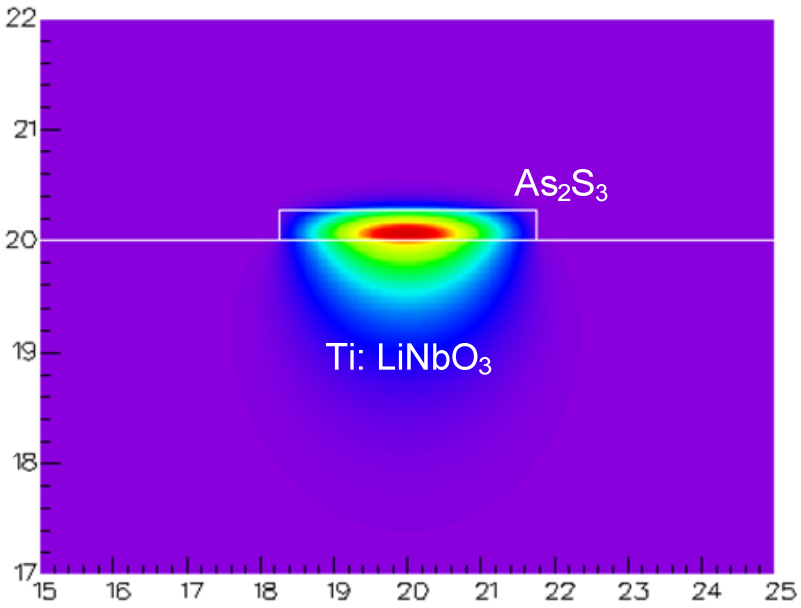

Fig. 2.7. Mode intensity profile of a TE-like mode for a hybrid As_2S_3-Ti:$LiNbO_3$ optical waveguide.

Figure 2.7 displays the mode intensity profile of the fundamental mode (TE-like or quasi-TE) at 1.55 μm from such a hybrid waveguide with As_2S_3 on Ti-diffused $LiNbO_3$. The width and height of As_2S_3 ridge on top are, respectively, 3.5 μm and 0.28 μm. The

effective index is 2.1548, slightly larger than that of Ti: $LiNbO_3$ waveguide. It is clear that only partial of mode intensity (~30% for this particular case) is confined in the high-index As_2S_3 ridge region; the rest of light intensity is confined in the Ti-diffused region. This feature facilitates the tuning capabilities with thermal-optic and electro-optic (EO) properties of $LiNbO_3$. For instance, EO-tunable Mach-Zehnder interferometer with a tuning rate of 28 pm/V was demonstrated [18]. An electro-optical tuning rate at 5 pm/V for As_2S_3 sidewall gratings integrated on Ti:$LiNbO_3$ waveguide was also theoretically predicted [17].

2.2.4 Slot waveguide

A slot waveguide is formed by placing two strip waveguide in parallel with a nanometer gap or slot in between. According to boundary conditions, the electric field amplitude in low-index slot region is much larger that in high-index region. As a result, high index-contrast materials such as silicon-on-insulator (SOI) are favored by such slot waveguides. Depending on the slot geometry, there are two types of slot waveguides as shown in Fig. 2.8. Quasi-TM modes have stronger confinement in horizontal slot waveguide while quasi-TE modes are more strongly confined in vertical slot waveguide. In practical applications, the slot is more often filled or loaded with some fluidic media to assist dispersion engineering, enhance mode confinement and reduce scattering losses. Or the slot is used a fluidic channel for the materials to be sensed or analyzed.

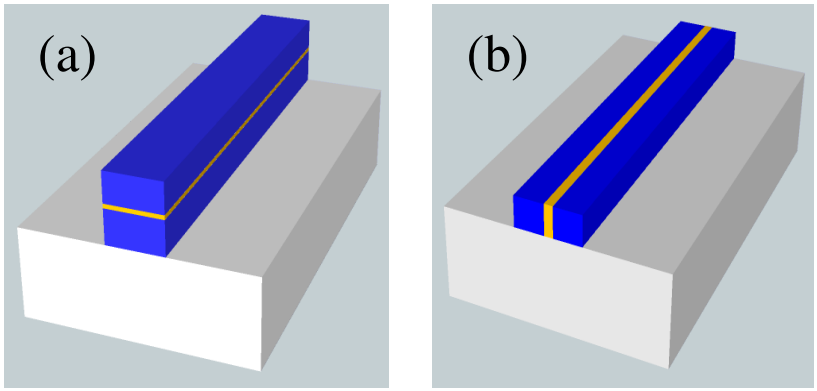

Fig. 2.8. (a) Horizontal and (b) vertical slot waveguide.

As seen in Fig. 2.9, the electric field is greatly enhanced and concentrated in the low-index slot region as expected, making it extremely sensitive to the refractive index of the slot medium. In this dissertation, two highly sensitive optical refractive index sensors with a compact dimension are designed using such slot waveguides.

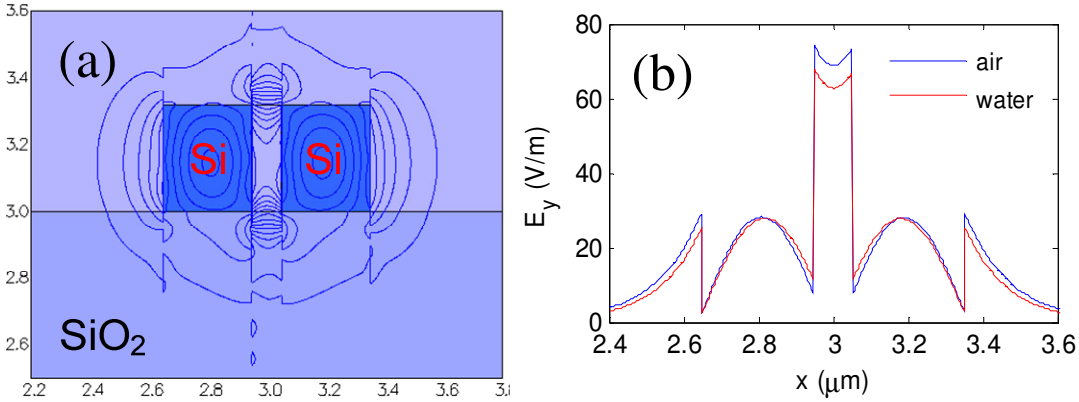

Fig. 2.9. (a) Cross-sectional view of silicon-on-insulator slot waveguide superimposed with electric field contours and (b) transverse electrical field distributions.

2.3 Coupled-mode Theory

In practical applications, an exterior light beam should be efficiently launched into an optical waveguide, which is called optical coupling. Both transverse coupling (butt coupling, endfire coupling) and surface coupling (prism coupling, grating coupling) are use in integrated optics. Coupled-mode theory (CMT) explains the coupling behaviors of spatial modes. To enhance coupling efficiency, the field amplitude distributions should spatially overlap as well as possible, which usually involves continuity conditions at interfaces, mode orthogonality relations and strong mode confinement assumption. The power coupling efficiency between two waveguide modes β_1 and β_2 is given by Eq. (2.16), where the first factor is for Fresnel reflection (β-mismatch) and the second factor is for mode-mismatch (overlap integration).

$$\eta = \frac{4\beta_1\beta_2}{(\beta_1^2+\beta_2^2)^2} \cdot \frac{\left[\int E_1(x)E_2^*(x)dx\right]^2}{\int E_1(x)E_1^*(x)dx \cdot \int E_2(x)E_2^*(x)dx} \tag{2.46}$$

Assuming z-propagation, the coupling-mode equations for two modes with complex electric field amplitudes denoted by $\boldsymbol{A}$ and $\boldsymbol{B}$ are written by

$$\pm\frac{dA(z)}{dz} = -j\kappa_{ab}A(z)e^{j\Delta\beta z} - \alpha A(z) \tag{2.47}$$

$$\pm\frac{dB(z)}{dz} = j\kappa_{ba}B(z)e^{j\Delta\beta z} + \alpha B(z) \tag{2.48}$$

Where α is amplitude attenuation constant to account for waveguide loss. $\Delta\beta = \beta_1 - \beta_2$ is phase-mismatch, κ is coupling coefficient determined by overlap integral between electric field distribution and refractive index distribution. In most cases, $\kappa_{ba} = (\kappa_{ab})^*$ holds for Hermitian dielectric tensors where * indicates the conjugation operator [3].

$$\kappa_{ab} = \frac{\omega\varepsilon_0}{4}\int [n_a^2(x,y) - n_b]E_1(x,y)E_2(x,y)dxdy \tag{2.49}$$

$$\kappa_{ba} = \frac{\omega\varepsilon_0}{4}\int [n_b^2(x,y) - n_a]E_1(x,y)E_2(x,y)dxdy \tag{2.50}$$

When $\beta_1\beta_2 > 0$, the coupling is called co-directional, i.e., a forward-propagating mode excites another forward-propagation mode as in directional couplers. For $\beta_1\beta_2 < 0$, it is called contra-directional coupling where a forward-propagating mode will excite a backward-propagation mode as for grating couplers. The general solutions to the coupled-mode equations are

$$A(z) = C_1 e^{j(\alpha+\Delta\beta)z/2 - sz} + C_2 e^{j(\alpha+\Delta\beta)z/2 + sz} \tag{2.51}$$

$$B(z) = \frac{j}{\kappa}\frac{dA(z)}{dz}e^{\alpha - j\Delta\beta z} \tag{2.52}$$

$$s^2 = \kappa\kappa^* - (\Delta\beta/2)^2 \tag{2.53}$$

The constant C_1 and C_2 are determined by applying boundary conditions. Consider a grating coupler of the length L, the initial conditions are: $B(L) = 0$, $A(0) = A_0$, $\beta_1 > 0$ and $\beta_2 < 0$, the solutions become

$$A(z) = A_0 \frac{s\cdot\cosh(sL - sz) + j(\Delta\beta/2)\cdot\sinh(sL - sz)}{s\cdot\cosh(sL) + j(\Delta\beta/2)\cdot\sinh(sL)} e^{-\alpha + j\frac{\Delta\beta}{2}z} \tag{2.54}$$

$$B(z) = A_0 \frac{-j\kappa^*\sinh(sL - sz)}{s\cdot\cosh(sL) + j(\Delta\beta/2)\cdot\sinh(sL)} e^{\alpha - j\frac{\Delta\beta}{2}z} \tag{2.55}$$

Here, $\Delta\beta = \beta_1 - \beta_2 - mK$, where m is an integer indicating the grating order, $K = 2\pi/\Lambda$ is grating vector with Λ denoting the grating period. The mode power transfer or reflectance at $z = 0$ through the grating coupler is given by

$$\eta = \left|\frac{B(0)}{A(0)}\right|^2 = \frac{|\kappa|^2 \cdot \sinh^2(sL)}{s^2 \cdot \cosh^2(sL) + (\Delta\beta/2)^2 \cdot \sinh^2(sL)} e^{-2\alpha L} \tag{2.56}$$

Fig. 2.10 shows the power transfer efficiency (or grating reflectance) as a function of phase-mismatch. The transfer efficiency decreases smoothly as $\Delta\beta/2$ increases from 0 to K. Complete power transfer only occurs under phase-matching condition (or Bragg condition): $\Delta\beta = 0$ and the corresponding central wavelength is called Bragg wavelength λ_B. When $\Delta\beta/2$ is beyond K, the value of s becomes imaginary and the waves change from exponential to sinusoidal. It also shows that the grating reflectivity increase as κL increases under the phase-matching. The grating period that satisfies $\Delta\beta = 0$ is given by

$$\Lambda = \frac{\lambda_0}{2n_{eff}} \tag{2.57}$$

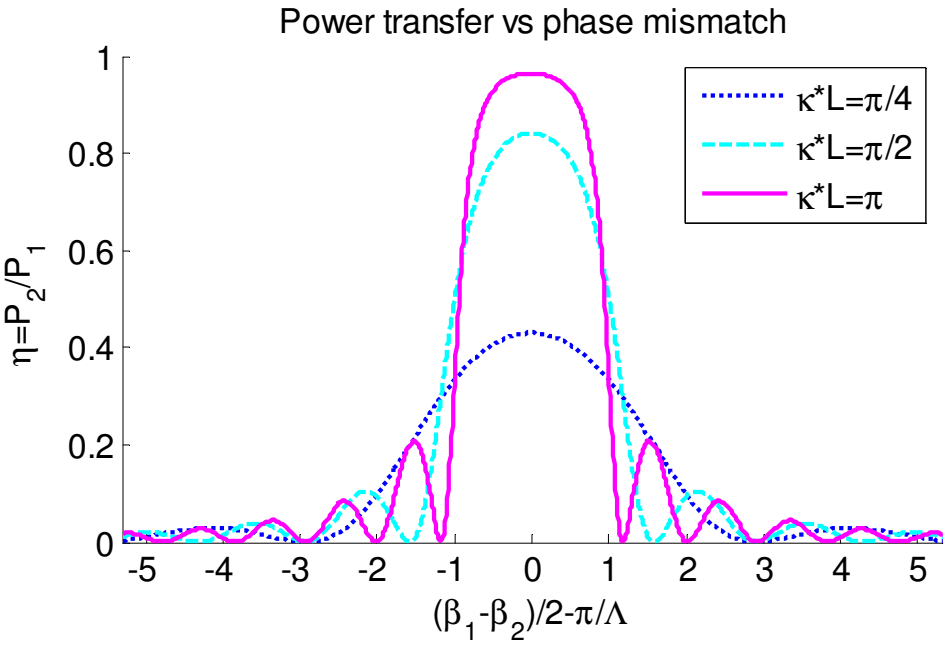

Fig. 2.10. Power transfer as a function of the phase-mismatch.

The reflectance bandwidth, defined as the spectral spacing between the first two minima near the reflectance peak, is expressed by

$$\Delta\lambda = \frac{\lambda_B^2}{2\pi n_{eff} L}\sqrt{(\kappa L)^2 + \pi^2}\ . \tag{2.58}$$

The calculation of coupling coefficient is of paramount importance for waveguide gratings. Consider the sidewall gratings integrated in As_2S_3 strip on Ti-diffused $LiNbO_3$ waveguide shown in Fig. 2.11. The gratings are written on both sidewalls of As_2S_3 strip with the thickness and width denoted by t and W_0. Grating depth is defined as the width difference: $\Delta W = (W_1 - W_2)/2$. Arbitrary grating profiles along x-axis and y-axis with periodic dielectric perturbation along z-axis can be expressed in the form of Taylor series as expressed by

$$\begin{aligned} &\Delta\varepsilon(y,z) = u(y)\Delta\varepsilon(z) \\ &u(y) = 1, (0 < y < t) \\ &\Delta\varepsilon(z) = \Delta\varepsilon_1 \cos(Kz) + \Delta\varepsilon_2 \cos(2Kz) + \cdots + \Delta\varepsilon_n \cos(nKz) \end{aligned} \tag{2.59}$$

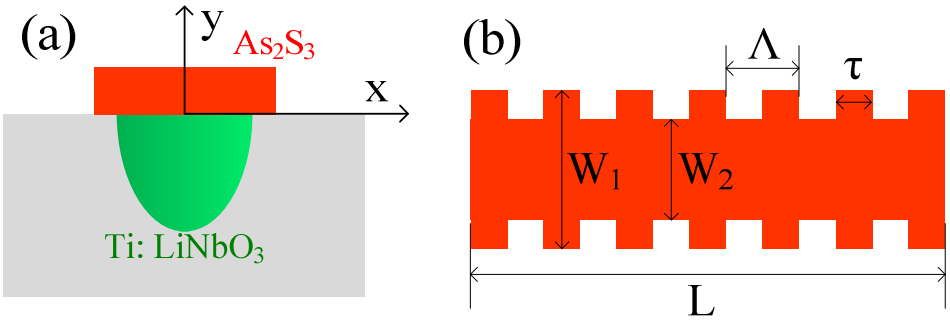

Fig. 2.11. (a) Cross-sectional and (b) top view of sidewall gratings.

Here, $\Delta\varepsilon_q$ is called harmonic coefficients, $\boldsymbol{K}$ is the grating vector. The influence of each harmonic can be analyzed individually and the total effect is obtained by summing all the harmonic terms. The harmonic coefficients for three common grating profiles are given below.

(1) Square Gratings:

$$\Delta\varepsilon_n = \frac{4(\varepsilon_{As2S3} - \varepsilon_0)}{n\pi}\sin(\frac{n\pi}{2}) = \frac{4(\varepsilon_{As2S3} - \varepsilon_0)}{n\pi}(-1)^{(n-1)/2} \quad (n = odd) \quad (2.60)$$

(2) Trapezoidal Gratings:

$$\Delta\varepsilon_n = \frac{16(\varepsilon_{As2S3} - \varepsilon_0)}{(n\pi)^2}\sin(\frac{nK_g\tau_r}{2})\sin(\frac{nK_g\tau}{2}) \quad (2.61)$$

(3) Sinusoidal Gratings:

$$\Delta\varepsilon_1 = (\varepsilon_{As2S3} - \varepsilon_0) \quad (2.62)$$

There are two main factors to consider in conducting the overlap integration to calculate the coupling coefficients of gratings: the number of total harmonics and the electric field resolution. Considering only the first order harmonic, both square and trapezoidal gratings have a stronger permutation due to their larger first order harmonic components. For a better approximation, higher order harmonics have to be included in the calculations, as illustrated by Fig. 2.12.

For square gratings with W_0 = 3.1 μm, ΔW = 0.4 μm and t = 0.35 μm, the effect of the number of harmonics on coupling coefficients κ is plotted in Fig. 2.13. It shows that the coupling coefficient κ oscillates with the total number of harmonics. At least 200 harmonics are needed to achieve a variation error smaller than 10^{-3} mm^{-1}.

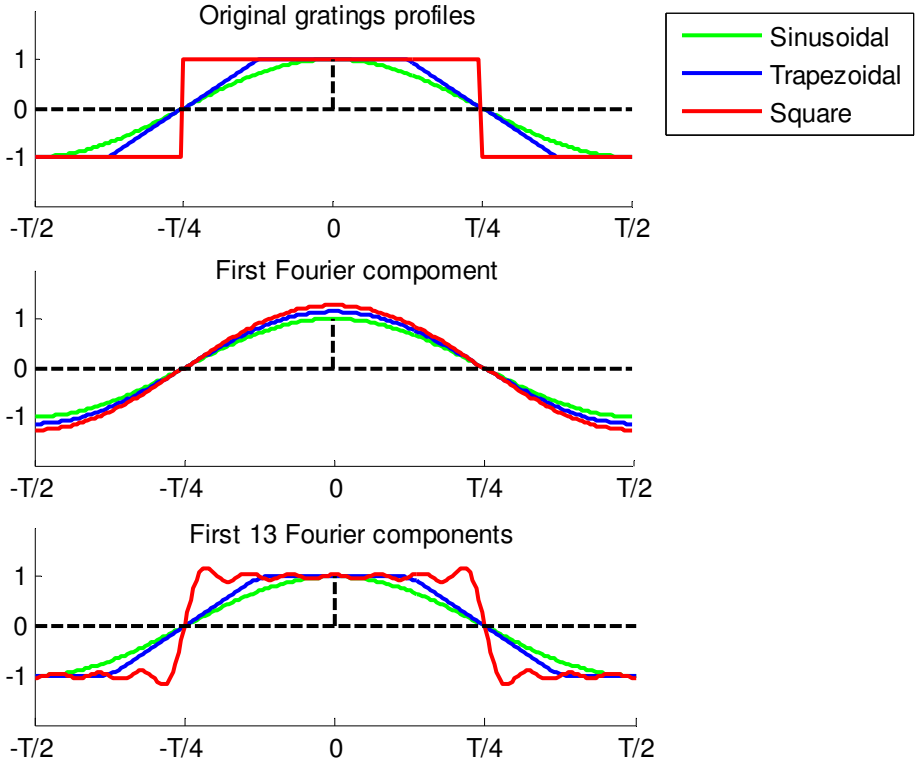

Fig. 2.12. Grating profiles approximated by harmonic components.

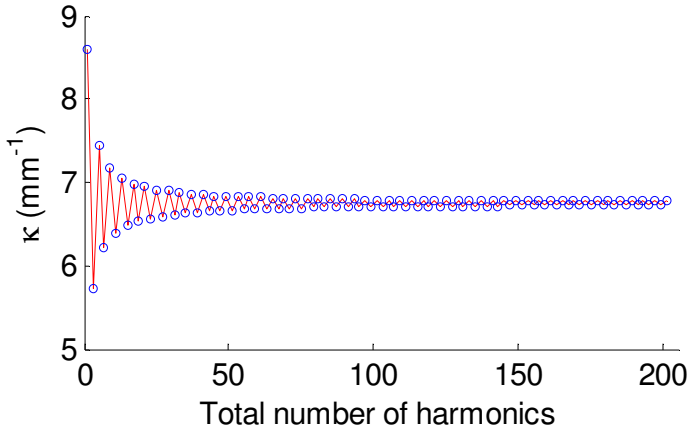

Fig. 2.13. Effect of the number of harmonics on coupling coefficient.

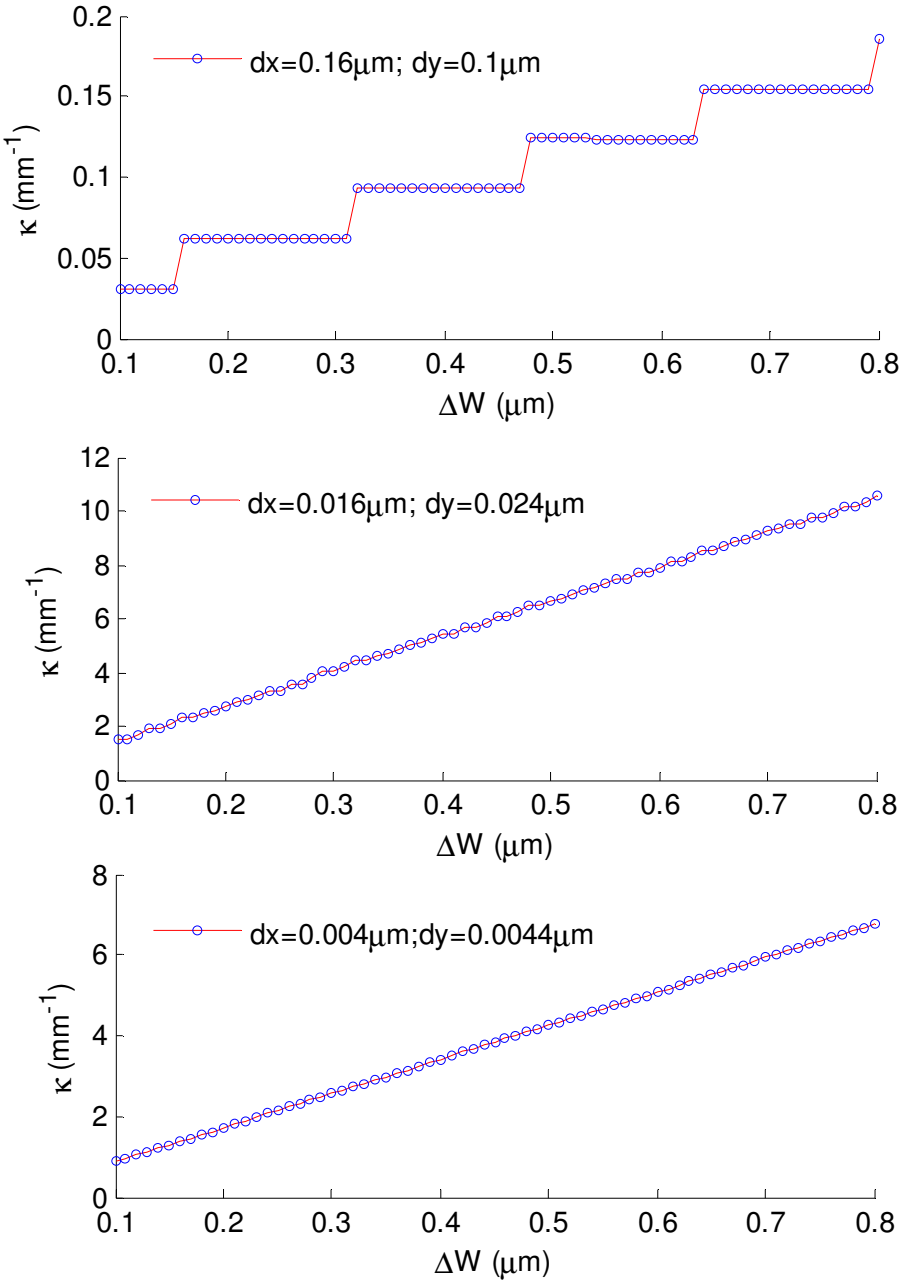

Fig. 2.14. Effect of the field resolution on coupling coefficient.

Another factor is the spatial resolution of transverse electric fields. Fig. 2.14 shows calculated values of κ as a function of grating depth ΔW at different spatial resolutions

(i.e., grid size: *dx* and *dy*) with the same grating parameters as in Fig. 2.13. Only a few sample points are used in the overlap integral at the grid resolution of *dx* = 0.16 μm and *dy* = 0.1 μm, leading to much smaller values of κ. Besides, the κ-ΔW relation exhibits stair-like behavior indicating the insufficient sampling. As the grid size gets smaller, the relation becomes smoother. When the resolution is beyond 0.5 nm, the κ-ΔW curve is almost linear. At this point, the coupling coefficient can be accurately calculated.

2.4 Transfer Matrix Method

Transfer matrix method is widely used in optics to analyze the propagation of optical waves through stratified or layered medium. It is based on simple continuity conditions for electric fields across boundaries from one segment to another. If the fields are known at the beginning of one segment, the fields at the end of the segment can be derived from a simple matrix operation *M*. Then, a stack of segments is treated as system matrix that is the product of all individual matrices. Finally, reflection and transmission coefficients are derived from the system matrix [72]. For example, the propagation of a given wave through an isotropic, lossless and homogeneous layer with the thickness of *L*, then the transfer matrix is

$$M = \begin{bmatrix} \cos(\beta L) & \frac{1}{\beta}\sin(\beta L) \\ -\beta \sin(\beta L) & \cos(\beta L) \end{bmatrix} \tag{2.59}$$

Assuming the propagation is along *z*-axis, if the fields at $z = 0$ are known, the field at $z = L$ is represented by

$$\begin{bmatrix} E(z=L) \\ H(z=L) \end{bmatrix} = M \cdot \begin{bmatrix} E(0) \\ H(0) \end{bmatrix} \tag{2.60}$$

For a system with N layers, each layer i has a transfer matrix M_i, where i increases towards higher z values, the system transfer matrix is

$$M_s = M_N \cdots\cdots M_i \cdots\cdots M_2 \cdot M_1 \tag{2.61}$$

The transfer matrix method can be directly applied to analyze spectral response of phase-shift Bragg gratings as well. Provided the coupling coefficient, grating length, and wavelength are given, the individual and system matrices are

$$M_i = \begin{bmatrix} \cosh(sL_i) - j\frac{\Delta\beta}{2s}\sinh(sL_i) & -j\frac{\kappa}{s}\sinh(sL_i) \\ j\frac{\kappa}{s}\sinh(sL_i) & \cosh(sL_i) + j\frac{\Delta\beta}{2s}\sinh(sL_i) \end{bmatrix} \tag{2.62}$$

$$M_s = \begin{bmatrix} M_{11} & M_{12} \\ M_{21} & M_{22} \end{bmatrix} = \prod_i M_i \tag{2.63}$$

The reflection and transmission coefficients are derived as

$$R = \left|\frac{M_{21}}{M_{11}}\right|^2 ; \quad T = 1 - \left|\frac{M_{21}}{M_{11}}\right|^2 . \tag{2.64}$$

2.5 Nonlinear Optics

The polarization density is a product of individual dipole moment induced by the applied electric field and the number of dipole moments. A linear dielectric medium is characterized by a linear relation between polarization density and electric field as in Eq. (2.9). However, when the electric field is comparable to inter-atomic electric fields,

which are typically 10^5-10^8 V/m, this relation becomes nonlinear [2]. The nonlinearity may be of microscopic or macroscopic origin.

Since externally applied optical electric fields are typically small compared with characteristic inter-atomic or crystalline fields, even when focused laser light is used, the nonlinearity is usually weak. The relation between polarization density $\boldsymbol{P}$ and electric field $\boldsymbol{E}$ is approximately linear for small $\boldsymbol{E}$, deviating only slightly from linearity as $\boldsymbol{E}$ increases. Therefore, the function that relates $\boldsymbol{P}$ to $\boldsymbol{E}$ can be expanded in Taylor series about $\boldsymbol{E} = 0$ as represented by

$$P = \varepsilon_0 \chi E + P^{NL} = \varepsilon_0 \chi E + \varepsilon_0 \chi^{(2)} E^2 + \varepsilon_0 \chi^{(3)} E^3 + \cdots \tag{2.65}$$

Here, χ is linear susceptibility that is related to the dielectric constant or refractive index of the material by $n^2 = \varepsilon/\varepsilon_0 = 1 + \chi$, the $\chi^{(2)}$ term represents a quadratic or second-order susceptibility, the $\chi^{(3)}$ term is called the third-order nonlinearity, and so on. In centrosymmetric media, which have inversion symmetry so that the properties are not altered by the transformation $\boldsymbol{r} \rightarrow \boldsymbol{-r}$, the above relation must have odd symmetry, so the second-order coefficient must then vanish, and the lowest-order nonlinearity is of third order.

The propagation of light in a nonlinear medium is governed by the wave equation in Eq. (2.10), rewritten as

$$\left(\frac{\partial^2}{\partial x^2} + \frac{\partial^2}{\partial y^2} + \frac{\partial^2}{\partial z^2} \right) E(r) - \omega^2 \mu \varepsilon E(r) = \mu_0 \frac{\partial^2 P^{NL}}{\partial t^2} \tag{2.66}$$

This is a nonlinear partial differential equation that underlies the theory of nonlinear optics. The term on right-hand-side can be regarded as a source that radiates in a linear

medium of refractive index n. Two approximate methods are used to solve this nonlinear wave equation. The first is an iterative approach known as the Born approximation which is based on scattering theory. The second method is a coupled-mode theory in which the nonlinear wave equation is used to derive linear coupled partial differential equations that govern the interacting waves [2]. Coupled-mode theory is the basis for more advanced analysis of wave interactions in nonlinear media.

In second-order nonlinear media, optical processes such as second-harmonic generation (SHG), optical rectification, linear electro-optic effect (Pockels effect), and three-wave mixing occurs under proper configurations. The second-order nonlinear medium can be used to mix two optical waves of difference frequencies and generate a third wave at the difference (called frequency down-conversion, or difference-frequency generation) or at the sum frequency (also known as frequency up-conversion, or sum-frequency generation). In a third-order nonlinear medium (or Kerr medium), it responds to optical fields by generating third harmonics and sums and differences of triplets of frequencies. The third-harmonic generation (THG), optical Kerr effect, self-phase modulation (SPM), cross-phase modulation (XPM), self-focusing, and four-wave mixing (FWM) are common nonlinear processes in such Kerr media.

Taking the second-order nonlinearity as an example, the coupled-wave equations for three interacting waves are described by three differential equations.

$$\begin{cases} (\nabla^2 + \beta_1^2)E_1 = -\mu_0 \omega_1^2 \chi^{(2)} E_3 E_2^* \\ (\nabla^2 + \beta_2^2)E_1 = -\mu_0 \omega_2^2 \chi^{(2)} E_3 E_1^* \\ (\nabla^2 + \beta_3^2)E_1 = -\mu_0 \omega_3^2 \chi^{(2)} E_1 E_2 \end{cases} \tag{2.67}$$

Assume the three waves are plane waves traveling in z-axis with complex field amplitudes expressed as

$$E_q = A_q \exp(-j\beta_q z) \quad (q = 1,2,3) \tag{2.68}$$

It is convenient to normalize the complex envelopes, $\boldsymbol{A_q}$, by defining

$$a_q = \frac{A_q}{\sqrt{2\eta\hbar\omega_q}} \tag{2.69}$$

Where $\eta = \eta_0/n$ is the impedance of the medium, $\eta_0 = (\mu_0/\varepsilon_0)^{1/2}$ is the impedance of free space (~ 377 ohms), $\hbar = 6.58\times10^{-16}$ eV·s is the reduced Planck constant. Thus, the intensities and photon flux densities (photons/s-m^2) associated with these waves are

$$I_q = \frac{\left|E_q\right|^2}{2\eta} = \hbar\omega_q \left|a_q\right|^2 \tag{2.70}$$

$$\phi_q = \frac{I_q}{\hbar\omega_q} = \left|a_q\right|^2 \tag{2.71}$$

This normalization is convenient because wave mixing process must be governed by photon-number conservation (or energy conservation). With slowly varying envelope approximation where d^2a_q/dz^2 is negligible, the above coupled-wave equations reduced to first-order differential equations that are akin to the paraxial Helmholtz equations with phase-mismatch $\Delta\beta$ considered [2].

$$\begin{cases} \dfrac{da_1}{dz} = -jga_3a_2^* \exp(-j\Delta\beta z) \\ \dfrac{da_2}{dz} = -jga_3a_1^* \exp(-j\Delta\beta z) \\ \dfrac{da_3}{dz} = -jga_1a_2 \exp(j\Delta\beta z) \end{cases} \tag{2.72}$$

where $g = \sqrt{2\hbar\omega_1\omega_2\omega_3\eta^3 d^2}$, $d = \frac{\varepsilon_0}{2}\chi^{(2)}$, $\Delta\beta = \beta_3 - \beta_2 - \beta_1$.

Consider a frequency up-converter that convert a wave of frequency ω_1 into a wave of higher frequency ω_3 by use of an auxiliary wave at frequency ω_2, called the pump. The conversion process is governed by Eq. (2.72). Assume perfect phase-matching $\Delta\beta$ = 0 and undepleted pump (i.e., the pump is sufficiently strong so that its amplitude does not change appreciably within the interaction distance of interest). The coupled-wave equations reduce to

$$\begin{cases} \dfrac{da_1}{dz} = -jga_3a_2 \\ \dfrac{da_3}{dz} = -jga_1a_2 \end{cases} \tag{2.73}$$

The harmonic solutions are

$$\begin{cases} a_1(z) = a_1(0)\cos\left[ga_2 z\right] \\ a_3(z) = -ja_1(0)\sin\left[ga_2 z\right] \end{cases} \tag{2.74}$$

The dependencies of photon flux densities are sketched in Fig. 2.15. It is clear that photons are exchanged periodically between two waves. In the region between $z = 0$ and $z = \pi/(2g\cdot a_2)$, the input ω_1 photons combine with the pump ω_2 photons and generate the up-converted ω_3 photons. As a result, signal wave is attenuated, whereas up-converted wave is amplified. For the region between $z = \pi/(2g\cdot a_2)$ and $z = \pi/(g\cdot a_2)$, the ω_3 photons are more abundant and they disintegrate into ω_1 and ω_2 photons, so that up-converted wave is attenuated and signal wave amplified. This process is repeated periodically as the waves travel through the medium.

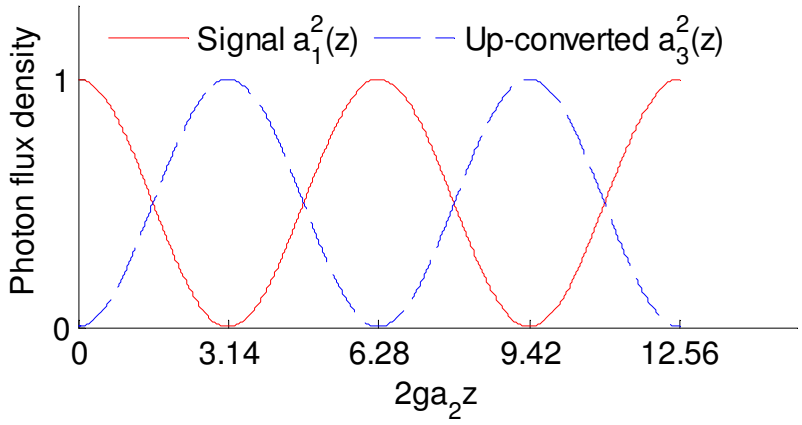

Fig. 2.15. Evolution of photon flux densities of the signal and up-converted wave.

The efficiency of up-conversion for a device of length L is

$$\eta_{conversion} = \frac{I_3(L)}{I_1(0)} = \frac{\omega_3}{\omega_1}\sin^2(ga_2L) \tag{2.75}$$

For $(ga_{2L}) << 1$, it is reduced to

$$\eta_{conversion} \approx \frac{\omega_3}{\omega_1}(ga_2L)^2 = 2\omega_3^2L^2d^2\eta^3I_2 \tag{2.76}$$

Assume the cross-sectional area is $\boldsymbol{A}$ and $P_2 = I_2A$ is the pump power, then the conversion efficiency is expressed as

$$\eta_{conversion} = \frac{2\omega_3^2\eta_0^3d^2L^2}{n^3A}P_2. \tag{2.77}$$

2.6 Electro-optic Effect

As aforementioned, electro-optic (EO) effect is the phenomena that the refractive index of a second-order nonlinear optical crystal changes when an electric field is applied. Perturbation in dielectric polarization along a waveguide can also be produced

from the application of electrical field or strain field. Such perturbation introduces index change, which can be used for a great variety of devices such as phase modulators, intensity modulators and polarization converters. For optical crystals without inversion symmetry, the index changes linearly with the externally-applied electric field. This is also called Pockels effect. In central-symmetrical crystals, Pockels effect is absent and the induced index change is proportional to the square of electric field. This is called Kerr effect. In general, linear EO effect provides the largest index change [73].

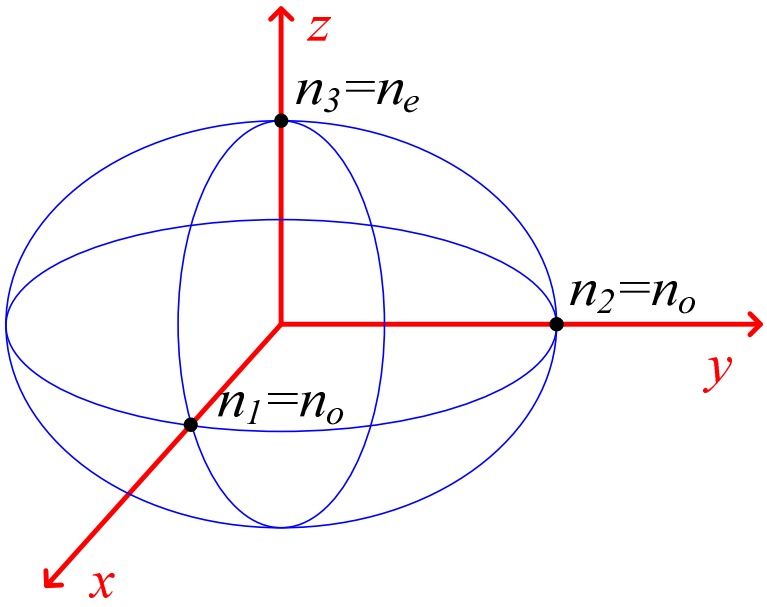

Fig. 2.16. The index ellipsoid for $LiNbO_3$ crystal.

Optical anisotropy is also observed in ferroelectric crystals such as $LiNbO_3$ where the refractive index depends on both crystal orientation and light propagation direction. An index ellipsoid, as sketched in Fig. 2.16, is often used to determine the corresponding

refractive index. If the principal axes of the index ellipsoid coincide with the coordinate system, the ellipsoid is diagonalized and can be written as

$$\frac{X^2}{\varepsilon_{11}}+\frac{Y^2}{\varepsilon_{22}}+\frac{Z^2}{\varepsilon_{33}}=1 \tag{2.78}$$

In terms of refractive index, since $\varepsilon_{jj}=(n_j)^2$, it yields

$$\frac{x^2}{n_1^2}+\frac{y^2}{n_2^2}+\frac{z^2}{n_3^2}=1 \tag{2.79}$$

In terms of inverse permittivity for simplicity, define $B=1/\varepsilon_{jj}$, then

$$B_{11}X^2+B_{22}Y^2+B_{33}Z^2=1 \tag{2.80}$$

When an electric field is applied, the index ellipsoid will be distorted through rotation or stretched along some directions. Then the index ellipsoid is no longer diagonalized. Thus, a general form of ellipsoid equation is introduced

$$B'_{11}X^2+B'_{22}Y^2+B'_{33}Z^2+2B'_{23}YZ+2B'_{13}XZ+2B'_{12}XY=1 \tag{2.81}$$

Rearranging the coefficients with reduced notations for convenience,

$$B'_1X^2+B'_2Y^2+B'_3Z^2+2B'_4YZ+2B'_5XZ+2B'_6XY=1 \tag{2.82}$$

And the index changed induced by externally-applied electric field can be described by a 6-by-3 electro-optic tensor

$$\Delta\left(\frac{1}{n_i^2}\right)\equiv\Delta B_i=B'_i-B_i=\sum\nolimits_{j=1}^{3}r_{ij}E_j \quad (i=1,2,3,4,5,6) \tag{2.83}$$

The magnitudes of refractive indices along principle axes can be changed by applying electric field. Note $B_4 = B_5 = B_6 = 0$ if the electric field is absent, a rotation is

introduced to the index ellipsoid from the applied electric field which produces off diagonal elements.

The elements of electro-optic tensor depend on crystal and its symmetry, some elements may be equal to zero and some may be equal to each other. For $LiNbO_3$, it has 3m symmetry, the electro-optic tensor (at the wavelength 632.8 nm) is

$$r_{ij} = \begin{pmatrix} 0 & -r_{22} & r_{13} \\ 0 & r_{22} & r_{13} \\ 0 & 0 & r_{33} \\ 0 & r_{51} & 0 \\ r_{51} & 0 & 0 \\ -r_{22} & 0 & 0 \end{pmatrix} = \begin{pmatrix} 0 & -3.4 & 8.6 \\ 0 & 3.4 & 8.6 \\ 0 & 0 & 30.8 \\ 0 & 28 & 0 \\ 28 & 0 & 0 \\ -3.4 & 0 & 0 \end{pmatrix} \times 10^{-12} \ (m/V) \tag{2.84}$$

Recall that

$$\Delta\left(\frac{1}{n_i^2}\right) = \frac{0 - 2n_i \Delta n_i}{n_i^4} = \sum_{j=1}^{3} r_{ij} E_j \tag{2.85}$$

Thus, the refractive index change is given by

$$\Delta n_i = -\frac{1}{2} n_i^3 \sum_{j=1}^{3} r_{ij} E_j \quad (i = 1,2,3,4,5,6)\,. \tag{2.86}$$

CHAPTER III

FABRICATION PROCESS

3.1 Ti-diffused $LiNbO_3$ Waveguide

Among the methods of preparing channel waveguides in lithium niobate ($LiNbO_3$), thin film titanium-diffusion is a favored one due to its high-quality, low propagation loss and ease of fabrication. Such channel waveguide possesses a comparable mode area size to that of standard single-mode fiber (SMF). This enables easy integration of such waveguides with other active and passive functional elements on a same microchip. The fabrication of such channel waveguide is well established with high quality and excellent reproducibility. We will first discuss the fabrication process for Ti-diffused $LiNbO_3$ (Ti: $LiNbO_3$) optical waveguides.

The fabrication process starts with cutting 1 mm-thick, 3 inch-diameter $LiNbO_3$ wafers, supplied by Crystal Technology Inc (Palo Alto, CA), into rectangular samples with a dimension of 24cm-by-20cm. After cleaning successively with soap water, acetone, isopropyl alcohol (IPA), de-ionized (DI) water and methanol, the sample is then deposited a preselected thickness of titanium thin film. For near-infrared 1.55 μm wavelength, the desired thickness is 95 nm, and it is 135 nm for mid-infrared 2.05 μm wavelength. The titanium strips are patterns by contact photolithography and subsequently reactive ion etching (RIE). The titanium diffusion process is conducted in a thermal furnace made of quarts at a temperature of 1025 ºC for an optimized time period. Fig. 3.2 briefly sketches fabrication process flow for Ti-diffused $LiNbO_3$ waveguides.

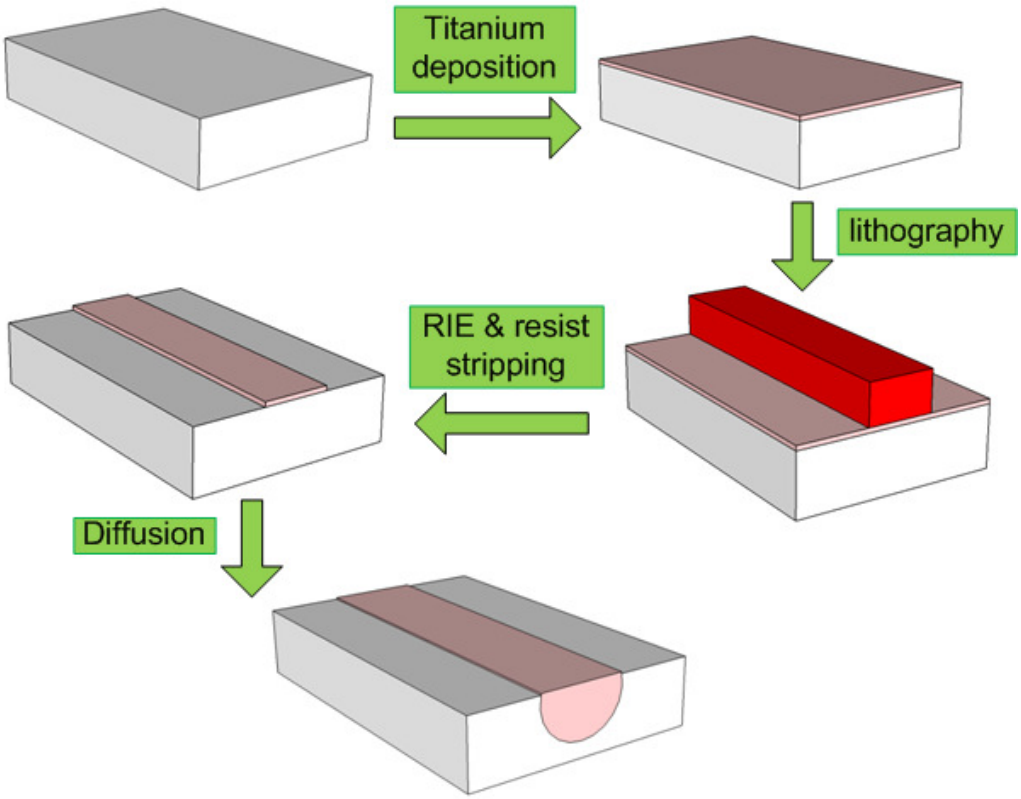

Fig. 3.1. Fabrication process for Ti-diffused $LiNbO_3$ waveguide.

Titanium thin film is deposited by magnetron sputtering system, supplied by AJA International Inc (Scituate, MA), as shown in Fig. 3.2. This AJA sputtering deposition system has both DC (direct current) and RF (radio frequency) configurations. Two parallel plates are used as the cathode mounted with a target material and the anode loaded with the sample. Once the chamber is pumped down to 10^{-6} Torr, inert argon gas is flowed into the chamber and accumulated until the chamber pressure reaches 20 mTorr. Then a high sputter voltage between 2-5 kV is applied to create a strong electric field between the two electrode plates where electrons accelerate and ionize argon atoms by $e^- + Ar \rightarrow 2e^- + Ar^+$, leading to ionization cascade process. Every creation of one

ionized argon atom also involves the generation of another electron which causes another ionization of argon atom, and this process continues. As a result, a self-sustained plasma environment is realized. Relatively larger distance between cathode and anode is needed for electrons to gain sufficient energy but it requires higher plasma breakdown voltage. In practice, the distance is chosen about 10 cm. Due to the strong electric field between the two parallel electrodes, electrons escape from the plasma body more rapidly than ions due to its small mass, resulting in positively-charged plasma. The escaped ions are accelerated towards the cathode and break the bonds of target atoms on the surface. These sputtered atoms from target materials are neutral and so are unaffected by the charged plasma and get deposited to the sample surface.

Magnetrons are often employed by sputtering system to confine charged plasma particles close to the target surface. In a magnetic field, electrons will follow helical paths and thus experience more ionizing collisions with gaseous neutrals near the target surface. Extra argon ions created during the collision lead to a higher deposition rate at a lower pressure and lower power. As a physical vapor deposition (PVD) method, magnetron sputtering provides a denser film with better adhesion on the sample surface compared with electron beam evaporation.

A typical configuration of electron beam evaporator is shown in Fig. 3.3 [74]. The deposition chamber must be evacuated to a pressure of 10^{-5} Torr for the electrons from the e-gun to the evaporation materials that are in the form of ingot pebbles or rods. The electrons are accelerated by magnetic fields to heat up the evaporation materials so that the evaporated atoms transport from the target to deposit a thin film onto the substrate

surface. The disadvantages of electron beam evaporation method include line-of-sight deposition process, non-uniform evaporation rate due to filament degradation and the scattering effects of vaporized target atoms. Therefore, we used DC sputtering method in order to obtain high-quality titanium film desired for low-loss optical waveguides.

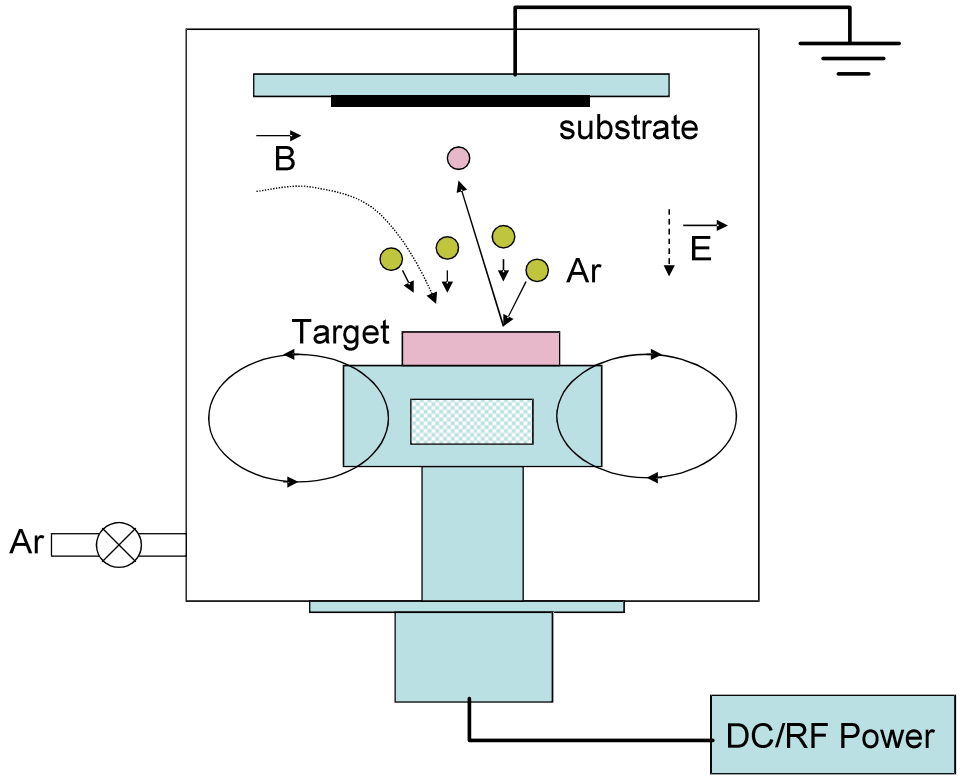

Fig. 3.2. Configuration of DC/RF magnetron sputtering deposition system.

Contact photolithography (*i*-line mask aligner, MA6) is used here to pattern the Ti strip waveguides. First a positive-tone photoresist AZ 5214 is spin coated the sample at a rotation speed of 4000 rpm for 40 seconds with a 5 second acceleration/deceleration time. After soft-bake on a hotplate at 125 ºC for 1 min, the sample is loaded onto the

mask aligner for exposure at a dose of 85 mJ/cm^2. Then, the sample is immersed in MF 312 developer solution for about 45 seconds to reveal the Ti strip waveguide patterns. After confirming the patterns under high-magnification optical microscope (500X), the sample is baked in an oven heated at 135 ºC for 15 minutes to harden the photoresist for the subsequent dry etching process.

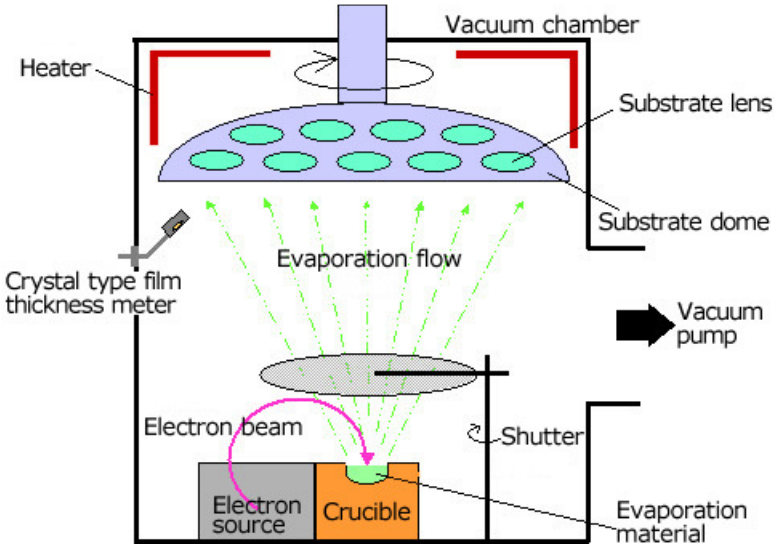

Fig. 3.3. Configuration of electron beam evaporation system [74].

An inductively-coupled plasma (ICP) reactive ion etching (RIE) system, supplied by Oxford Instruments, is used for etching process. We used an optimized gas mixture of carbon tri-fluoride (CHF_3) and argon (Ar) to produce volatile titanium fluoride (TiF_x) reaction byproducts on the etching of Ti samples. The etching consists of inert argon ion bombardment (physical sputtering) and reactive CHF_3 chemical etching. The reaction byproducts AsF_x and SF_x are highly volatile and can be removed easily by gas flow. The

fluorocarbon polymer can form a passivation layer on the etched sidewalls to enhance etching directionality. The plasma induced by the inductive coils surrounding the etching chamber provides a higher etch rate but less damage at a lower voltage. To alternatively avoid the surface damage, it is also feasible to stop etching right before the substrate and continue etching with diluted hydrofluoric acid (5%). For nonconductive substrate such as $LiNbO_3$, the etch profile undergoes undesired undercut problem because of charging effect. To prevent this, the etching time and etching rates have to be precisely controlled. To improve sidewall roughness, higher ICP power and lower pressure are of paramount importance. Higher ICP power provides higher plasma density and lower pressure reduce the ion-molecule scattering, leading to better etching directionality. In addition, the photoresist roughness can be transferred into waveguide, which can be improved by simply increasing the hard-bake time [75]. The height of Ti strip waveguides after stripping remaining photoresist is measured by Dektak 150 3D surface profiler to check the desired deposition thickness and adjust diffusion time.

The substrates are then put into a diffusion furnace for a preselected time period with an ambient breathing air environment at a temperature of 1025 ºC. The sample holder is made of alumina and the furnace tube is made of quartz. The wet environment is used to prevent lithium out-diffusion effects that may form a lateral surface guiding layer [76, 77]. During the diffusion process, Ti atoms from the patterned Ti strips will diffuse into $LiNbO_3$ substrate. The diffusion profile is characterized by lateral and vertical diffusion lengths, which are calculated from diffusion temperature and initial Ti geometries [78]. The refractive index has Gaussian distribution laterally and Hermit-Gaussian distribution

vertically. Smooth surface is essential for achieving low-loss hybrid optical waveguide structures. If the Ti substrate is under-diffused, great optical loss can be introduced, it is critical to optimize the diffusion time, temperature and breathing air environment. For near-infrared 1.55 μm wavelength, the optimal diffusion time is 11.5 hours plus 1 hours and 15 minutes temperature ramping time. At 2.05 μm, the diffusion time is optimized at 16.5 hours. It takes about 6 hours for the furnace cools down slowly to room temperature without interference after diffusion.

The edges of the sample are too rough for optical testing and measurement. The end facets of Ti-diffused $LiNbO_3$ sample have to be polished to optical quality. We used a polishing machine to manually polish the sample with three different abrasive pads. The abrasive pads have diamond particles of various grain sizes bonded on it. Polishing is started with a relative course pad with a grain size of 10 μm, successively followed by two pads with smaller grain sizes at 3 μm and 0.5 μm. After polishing, end facets of optical quality are obtained and the measured fiber-coupling loss is < 0.5 dB per facet.

3.2 As_2S_3 Sidewall Bragg Gratings

Arsenic tri-sulfide (As_2S_3) is a member of chalcogenide glass family. Chalcogenide glasses are popular materials for both near-infrared and mid-infrared optical waveguides and devices due to their broad transmission properties. Different fabrication methods are developed to make chalcogenide optical waveguides such as conventional top-down method, liftoff, nano-imprint, solution-process, photorefractive effects [79-82]. The top-down approach provides best control on waveguide dimensions which involves film

deposition, lithography and etching processes. Lift-off process is easy and simple to fabricate waveguide by removing photoresist directly after film deposition and no etching is needed. Solution-processed and nano-imprint waveguides are defined by a soft stamp and revealed by peeling off the stamp. The refractive index of chalcogenide glass will be changed under proper light illumination; such photorefractive effect can be to create optical waveguide. Here, metal lift-off process is used to fabricate sidewall gratings on As_2S_3 strip waveguides. Fig. 3.4 briefly illustrates the fabrication process flow for As_2S_3 sidewall gratings.

The fabrication of As_2S_3 sidewall gratings starts with the above prepared Ti-diffused $LiNbO_3$ sample. Firstly, a desired As_2S_3 thickness is deposited by RF (radio-frequency) magnetron sputtering system as illustrated in Fig. 3.1. Unlike titanium target, arsenic tri-sulfide is an insulating material, so RF sputtering source as well as impedance matching networks has to be used instead of DC source to avoid charge build-up on insulator targets. The sign of anode-cathode bias is varied at a high frequency of 13.56 MHz. Electrons can respond to such fast switching and neutralize the charge build-up at insulator targets while ions cannot follow the fast switching due to their larger mass-charge-ratios.

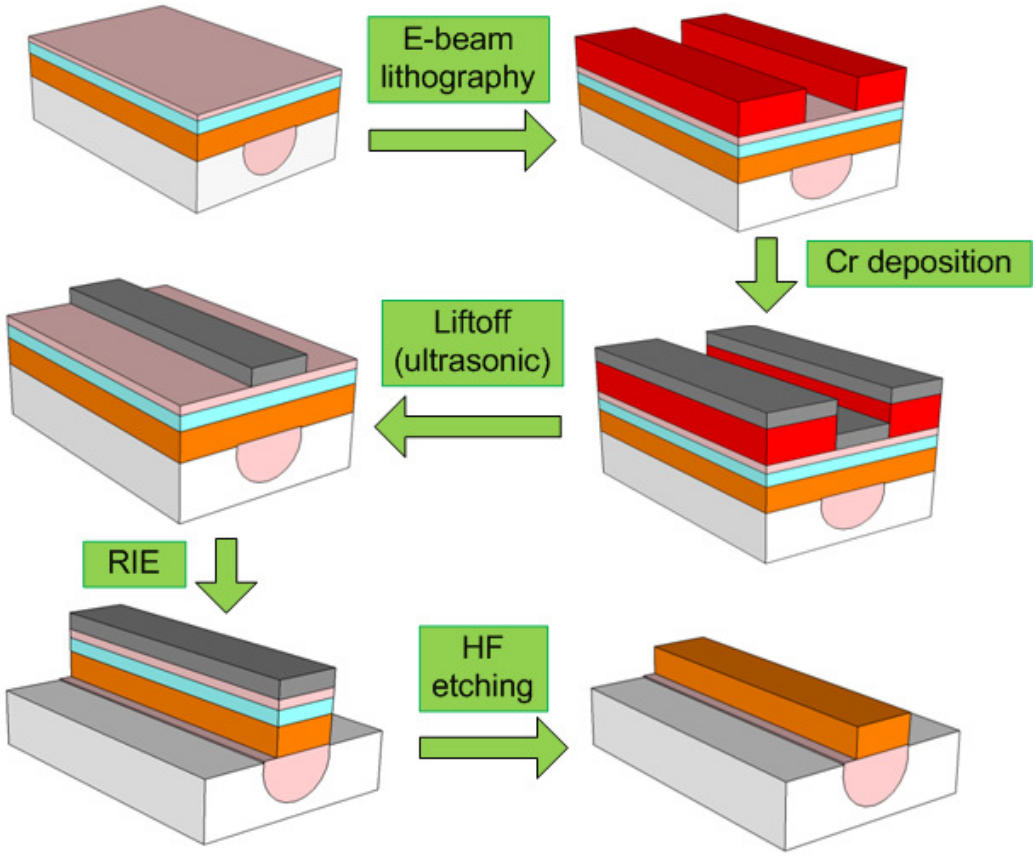

Fig. 3.4. Fabrication process for As_2S_3 sidewall gratings.

In general, there are mainly four ways to depositing As_2S_3 film: spin coating, thermal evaporation, pulse laser deposition and RF sputtering. A solution of As_2S_3 is firstly prepared before spin coating. It is simple and cost-effective, but the oxidation of As_2S_3 solution is unavoidable. Due to the low melting temperature (300 ℃) of As_2S_3 glass compared to oxide glasses, additional annealing is needed after thermal evaporation or pulse laser deposition of As_2S_3 to stabilize refractive index distribution; otherwise, the refractive index can be altered by illuminating a light with above band-gap energy on it. This is so-called photorefractive or photo-darkening effect and can be utilized to form

optical waveguide as well [80]. RF magnetron sputtering method is used here and a recipe is optimized to deposit uniform, dense, amorphous As_2S_3 film. On As_2S_3 thin film, a protection layer made of 130 nm SiO_2 and 25 nm Ti are also deposited as a protection layer. It prevents As_2S_3 from being exposed to air and protects it from being dissolved by $(CH_3)_4NOH$-based developers such as MF 312.

Because the sidewall gratings on As_2S_3 waveguide is on top of Ti-diffused channel waveguide, align marks are needed to precisely align the As_2S_3 layer with respect to the Ti-diffused sample. We prepared cross marks made of high atom-number metal tungsten (W) for the align purpose during electron-beam lithography (EBL). The tungsten crosses are 3 μm wide and 1000 μm long and located on the top and bottom edges of the sample. Image reversal lithography and metal lift-off process are used to prepare such tungsten align marks. The sample is firstly spin coated with photoresist AZ 5214 at 4000 rpm for 40 seconds with 5 seconds acceleration/deceleration rate. After soft-baking on a hotplate at 85 ºC for 1 minute, the sample is exposed by MA6 at a dose 65 mJ/cm^2. The sample is then reverse-baked on another hotplate at 105 ºC for 1 minute, followed by a flood exposure without loading photo mask at a dose 265 mJ/cm^2. The sample is developed with the MF 312 developer solution for about 40 seconds to reveal the void patterns.

After that, the sample is ready for deposition of 200 nm tungsten by DC magnetron sputtering system. Since the same photo mask is used during image reversal lithography, the middle region of sample is covered by Teflon tape to prevent tungsten deposition on waveguide patterns, as shown in Fig. 3.5. The tungsten looks dark and shiny at about 200 nm thickness.

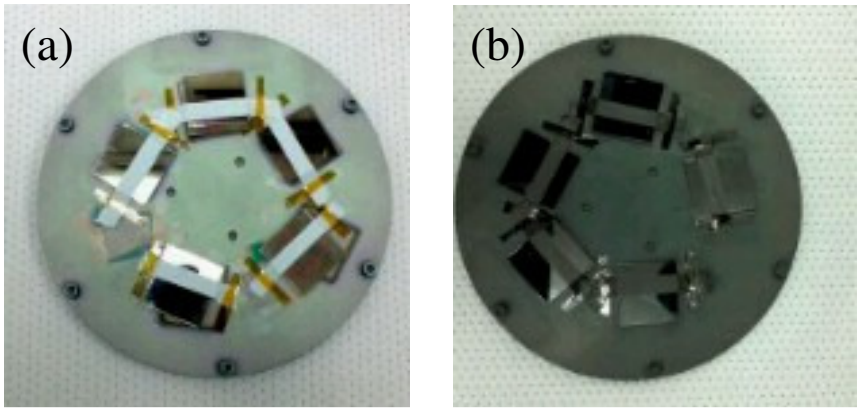

Fig. 3.5. (a) Before and (b) after tungsten deposition on the samples.

Subsequently, the sample is placed face-down in a beaker of acetone for 3 minutes. The beaker is then put into the ultrasonic cleaner for another 3 minutes to reveal tungsten cross marks. The tungsten cross marks are checked under a high-magnification microscope to assure the cross marks are well developed. The sample is placed face-down to avoid re-deposition of tungsten. Fig. 3.6 displays one of the prepared tungsten align marks with two 1 mm-long 3 μm-wide strips crossing over each other.

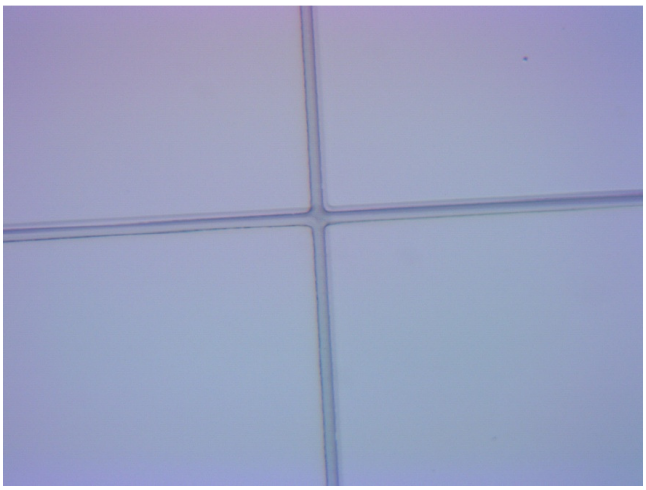

Fig. 3.6. Tungsten cross align marks after liftoff process.

Electron beam lithography (EBL), JBX-5500FS supplied by JOEL, is used to write As_2S_3 sidewall gratings because it has sub-10 nm resolution and our gratings has a grating period of 360 nm. A typical electron beam lithography system includes electron sources, electrostatic lenses, stage stitching and alignment and a control computer. It scans a focused beam of electrons to directly write custom patterns on a surface covered with an electron sensitive film, called electron beam resist. The high-energy beam of electrons changes the solubility of the resist enabling selective removal of the exposed area (positive-tone resist) or non-exposed area (negative-tone resist) of the resist by immersing it in a developer solution. Compared to photolithography, it has much smaller feature size but lower throughput, limiting its usage to photo mask fabrication, low-volume manufacturing, research and development.

3% PMMA (polymethyl methacrylate) resist is used for electron beam lithography. PMMA is an ultra-high resolution, high-current, positive-tone resist, which sticks well to almost any metal surface and provides excellent reproducible results [83]. The resist is spin coated at a rotation speed of 2500 rpm for 60 seconds with a ramp at 1250 rpm. After soft-baking on a hotplate at 180 ℃ for 2 minutes, the sample is loaded into the chamber for exposure. To find optimum dose for smooth sidewall gratings, a dose test is conducted with 50 keV electrons and 1 nA electron current. The dosage D is determined by the electron current I, exposure area A and writing time t, as expressed in Eq. (3.1).

$$D \cdot A = I \cdot t \tag{3.1}$$

After exposure, the sample is developed in IPA solution (IPA: Water = 2:1) at room temperature for 30 seconds. It is found that a dose at 350 $\mu C/cm^2$ gives uniform sidewall

gratings and the grating duty cycle is close to 0.5. Fig. 3.7 presents scanning electron microscope images for gratings and grating-taper transitions exposed at different doses.

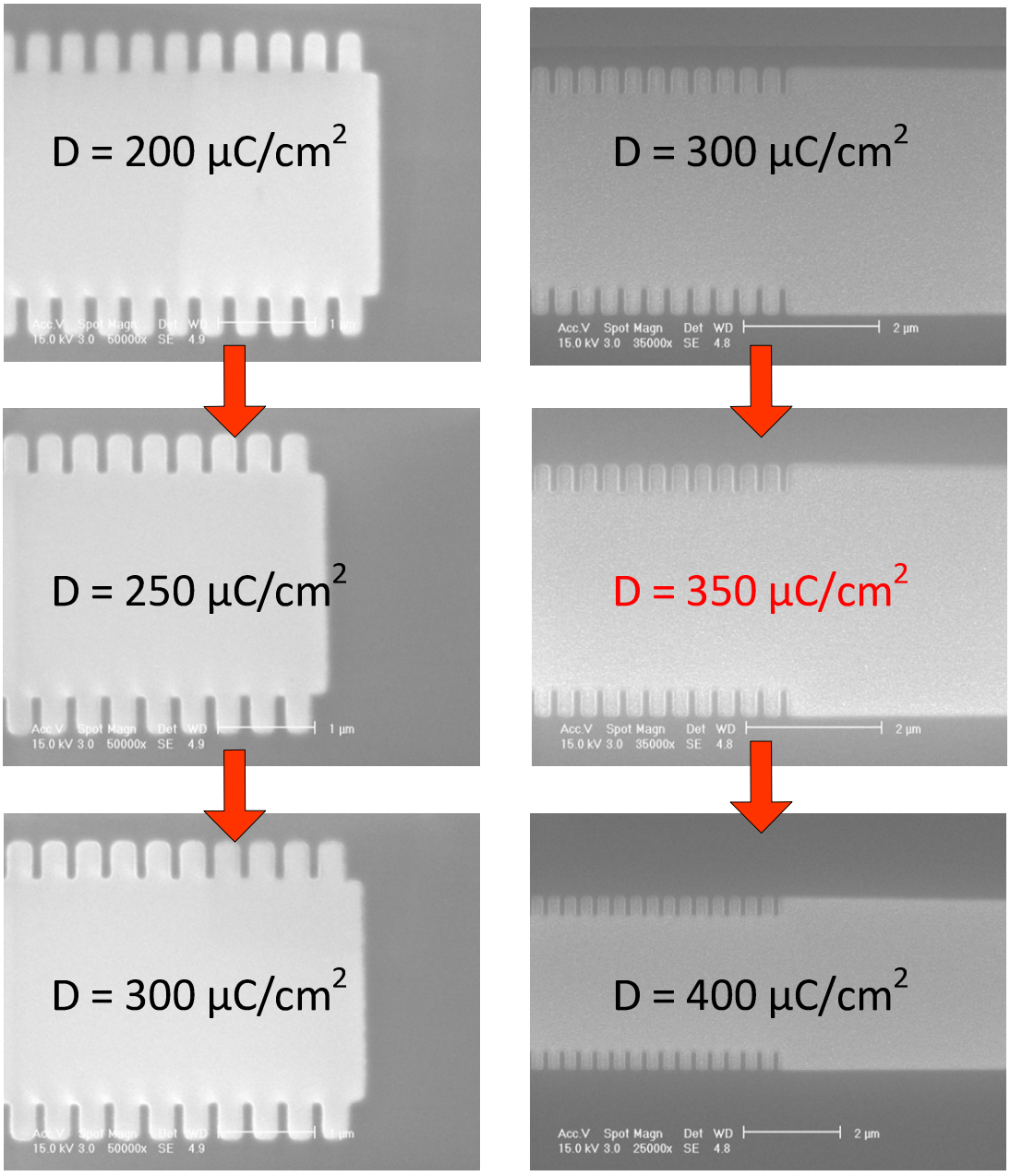

Fig. 3.7. SEM images for dose test on 3% PMMA resist.

After exposed by electron beam lithography, the sample was loaded into the RIE system for 30 seconds oxygen (O_2) ashing to remove the residual PMMA resist on the grating patterns. This will improve the grating uniformity and the adherence of metal to e deposited for liftoff process. We deposited about 30 nm chromium (Cr) on the sample surface by electron beam evaporator, supplied by Kurt J. Lesker, at an evaporation rate of 3 A/s. The sample is put face-down in a beaker of acetone. After 2 minute, the beaker is moved into the ultrasonic cleaner for an additional 3 seconds to liftoff the chromium. The measured gratings period is 350 nm, grating depth is 410 nm, low-index width is 190 nm, and the corresponding duty cycle is 190/350 = 0.54, as shown in Fig. 3.8, are in fabrication tolerance to our designed parameters.

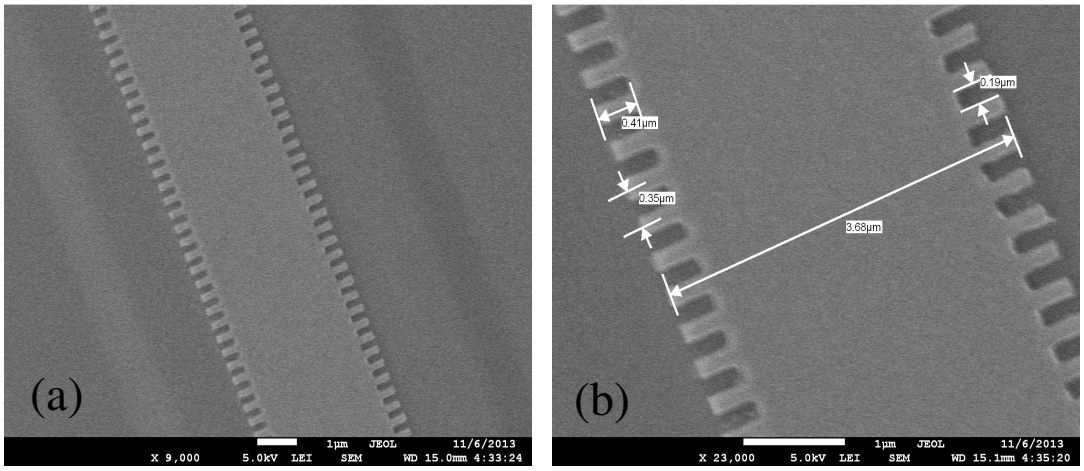

Fig. 3.8. SEM images of sidewall gratings after Cr liftoff process.

The chromium after liftoff acts as dry etching mask during reactive ion etching of As_2S_3 layer and its above protection layer. We started the etching with the same recipe

as titanium etching but without argon gas fir the first 2 minutes and continue etching with argon gas at a flow rate of 5 sccm for another 3 minutes. The RF power is 100 W and ICP power is 200 W. Chamber pressure is 10 mTorr and temperature is 15 ºC. CHF_3 gas flow is 25 sccm. The etch rate for As_2S_3 is about 20 A/s and 15 A/s for SiO_2.

After RIE etching of the sample, 5% hydrofludic (HF) chemical etching is used to remove the protection layer and the Cr etch mask. Scanning electron microscope (SEM) images of final fabricated As_2S_3 sidewall gratings and linear tapers are shown in Fig. 3.9. The integrated As_2S_3 sidewall gratings were aligned down the midline of Ti-diffused $LiNbO_3$ optical waveguide. Note that there is a small bump on the Ti:$LiNbO_3$ channel waveguide surface because of the imperfect titanium diffusion. The bump is uneven and degrades the optical quality of As_2S_3-$LiNbO_3$ interface, resulting in excess waveguide propagation loss. However, this can be improved by performing chemical-mechanical planarization (CMP) right after Ti diffusion process to obtain a smooth surface.

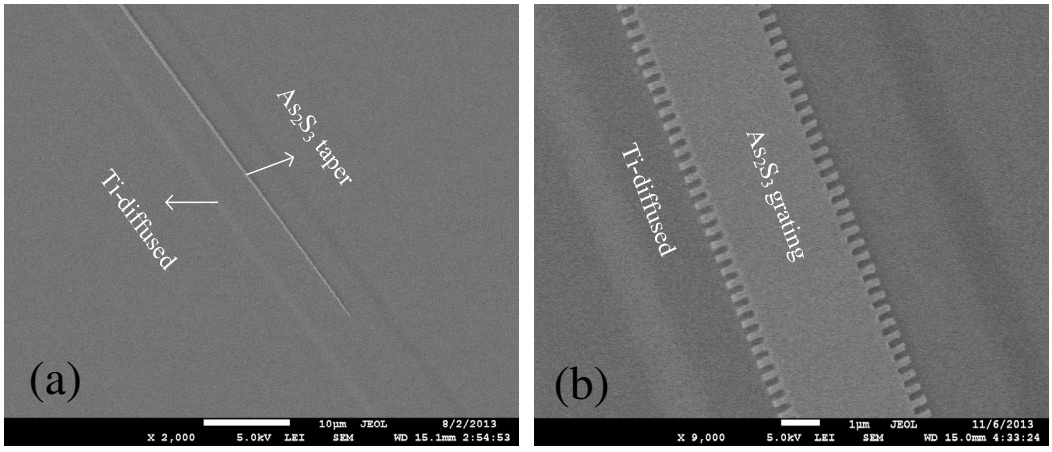

Fig. 3.9. Fabricated (a) As_2S_3 linear tapers and (b) As_2S_3 sidewall gratings.

3.3 As_2S_3 Vertical Tapers

To couple the mode from Ti:$LiNbO_3$ waveguide to the hybrid As_2S_3-Ti:$LiNbO_3$ waveguide, linear tapers are designed. Lateral tapers with their lateral width gradually changing along the propagation distance are often used for this purpose because of simple fabrication. However, vertical tapers exhibit a much higher coupling efficiency for our vertically-integrated hybrid optical waveguides. Therefore, as a first attempt, we designed a shadow-mask assembly to fabricate vertical linear tapers by magnetron sputtering as sketched by Fig. 3.10. During the sputtering deposition, the sputtered atoms coming out of the source target are blocked by the 1 mm thick aluminum mask, resulting in a vertically-tapering deposition profile within the shadow of aluminum mask. The spacing between aluminum mask and substrate is adjusted by using a stack of Teflon spacers of 125 nm height. To obtain a smooth surface on the vertical taper, the lower corner is slanted at 45 degrees to minimize the edge scattering effects.

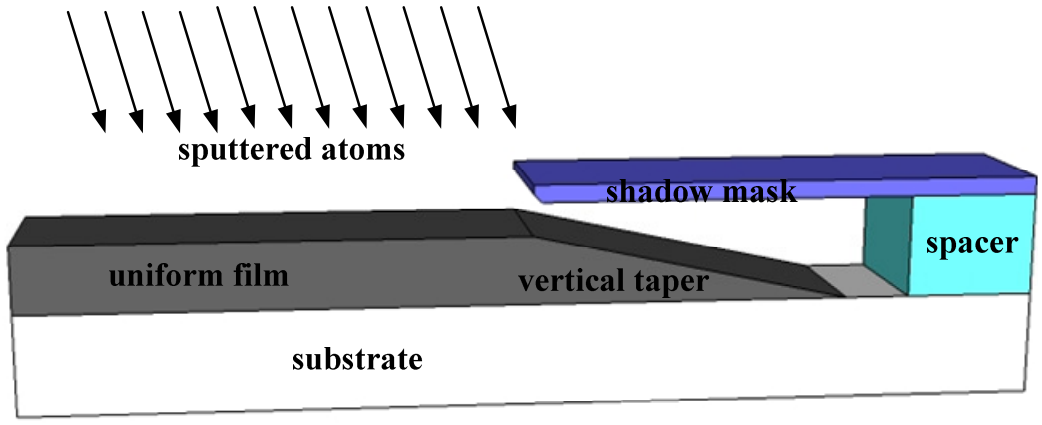

Fig. 3.10. Schematics of self-designed shadow-mask deposition assembly.

We tested our self-designed shadow-mask deposition assembly by depositing 350 nm thick silicon dioxide on lithium niobate and measured the surface profile with Dektak 150 surface profiler. Fig. 3.11 shows one of measurements on fabricated samples. The taper length is 2.5 mm and height changes smoothly from 0 to 350 nm. By linear fitting, we obtained a slope at 0.00015, corresponding to a tapering angle of less than 0.5 degree. This angle is dependent on spacer thickness. It can also be further adjusted by appropriately orienting the substrate surface with respect to the sputtered atom direction. It is expected that such vertical tapers experience low transition loss for vertical mode coupling between titanium-diffused channel waveguide to arsenic tri-sulfide strip waveguide.

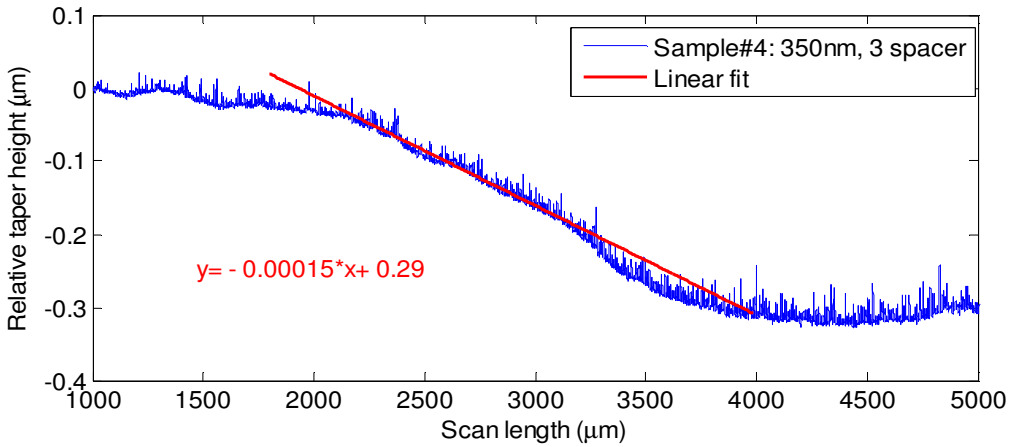

Fig. 3.11. Measured surface profile of a fabricated vertical taper.

The designed mechanical assembly as well as the spacer geometry, shadow mask geometry and wafer holder geometry are given in Appendix A.

CHAPTER IV

RESULTS AND DISCUSSION*

There are three topics covered in this chapter. Firstly, a hybrid waveguide structure is designed for efficient mid-infrared difference frequency generation at 4.0-4.9 μm via type-I and type-IV phase-matching. The design principle, material matching, waveguide loss, and power conversion efficiency are investigated. Secondly, the design, fabrication and measurement of integrated sidewall gratings in hybrid As_2S_3 on Ti-diffused $LiNbO_3$ optical waveguides (As_2S_3-Ti:$LiNbO_3$) are discussed in details. Uniform gratings, phase-shifted gratings and grating cavities are considered. The effects of waveguide and grating parameters on reflection bandwidth are discussed. Coupling coefficients are calculated by overlap integration and compared with abstracted values from numerical fittings. The final topic is on the design of optical refractive index sensors with phase-shifted sidewall gratings in silicon-on-insulator (SOI) slot waveguide. It is theoretically demonstrated that such optical refractive index sensors has a high sensitivity at the order

---

* Part of this chapter is reprinted with permission from "Chalcogenide As_2S_3 sidewall Bragg gratings integrated on $LiNbO_3$ substrate," X. Wang, A. Jiang, and C. K. Madsen, Opt. and Photon. J. **3**, 78-87, 2013, copyright 2013 by Scientific Research Publishing Inc.
Part of this chapter is reprinted with permission from "Highly sensitive compact refractive index sensor based on phase-shifted sidewall Bragg gratings in slot waveguide," X. Wang and C. K. Madsen, Appl. Opt. **53**, 96-103, 2014, copyright 2014 by OSA.
Part of this chapter is reprinted with permission from "Fabrication and measurement of sidewall gratings integrated in hybrid As_2S_3-Ti:$LiNbO_3$ optical waveguides," X. Wang, Y. Zhou, and C. K. Madsen, J. Lightwave Technol. **32**, 2989-2995, 2014, copyright 2014 by IEEE.
Part of this chapter is reprinted with permission from "Design of a hybrid As_2S_3-Ti:$LiNbO_3$ optical waveguide for phase-matched difference frequency generation at mid-infrared," X. Wang and C. K. Madsen, Opt. Express, to be published, 2014, copyright 2014 by OSA.

of 10^{-6}, a linear response, a compact device dimension as small as 11.7 μm, and a dynamic detection range as wide as 1.32 RIU (refractive index unit).

4.1 Mid-infrared DFG Waveguide

This section shows the design and simulation of a novel hybrid waveguide structure with chalcogenide arsenic tri-sulfide on a titanium-diffused lithium niobate for efficient mid-infrared emission at 4.0-4.9 μm by phase-matched difference frequency generation (DFG). Two types of phase-matching schemes are used for efficient DFG process in z-cut y-propagating $LiNbO_3$ substrate: type-I (o + e → e) and type-IV (e + e → e).

4.1.1 Type-I waveguide design

As aforementioned in the introduction section, both chalcogenide As_2S_3 and $LiNbO_3$ are excellent materials for mid-infrared (mid-IR) applications. Here, we designed a novel hybrid waveguide using arsenic tri-sulfide on titanium-diffused lithium niobate for mid-IR difference frequency generation (DFG). Besides, we also used magnesium fluoride (MgF_2, 0.11-7.5 μm) and aluminum nitride (AlN, 0.2-6.5 μm) in the waveguide design. As illustrated in Fig. 4.1(a), the hybrid waveguide consists of three dielectric thin films (As_2S_3-MgF_2-As_2S_3) on Ti-diffused $LiNbO_3$. Here, 95 nm-thick 7 μm-wide Ti strips are diffused in the *z*-cut $LiNbO_3$ for 10.5 hours at 1025 °C. t_1, t_2, and t_3, respectively, are thicknesses of lower As_2S_3 slab, MgF_2 buffer layer and upper As_2S_3 slab; w and h denotes the width and height of the AlN ridge.

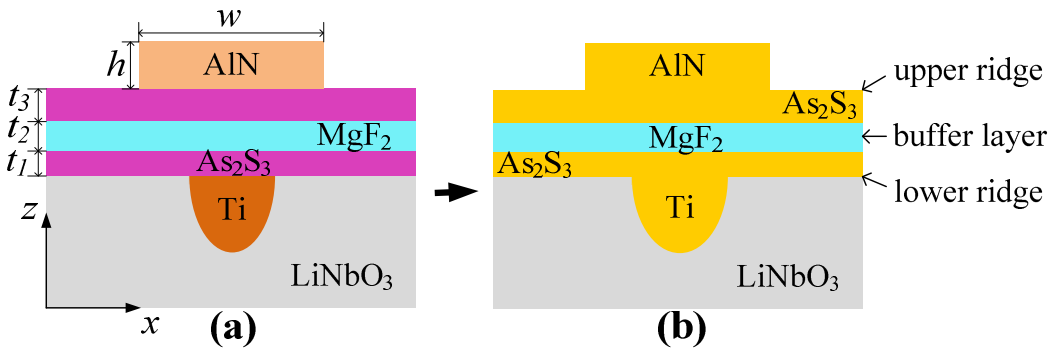

Fig. 4.1. Schematics of (a) hybrid As_2S_3-Ti:$LiNbO_3$ waveguide and (b) the equivalent ridge waveguides model.

Figure 4.2 plots the refractive indices of the waveguide materials in their corresponding transmission windows. MgF_2 possesses the lowest refractive index and is used as a buffer medium in hybrid waveguide structure. For type-I phase-matching scheme, the second-order nonlinear susceptibility element d_{31} = 4.64 pm/V of the z-cut $LiNbO_3$ crystal is utilized [84]. The AlN ridge is designed to provide lateral mode confinement at mid-infrared. The low-index MgF_2 buffer layer is sandwiched between two high-index As_2S_3 slabs. The functionality of this buffer layer is in dual sense. It firstly tightens the mode confinement of pump and signal waves at near-infrared by increasing effective index. Meanwhile, it tends to pull up a guided mode from the lower As_2S_3 slab and Ti diffused region so that the mode is confined and guided by the whole hybrid waveguide.

To minimize propagation loss as well as to optimize effective interaction area, the hybrid waveguide should be at single-mode operation. Note that, in Fig. 4.2, the ordinary refractive index (n_o) of AlN is close to the extraordinary refractive index (n_e) of $LiNbO_3$.

This facilitates us to model the hybrid waveguide as two ridge waveguides that are placed back to back to low-index MgF_2 buffer layer as in Fig. 4.1(b). Consequently, we can treat the hybrid waveguide structure as a loaded slot waveguide formed by the two equivalent ridge waveguides [85].

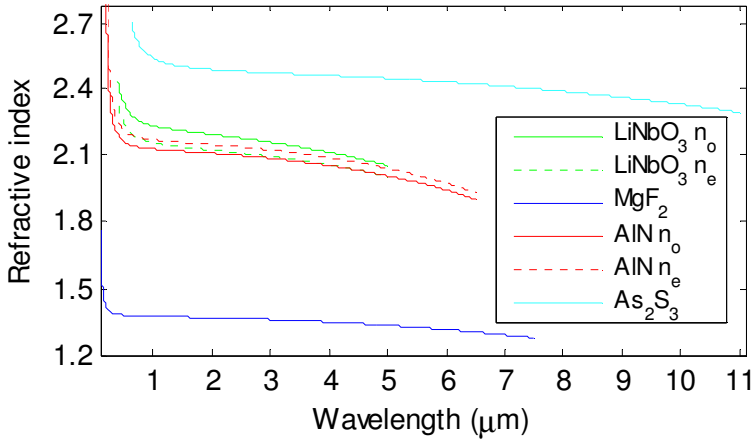

Fig. 4.2. Refractive indices of the waveguide materials.

We first estimated the thickness of lower As_2S_3, t_1, by optimizing single-mode operation for the equipment ridge waveguide made by lower As_2S_3 slab. As Ti diffusion increases the refractive indices of $LiNbO_3$, the upper As_2S_3 thickness, t_3, was adjusted accordingly to maintain the waveguide symmetry. After optimization, the As_2S_3 thicknesses were fixed at t_1 = 230 nm and t_3 = 240 nm and the MgF_2 layer thickness is variable depending on phase-matching condition. The AlN ridge is optimized at h = 4 μm and w = 16 μm. Fig. 4.3 shows calculated effective indices of the hybrid waveguide with film-mode matching (FMM) tools in FIMMWAVE (Photon Design Inc. UK). Vertical dotted line indicates the cutoff wavelength for high order modes. The cutoff

wavelength is 1.95 µm for transverse electric (TE) polarization and 1.38 µm for transverse magnetic (TM) polarization. In this work, we used a TE-polarized signal at λ_s = 2.05 µm (e) and a TM-polarized pump at λ_p = 1.42 µm (o) as input to the designed hybrid waveguide. The DFG idler wave is also TE-polarized (e) with the wavelength determined by energy conservation [86].

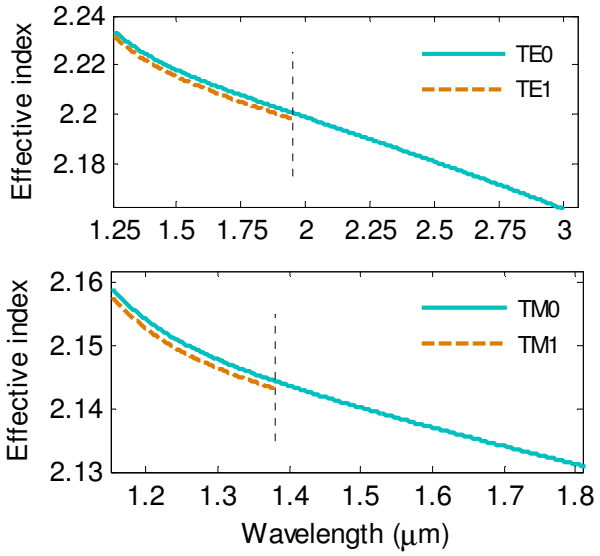

Fig. 4.3. Mode effective indices of the final designed hybrid waveguide.

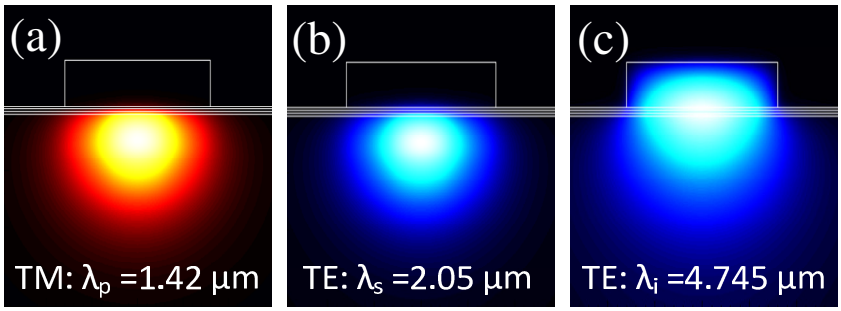

Fig. 4.4. Electric field distributions of (a) pump, (b) signal and (c) idler waves.

As displayed by Fig. 4.4, transverse electrical fields $\boldsymbol{E_z}$ for TM pump and $\boldsymbol{E_x}$ for TE signal are largely confined by the equivalent lower ridge waveguide. The output mid-IR idler is confined by the whole hybrid waveguide. However, the TM mode is less confined with a larger electric field profile than the TE mode and has a lower effective index as seen in Fig. 4.3. As a result, the TM mode penetrates the low-index MgF_2 buffer layer much more than the TE mode. At the same time, the TE mode of mid-IR idler was confined by a slot waveguide formed by two equivalent ridge waveguides, so the idler wave is significantly affected by the MgF_2 buffer layer thickness [28, 85].

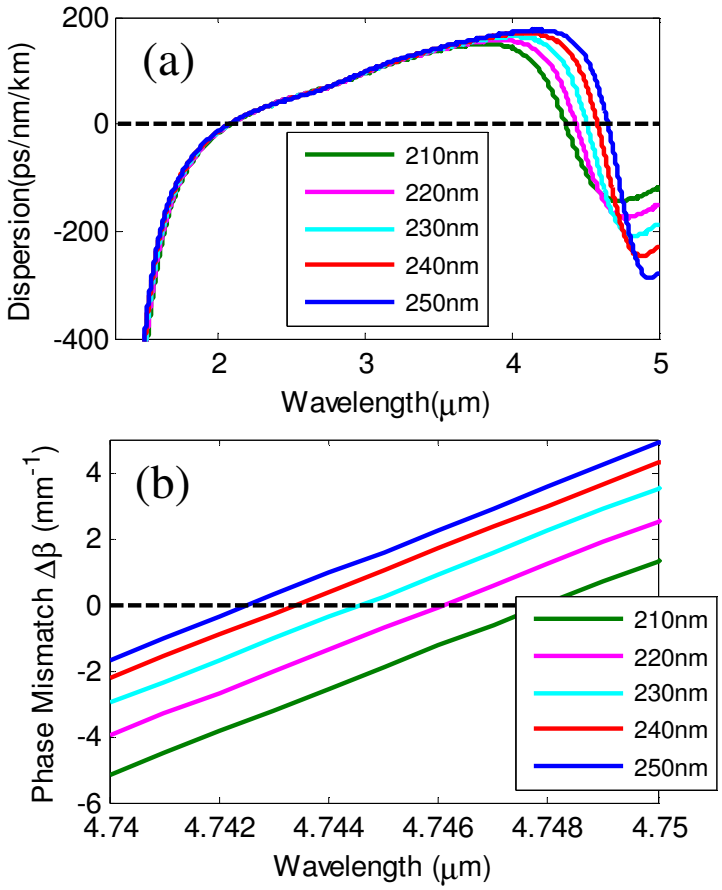

Fig. 4.5. (a) Dispersion and (b) phase mismatch at different buffer thickness.

Figure 4.5 shows the effects of MgF_2 buffer layer on dispersion and phase mismatch. In general, the dispersion is -200~200 ps/nm/km in wavelength conversion band from 2.05 μm to 4.745 μm. As expected, the buffer layer shifts zero-dispersion wavelengths (ZDWL) at mid-IR, which alters phase-matching condition for efficient DFG process [86]. This provides an alternative way to expanding mid-IR tunability.

4.1.2 Type-I conversion efficiency

The interaction between signal, pump and idler waves is governed by associated coupled-mode equations. With continuous-wave (CW) pump and signal, the power-normalized DFG conversion efficiency under the non-depletion approximation can be rigorously derived from the following coupled-mode equations [86, 87].

$$\frac{\partial A_p}{\partial y}+\frac{c}{n_{gp}}\frac{\partial A_p}{\partial t}=-\frac{\alpha_p}{2}A_p+j\frac{2\pi c}{\lambda_p}\kappa A_s A_i \exp(-j\Delta\beta y) \tag{4.1}$$

$$\frac{\partial A_s}{\partial y}+\frac{c}{n_{gs}}\frac{\partial A_s}{\partial t}=-\frac{\alpha_s}{2}A_s+j\frac{2\pi c}{\lambda_s}\kappa A_p A_i^* \exp(j\Delta\beta y) \tag{4.2}$$

$$\frac{\partial A_i}{\partial y}+\frac{c}{n_{gi}}\frac{\partial A_i}{\partial t}=-\frac{\alpha_i}{2}A_i+j\frac{2\pi c}{\lambda_i}\kappa A_p A_s^* \exp(j\Delta\beta y) \tag{4.3}$$

Here, the power is defined by $P_q = |A_q|^2$ (q = s, p, i) where $\boldsymbol{A_q}$ is the normalized complex amplitudes of signal, pump waves and average normalized complex amplitude of mid-IR idler wave. L is the hybrid waveguide device length; c is the vacuum speed of light. n_{gq}, β_q and α_q are group indices, propagation constants and loss coefficients for pump, signal and idler waves, respectively. $\Delta\beta = \beta_p - \beta_s - \beta_i$ is the phase mismatch. κ

refers to DFG coupling coefficient that is determined by nonlinear coefficient d_{31}, effective indices n_q, and effective DFG interaction area A_{eff}, as expressed by

$$\kappa = d_{31}\sqrt{2\mu_0 /(cn_p n_s n_i A_{eff})} \tag{4.4}$$

Here, μ_0 is the vacuum permeability. The effective DFG interaction area A_{eff} is evaluated by taking overlap integration between distributions of transverse electric fields $\boldsymbol{E_q(x, z)}$ and refractive index $n(x, z)$ in the waveguide, as described by Eq. (4.5) where Δ and Ω indicate $LiNbO_3$ area and the whole hybrid waveguide, respectively.

$$A_{eff} = \frac{n_i^2 \int_\Omega n^2(\lambda_p)E_p^2 dxdz \int_\Omega n^2(\lambda_s)E_s^2 dxdz \int_\Omega n^2(\lambda_i)E_i^2 dxdz}{n_p^2 n_s^2 \left|\int_\Delta n^2(\lambda_i)E_p E_s E_i dxdz\right|^2} \tag{4.5}$$

The DFG power conversion is given by

$$\eta_{norm} = \left(\frac{2\kappa\pi c}{\lambda_i}\right)^2 \cdot \exp[-(\alpha_p + \alpha_s + \alpha_i)L/2] \cdot \frac{\sin^2(\Delta\beta L/2) + \sinh^2(\alpha_p + \alpha_s - \alpha_i)L/4)}{(\Delta\beta L/2)^2 + [(\alpha_p + \alpha_s - \alpha_i)L/4)]^2} \tag{4.6}$$

As_2S_3 on Ti:$LiNbO_3$ optical waveguide was reported with α = 0.25 dB/cm at 1.55 μm [15, 88], here we assumed α = 1 dB/cm at near-infrared. Low-loss As_2S_3 waveguide on bare $LiNbO_3$ was also fabricated with α = 0.33 dB/cm at 4.8 μm [14]. Because slot waveguide generally experiences higher loss than strip and rib waveguide, we used a typical value α = 6.5 dB/cm at mid-IR [89]. Fig. 4.6 displays the calculated mid-IR idler powers on the hybrid waveguide pumped at P_p = P_s = 50 mW. The conversion efficiency η increases with waveguide length and reaches a maximum value at 0.23%W^{-1} for L = 16 mm. The power conversion efficiency is limited by waveguide loss when L is

beyond 16 mm. The full-width half-maximum (FWHM) linewidth, $\Delta\lambda$, of the mid-IR idler wave decreases with the waveguide length. For L = 6 mm, the idler power at 4.745 µm is -25.5 dBm (i.e., 2.8 µW) with $\Delta\lambda$ = 2.13 nm and η = 0.11% W^{-1}. At L = 16 mm, the idler power is increased to ~5.8 µW and the linewidth is suppressed to 0.56 nm. The impact of parametric noise due to spontaneous emission, power fluctuations and two-photon absorption is only 1 nW at 150 mW power at near-IR [32, 90]. Without introducing any additional noise, the output idler power can be improved to ~52 µW at $P_p = P_s$ = 150 mW. A broad mid-IR tuning range from 3.3 µm to 4.9 µm is theoretically calculated with a tunable signal laser. The mid-IR tunability can be further extended by applying thermal-optic and electro-optic effects of $LiNbO_3$ crystal.

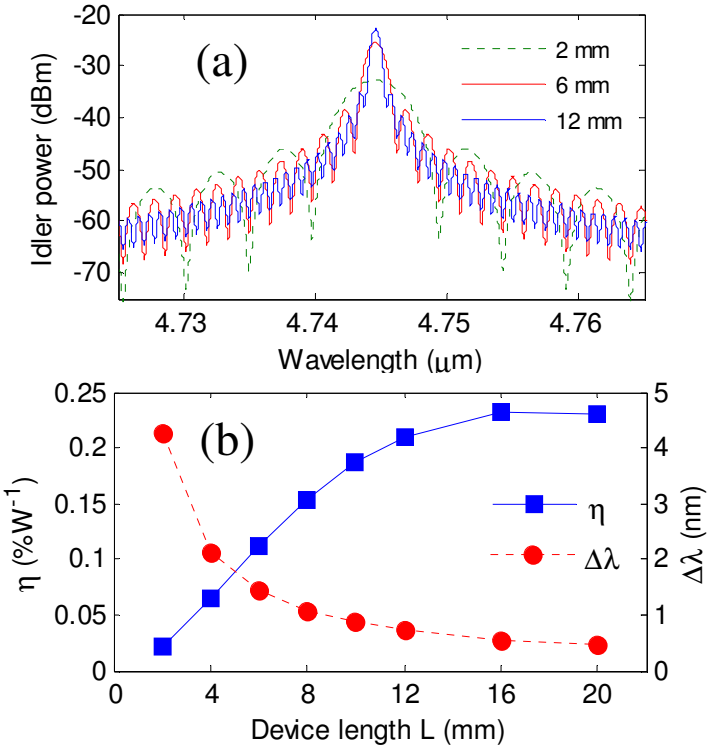

Fig. 4.6. (a) Power of idler wave and (b) DFG conversion efficiency.

4.1.3 Type-IV waveguide design

To utilize the largest second-order nonlinear susceptibility element d_{33} = 30 pm/V of z-cut y-propagating $LiNbO_3$ crystal [84], type-IV phase-matching has to be satisfied. As discussed above, the functionality of low-index MgF_2 buffer layer is in dual sense. First, the near-infrared mode behaviors of the two equivalent ridge waveguides are almost independent of each other as a result of low-index gap. Second, the buffer layer tends to pull up a mid-infrared mode from the lower ridge waveguide so that the mid-infrared mode is confined and guided by the whole hybrid waveguide. This facilitates us to design a hybrid waveguide supporting only fundamental modes to optimize the wavelength conversion efficiency. Here, a TE-polarized signal wave at wavelength λ_s = 2.05 μm (e) and a TE-polarized pump wave at wavelength λ_p = 1.42 μm (e) as input to the designed type-IV optical waveguide to generate a TE-polarized idler wave (e).

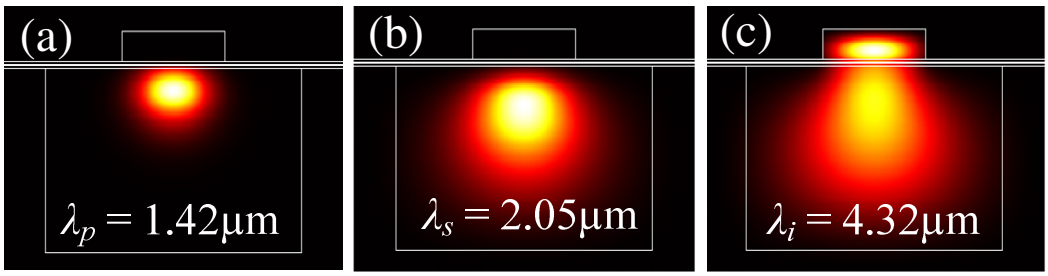

Fig. 4.7. Mode intensity profiles of (a) pump, (b) signal and (c) idler waves.

Similar to the type-I waveguide design, after optimization, the As_2S_3 film thicknesses were fixed at t_1 = 220 nm and t_3 = 230 nm. The MgF_2 layer thickness, t_2, is variable between 140 nm and 190 nm, which affects transverse electric field distribution of mid-

infrared idler wave and plays a critical role in satisfying phase-matching condition. The AlN ridge is designed at h = 3 μm and w = 12 μm to provide lateral mode confinement for mid-infrared idler. Fig. 4.7 shows the calculated mode intensity profiles for pump, signal and idler waves of the designed type-IV hybrid optical waveguide. Both pump and signal with relatively higher mode effective indices are tightly confined by the lower ridge waveguide. The pear-like idler at mid-infrared wavelength 4.32 μm is confined by the whole hybrid waveguide structure.

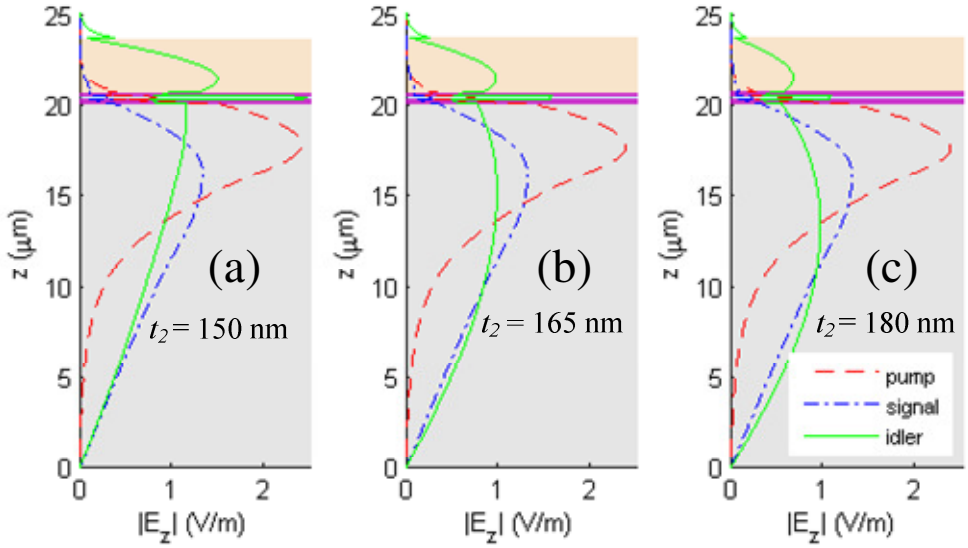

Fig. 4.8. Transverse electric field amplitude profiles at different t_2.

The amplitude profiles of transverse electric fields for the interacting signal, pump and idler waves in the hybrid waveguide with different buffer layer thicknesses are shown in Fig. 4.8. On the one hand, the MgF_2 buffer layer thickness (or slot width in the equivalent ridge waveguides model) does not affect much transverse electric field

amplitude profiles for near-infrared modes that are strongly confined in titanium-diffused $LiNbO_3$. On the other hand, the transverse electric field distribution of a mid-infrared mode significantly depends on the slot width. Narrower slot widths provide a higher electric field confinement in the slot region, but less overlap between interacting waves. Optimal modal overlap between pump, signal and idler was achieved with the MgF_2 buffer layer of a thickness at t_2 = 165 nm.

4.1.4 Type-IV conversion efficiency

The conversion efficiency of type-IV hybrid waveguide is theoretically predicted by Eq. (4.6) considering the waveguide loss. Fig. 4.9 demonstrates effect of the low-index MgF_2 buffer layer on phase mismatch. As expected, the buffer layer shifts phase-matching condition required for efficient DFG [32]. Thicker buffer layer results to an idler wave near a relatively shorter wavelength because thicker buffer layer leads to smaller effective index for the mid-infrared wave. This, however, provides an extra approach to expanding the mid-infrared tuning range [28].

The DFG output power in dBm from the designed hybrid waveguide at different device lengths is given in Fig. 4.10 where the pump powers are P_p = P_s = 50 mW. Longer waveguides gives higher power and narrower linewidth of the output idler wave. For L = 4 mm, the idler power near 4.318 μm is -12 dBm (i.e., 64.5 μW). This power can be easily improved ~0.4 mW at L = 16 mm.

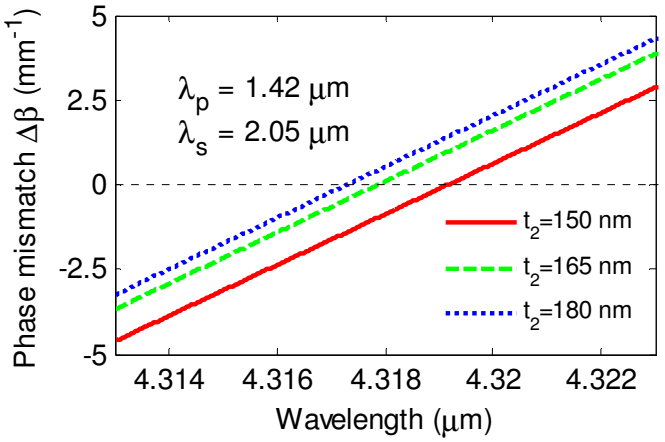

Fig. 4.9. Effect of the buffer layer thickness on the phase-mismatch.

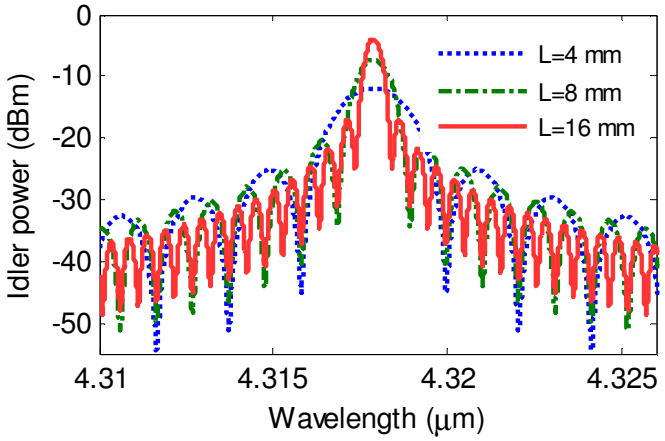

Fig. 4.10. DFG idler power of the designed hybrid waveguide pumped at 50 mW.

Another way of increasing idler power is to use higher pump powers, which may introduces unwanted parametric noise due to spontaneous emission, power fluctuations and two-photon absorption in the hybrid waveguide. However, the parametric noise is only ~1 nW at 150 mW powers at near-infrared for $LiNbO_3$ [32]. Therefore, higher idler

power of mWs can be obtained. The idler power near 4.318 μm is ~3.6 mW when 150 mW pump and signal powers are applied to a 16 mm-long hybrid waveguide.

The mid-infrared idler wave can be continuously tuned by using a tunable signal wave or pump wave or both, as shown in Fig. 5(c) and (d). For instance, using a tunable near-infrared pump laser that covers a wavelength ranging from 1.38 μm to 1.47 μm and a fixed signal wave near λ_s = 2.05 μm (e.g., Thulium lasers) as input to the waveguide, the wavelength of output idler can be continuously tuned between 4.0 μm and 4.9 μm.

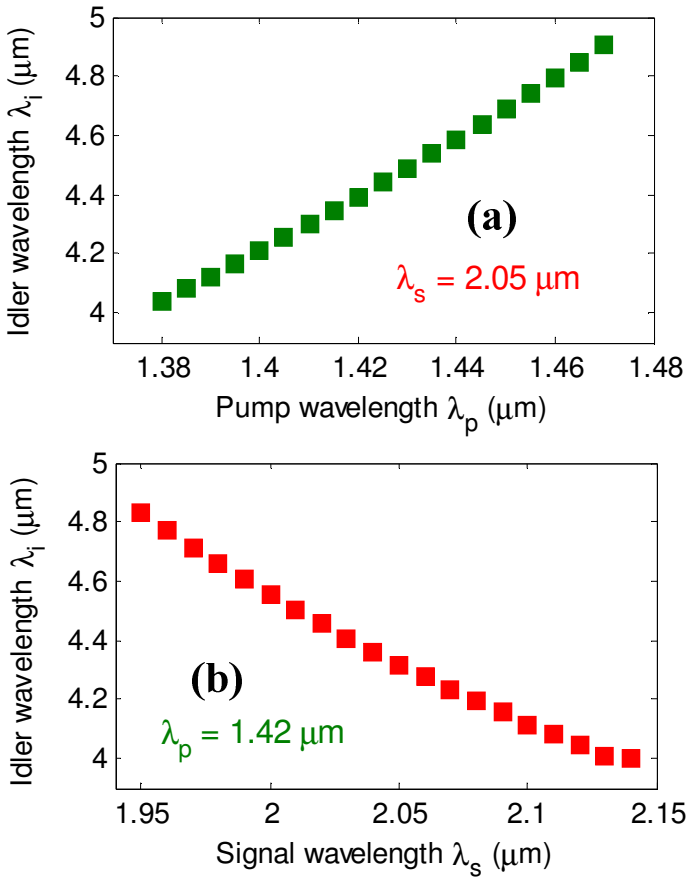

Fig. 4.11. Tuning mid-infrared idler wave with tunable (a) pump and (b) signal.

To investigate the effect of waveguide loss on the DFG power conversion efficiency, we considered the DFG power conversion efficiency given by $\eta = \eta_{norm}L^2$. Fig. 6 plots such conversion efficiency and full-width half-maximum (FWHM) spectral linewidth, $\Delta\lambda$, of the mid-infrared idler wave generated from the hybrid waveguide pumped at $P_p = P_s$ = 50 mW at different waveguide device lengths. It shows that conversion efficiency firstly increases with increased waveguide length before it reaches an optimal value ~20%W^{-1} at L = 26 mm. For waveguide longer than 26 mm, the conversion efficiency will be limited to waveguide loss. The inewidth decreases as L increases. For a 4 mm-long waveguide, $\Delta\lambda$ is 1.8 nm and η is 2.6%W^{-1}. At L = 16 mm, $\Delta\lambda$ is suppressed to ~0.46 nm and the conversion efficiency is increased to 16.1%W^{-1}.

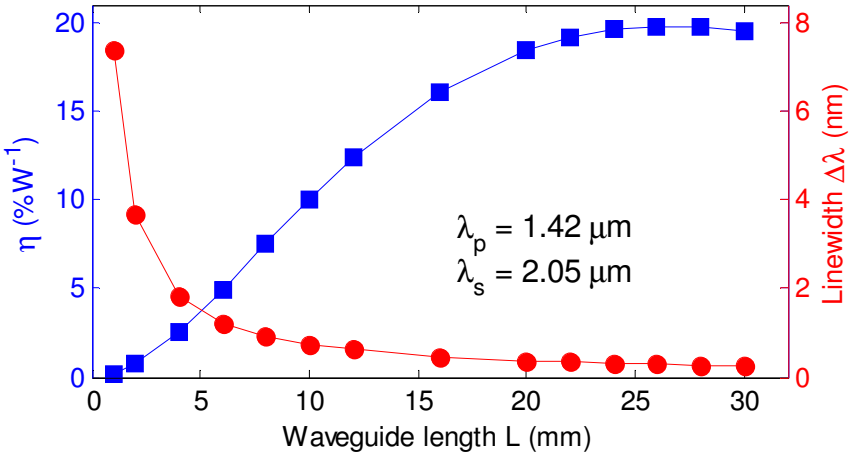

Fig. 4.12. Conversion efficiency and linewidth of output idler as a function of waveguide length at 50 mW pump powers.

For comparison, Table 4.1 summarizes the normalized DFG power conversion efficiencies of some mid-infrared DFG waveguides. The proposed hybrid waveguide

operates at single mode for all signal, pump and idler waves. The signal and pump wave is highly confined by titanium-diffused waveguide while the generated mid-infrared idler wave is confined by the whole hybrid waveguide. On a 1 mm-long hybrid waveguide pumped at 50 mW signal and 50 mW pump, a normalized power conversion efficiency of 20.52%$W^{-1}cm^{-2}$ was theoretically predicted near 4.32 μm. This efficiency is comparable to that of suspended GaAs waveguide in [91] and is almost one order of magnitude higher than that of direct-bonded Zn:$LiNbO_3$ ridge waveguide in [31]. To the best of our knowledge, this is the highest efficiency record for mid-infrared DFG waveguide designs on $LiNbO_3$ substrate. Besides, a continuously-tunable wavelength range at mid-infrared 4.0-4.9 μm can be achieved by using tunable near-infrared pump or signal lasers. In addition, such hybrid As_2S_3-Ti:$LiNbO_3$ waveguides can be fabrication in just a few CMOS-compatible steps by thin film deposition, photolithography, etching, thermal diffusion and polishing [15, 18, 19].

Table 4.1. Conversion Efficiencies (CE) of Some Mid-IR DFG Waveguides.

Waveguide structures	λ_p *(μm)*	λ_s *(μm)*	λ_i *(μm)*	L *(mm)*	η_{norm} *(%$W^{-1}cm^{-2}$)*
Ti-diffused PPLN [32]	1.1	1.55	3.8	80	1.08
Direct-bonded $LiNbO_3$ ridge [30]	1.0	1.55	3.2	50	1.60
Direct-bonded Zn:$LiNbO_3$ ridge [31]	1.064	1.55	3.4	38	2.42
Bulk PPLN [29]	1.064	~0.8	3-4.1	6	0.17
AlGaAs/GaAs multilayer [93]	~0.945	~1.54	2.36-2.53	3.8	0.29
Suspended GaAs [91]	~1.025	~1.55	2.8-3.15	1.2	27.78
AlGaAs/AlAs multilayer [27]	1.0	1.32	4.04	1.2	2.98
Multilayer AlGaAs [92]	1.55	1.95	7.5	1	0.012
Suspended AlGaAs [28]	1.06	1.554	3.41	1	0.16*
Proposed hybrid As_2S_3-Ti:$LiNbO_3$	~1.42	~2.05	4.0-4.9	1	20.52*

*Note: (1) * indicates a theoretical value; (2) ~ denotes a tunable laser.*

In summary, we proposed a novel hybrid waveguide for efficient mid-infrared DFG through two types of phase-matching schemes. The hybrid waveguide operates at single mode condition. The designed waveguide was modeled as a slot waveguide formed by two back-to-back ridge waveguides with a low-index buffer medium. The buffer layer was characterized such that both pump and signal waves were confined by lower ridge waveguide while the DFG output idler wave was confined by the whole hybrid waveguide structure. For type-I phase-matching, we predicted a DFG conversion efficiency of 0.11% W^{-1} near 4.745 μm (e) on a 6 mm-long waveguide using 50 mW TM pump at 1.42 μm (o) and 50 mW TE signal at 2.05 μm (e). The maximum DFG conversion efficiency is 0.23% W^{-1}, limited by waveguide loss. For type-IV phase-matching case, a normalized power conversion efficiency of 20.52%$W^{-1}cm^{-2}$ was theoretically predicted on a 1 mm-long hybrid waveguide using 50 mW pump wave at 1.42 μm (e) and 50 mW signal wave at 2.05 μm (e). This efficiency, to the best of our knowledge, is the highest efficiency record for mid-infrared DFG waveguide based on lithium niobate crystal. The maximum conversion efficiency is limited by waveguide loss for waveguide device longer than 26 mm. A broadband mid-infrared tuning range from 4.0 μm to 4.9 μm can be realized with a tunable near-infrared pump laser at 1.38-1.47 μm or a tunable signal laser at 1.95-2.15 μm. Such hybrid waveguides can provide an alternative approach of efficient mid-infrared generation with mW powers and sub-nanometer linewidths. In view of fabrication, the designed hybrid optical waveguide can be easily fabricated in only a few steps by thin film deposition, photolithography, etching, thermal diffusion and polishing. Besides, the proposed hybrid waveguide has

the potential capabilities for lab-on-a-chip integration with other electronics, couplers, sensors and detectors by low-loss fiber-coupling.

4.2 Sidewall Gratings in As_2S_3-Ti:$LiNbO_3$ Waveguide

This section will systematically discuss the design, simulation and experimental measurements of the fabricated integrated sidewall Bragg gratings in hybrid As_2S_3-Ti:$LiNbO_3$ optical waveguides.

4.2.1 Design and simulation

Fig. 4.13(a) illustrates cross-sectional view of the hybrid As_2S_3-Ti:$LiNbO_3$ waveguide that is constructed by patterning As_2S_3 strips on top of Ti-diffused channel waveguide in $LiNbO_3$. W_0 and t are the width and thickness of unperturbed As_2S_3 strip, respectively. The As_2S_3 thickness is determined at t = 280 nm for single mode operation. The unperturbed As_2S_3 width W_0 is variable from 2.6 μm to 4.6 μm, depending on grating depth. To minimize the scattering loss resulting from waveguide surface roughness, the temperature distribution in furnace, diffusion time and environmental factors were considered. It is worthy to note that the mode intensity is only partially confined in high-index As_2S_3 strip due to the hybrid nature of the As_2S_3-Ti:$LiNbO_3$ optical waveguide. For the fundamental TE_0 mode at 1.55 μm, ~38% of the light intensity is concentrated in high-index As_2S_3 region while the rest of light intensity is still confined in Ti-diffused region as seen in Fig. 4.13(b). This hybrid feature facilitates

the electro-optically tuning capabilities of sidewall gratings integrated in hybrid As_2S_3-Ti:$LiNbO_3$ waveguide.

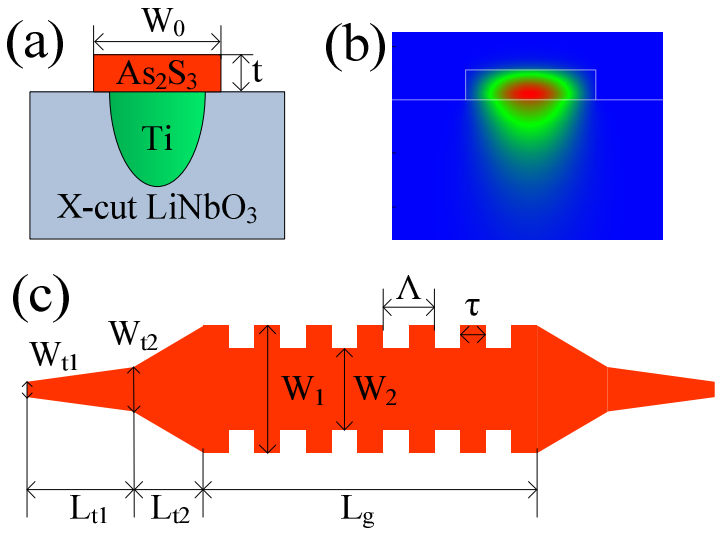

Fig. 4.13. (a) Cross-sectional view of hybrid As_2S_3-Ti:$LiNbO_3$ waveguide. (b) Mode intensity profile at 1.55 μm with W_0 = 3.2 μm. (c) Top view of sidewall gratings.

The sidewall gratings are patterned on both sidewalls of As_2S_3 strip, as displayed in Fig. 4.13(c). Here, W_1 and W_2 , respectively, represent the widest and narrowest width for the gratings. The width difference $\Delta W = (W_1 - W_2)/2$ is defined as grating depth which is a direct measure of index perturbation strength. Λ is grating period. L_g is grating length. W_1 and W_2 are the widest and narrowest width in the grating section. Here, W_{t1} and W_{t2} denote tip widths of tapers; L_{t1} and L_{t2} indicate the taper lengths. Grating period Λ is given by phase-matching: $\Lambda = \lambda_B/(2n_{eff})$ where λ_B is Bragg wavelength and n_{eff} is the mode effective index. τ is fractional length of high-index material in one grating period and the ratio τ/Λ is filling factor. Sidewall gratings have the largest coupling coefficients

at τ/Λ = 0.5. Grating length is $L_g = N\Lambda$ with N indicating the total number of periods. Following the perturbation theory, mode effective index n_{eff} can be estimated by applying $W_0 = (W_1 + W_2)/2$ for weak perturbation (i.e., $\Delta W << W_0$). For W_0 = 3.2 µm, the effective index is 2.1535 and thus the grating period is ~360 nm. To systematically investigate spectral response of sidewall gratings, it is reasonable to fix the value of W_0 and vary grating depth ΔW and grating length L_g.

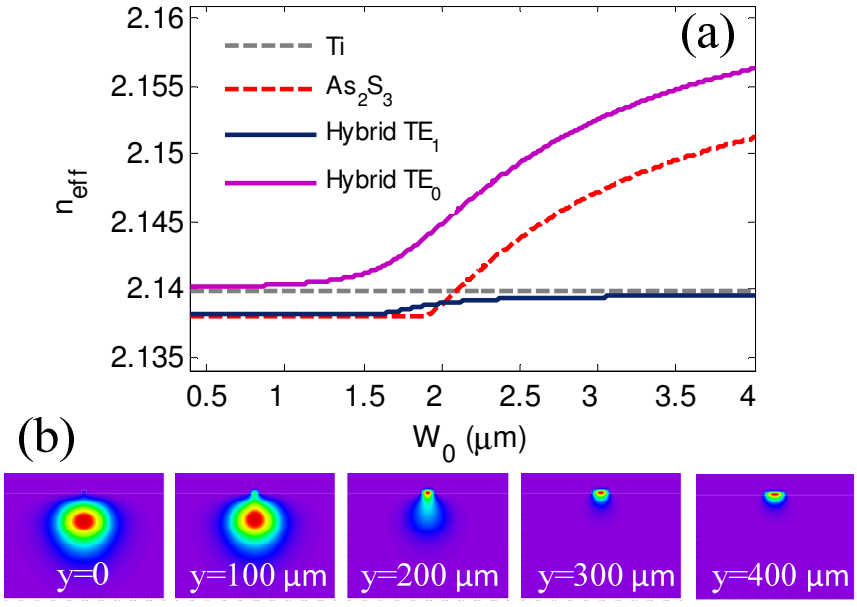

Fig. 4.14 (a) Effective indices of As_2S_3 strip and the hybrid As_2S_3-Ti:$LiNbO_3$ waveguide with varying As_2S_3 width. (b) Electric field profiles in two-stage taper. Here L_{t1} = 300 µm, W_{t1} = 0.6 µm, L_{t2} = 100 µm, W_{t2} = 1.6 µm; W_1 = 3.2 µm, and t = 280 nm.

For mode coupling between As_2S_3 strip and Ti-diffused waveguide, two-stage tapers were designed at both sides of sidewall gratings. Using the film-mode matching (FMM) tools in FIMMWAVE (Photon Design Inc., UK), effective indices of Ti waveguide,

As_2S_3 strip and the hybrid waveguide with varying As_2S_3 strip width at 1.55 μm are plotted in Fig. 4.14(a). Horizontal grey dashed line indicates the effective index of Ti waveguide. As the As_2S_3 width increases, the effective index of hybrid TE_0 mode firstly coincides with Ti waveguide and then gradually follows the trend of the mode in As_2S_3 strip [71]. The mode coupling from Ti waveguide to As_2S_3 strip starts at a critical As_2S_3 width of 0.74 μm. Thus, the first taper was designed 300μm-long with gradually varying widths from 0.6 μm to 1.6 μm. The second taper with a length of 100 μm acts as a mode size converter by transforming the mode into the gratings section. Fig. 4.14(b) also shows electric field evolution through the designed two-stage taper (along *y*-axis). At the taper end (y = 400 μm), ~100% of the mode intensity has been transferred into the hybrid As_2S_3-Ti:$LiNbO_3$ optical waveguide.

Now, let's first look at the calculated coupling coefficients by overlap integration. As depicted in Fig. 4.15, general trapezoidal sidewall gratings are engraved in both sidewalls of As_2S_3 strips on Ti:$LiNbO_3$. The grating period is Λ. Duty cycle (DC) is defined as the fractional width with high index material in one grating period and thus DC = τ/Λ where τ is the width of high index material in one period. The rise/fall width is denoted by τ_r. ΔW is the grating depth which is a measure of the index perturbation strength. W and t are the width and thickness of the equivalent unperturbed As_2S_3 strip waveguide, respectively. Arbitrary grating shape along *x*- and *z*-axis with periodic perturbation of index modulation along *y*-axis can be expressed in the form of Taylor expansion. We rewrite the formulas for Fourier coefficients and coupling coefficients for square grating profile here,

$$\Delta\varepsilon_n = \frac{4(\varepsilon_{As2S3} - \varepsilon_0)}{n\pi}\sin(\frac{n\pi\tau}{\Lambda}) \tag{4.7}$$

$$k_n = \frac{\omega}{4}\Delta\varepsilon_n \cos(nKy)\int_0^t dx\left\{\int_{(W-\Delta W)/2}^{(W+\Delta W)/2} dz\left|E(x,z)\right|^2 + \int_{-(W+\Delta W)/2}^{-(W-\Delta W)/2} dz\left|E(x,z)\right|^2\right\} \tag{4.8}$$

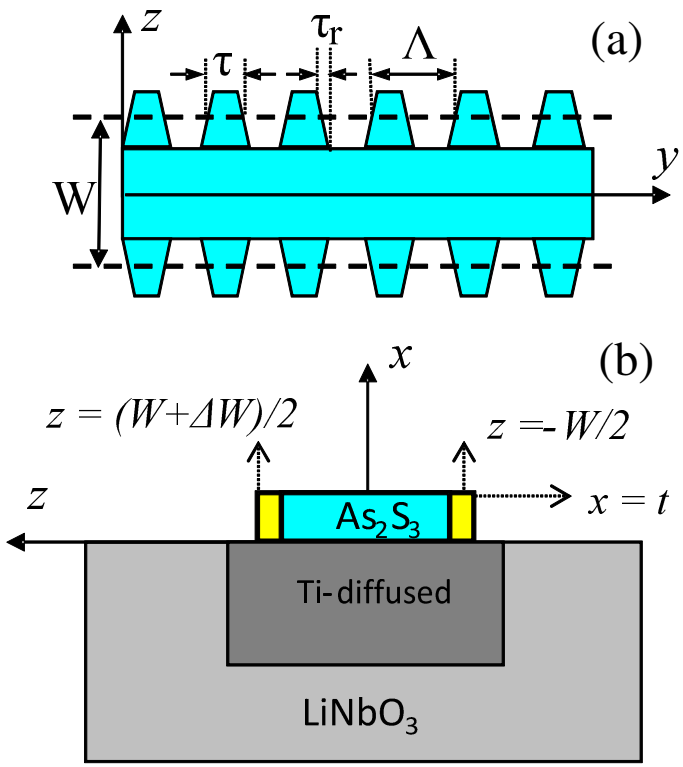

Fig. 4.15. Schematics of integrated sidewall gratings in hybrid optical waveguide.

The coupling coefficients resulting from the first-order perturbation for square, sinusoidal and trapezoidal gratings at 1.55 μm are plotted in Fig. 4.16. Red squares, green circles and blue triangles denote the square, sinusoidal and trapezoidal sidewall gratings, respectively. Square gratings have largest coupling coefficient at 8.75 mm^{-1}

because of its largest first-order Fourier coefficient. As the grating depths increases, coupling coefficient increases. For all the binary gratings, coupling coefficients are maximized when the duty cycle is 0.5.

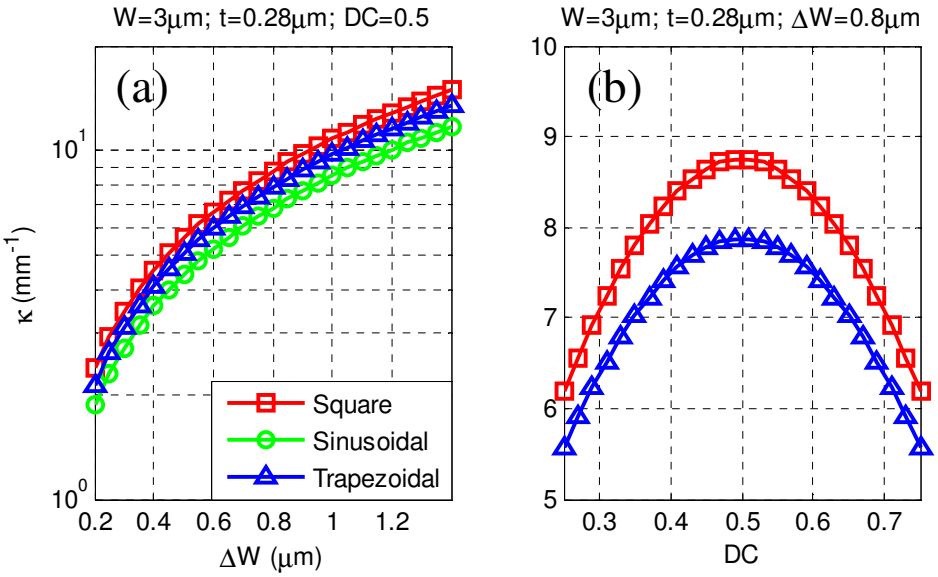

Fig. 4.16. Coupling coefficients for various grating profiles.

As discussed in Chapter II, the reflectance R and bandwidth $\Delta\lambda$ of sidewall gratings can be analytically derived from the coupled-mode equations. At 1.55 μm, numerical results for sidewall gratings under weak coupling and strong coupling are plotted in Fig. 4.17 and Fig. 4.18, respectively. Under weak coupling, the bandwidth is inversely proportional to grating length. To improve reflectance of weak coupling gratings and maintain the same grating length, larger grating depth is required. For instance, the grating reflectance for N = 600 periods can be increased from 60% to 94% by varying grating depth from ΔW = 0.4 μm to ΔW = 1.0 μm. By comparing, gratings under strong

coupling have much narrower reflection bandwidth compared with weak coupling gratings. It is also more efficient in reflectance especially at larger values of ΔW. A linear relationship between the bandwidth and the coupling coefficient beyond $\kappa > 4$ mm^{-1} is observed in Fig. 4.18.

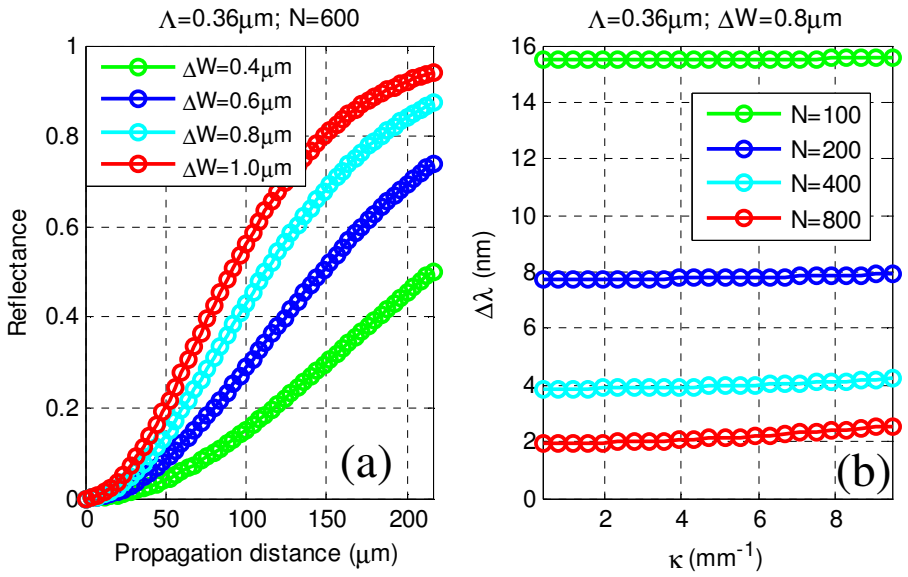

Fig. 4.17. (a) Reflectance and (b) bandwidth under weak coupling.

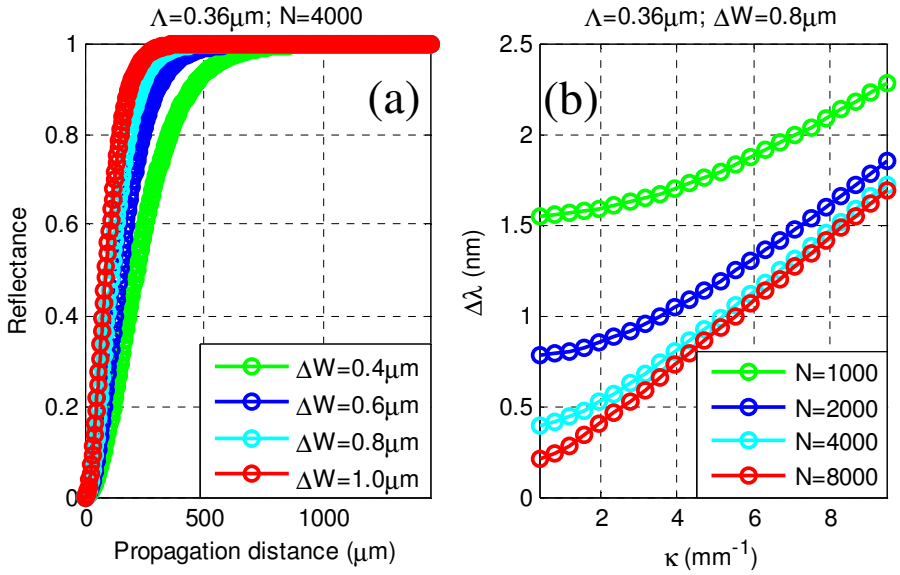

Fig. 4.18. (a) Reflectance and (b) bandwidth under strong coupling.

The uniform sidewall grating with N = 600 periods can be spitted into halves by inserting a quarter-wave spacer (i.e., the quarter-wavelength length $\lambda/(4n_{eff})$). As a result, a Fabry-Perot type of microcavity resonator is formed by two identical distributed Bragg reflectors (DBRs) [94]. A transmission peak will be created at the center of the rejection band of the uniform sidewall gratings [95, 96].

As shown in Fig. 4.19, the red line indicates the reflectance spectrum from a uniform grating with N = 600, W_0 = 3μm, ΔW = 1.0 μm and DC = 0.5 and the blue line denotes the reflectance from a phase-shifted grating. A transmission peak at 1.5472 μm with a linewidth of 0.45 nm is observed near the center of 12 nm rejection band. The quality factor (Q-factor) of this microcavity resonator is $Q = \lambda_0/\Delta\lambda = 3.4\times10^3$ which is of same order as the silicon transmission resonant filters [97].

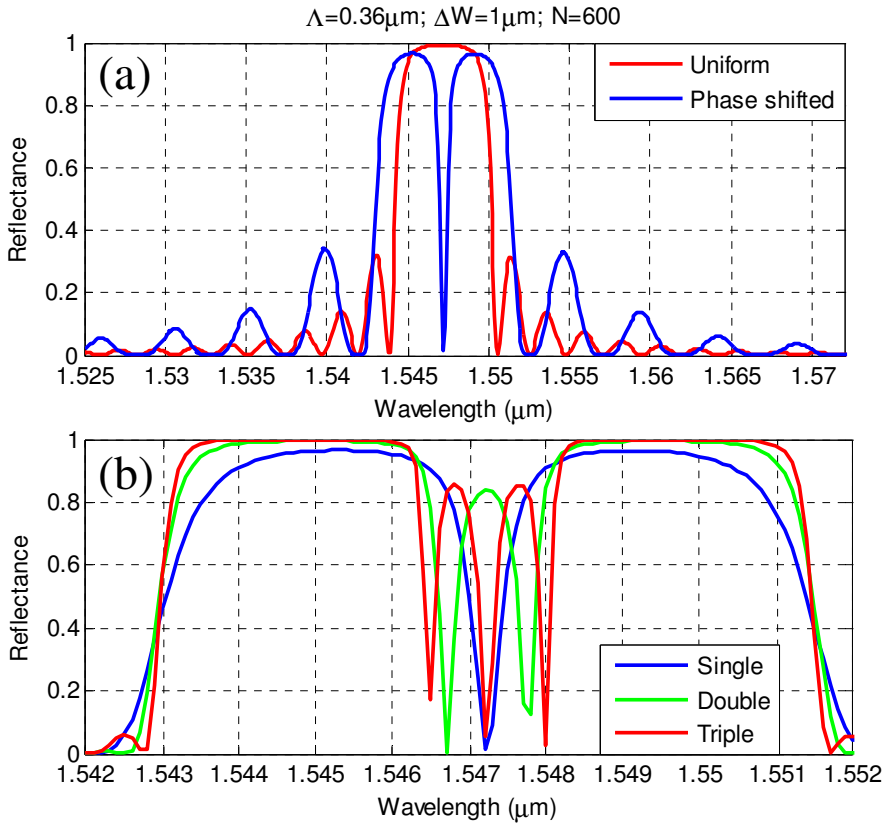

Fig. 4.19. (a) Single and (b) multiple phase-shifted sidewall gratings.

Besides, multi-channel transmission filters can be implemented by introducing multiple phase-shifting spacers in uniform sidewall gratings, [38, 98]. For instance, Fig. 4.11 also displays the reflectance spectra from sidewall gratings with single, double and triple phase-shifting spacers, where each grating section has $N/2 = 300$ periods and each phase shifting spacer has the quarter-wavelength length. Add/drop filters for wavelength-division-multiplexing (WDM) in optical communication systems can be implemented with such phase shifted sidewall gratings [38, 94].

Similar to the phase-shifted sidewall gratings, an optical resonant cavity with the length of L_c can be constructed by two identical DBRs. This optical resonant cavity can be treated as a Fabry-Perot resonator with an effective cavity length L_{eff} [99]. The reflectance spectra for three optical resonant cavities with length L_c = 0.3 mm, L_c = 0.5 mm and L_c = 0.7 mm are given in Fig. 4.20. The free spectral range (FSR) is inversely proportional to the effective cavity length and is determined by Eq. (4.9). For the cavity with L_c = 0.5 mm, the resonant transmission bandwidth is 0.04 nm at 1.5496 μm and thus the Q-factor is ~3.874×10^4. The FSR is 0.9 nm (~112 GHz). The effective cavity length is estimated at L_{eff} = 0.62 mm which is larger than its physical length. The FSR and Q-factor for the L_c = 0.7 mm cavity are 0.63 nm and 9.68×10^4, respective. It is expected that resonant cavities with a Q-factor over 10^6 can be realized with the physical cavity length longer than 1cm. Therefore, such sidewall Bragg gratings are very useful for compact resonant cavities with ultrahigh Q-factors at both near-IR and mid-IR.

$$FSR = \frac{\lambda^2}{2n_{eff}L_{eff}} \tag{4.9}$$

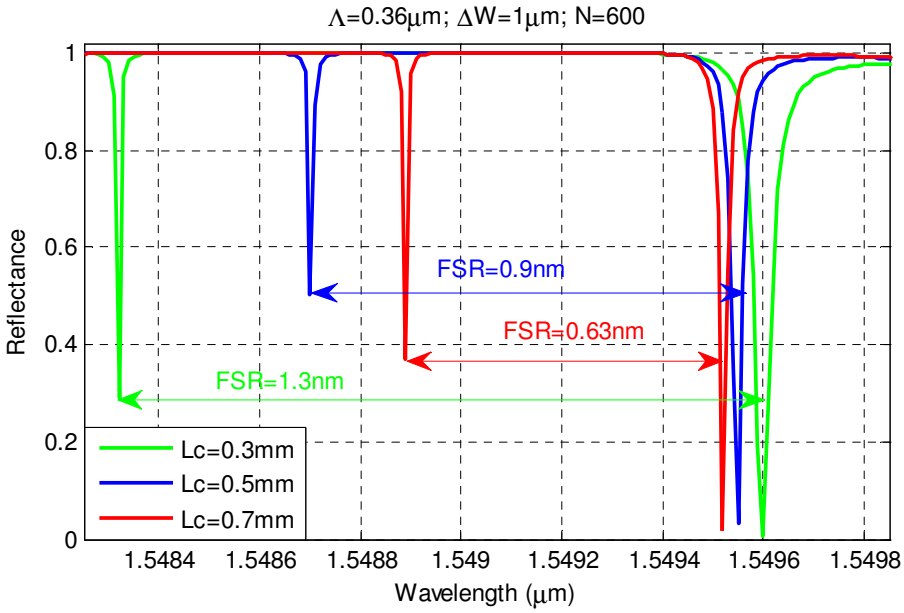

Fig. 4.20. Resonant cavities based on sidewall gratings.

Electro-optic (EO) tunable Bragg gratings on Ti-diffused $LiNbO_3$ waveguide was reported with a tuning rate of 5 pm/V [99]. Here we investigated EO tenability of sidewall gratings on hybrid waveguides, where optical mode is partially confined in As_2S_3 strip (~38% at 1.55 μm for W_0 = 3 μm and t = 280 nm) and the rest of mode is confined in Ti:$LiNbO_3$ channel waveguide. This hybrid mode feature facilitates EO-tuning capabilities. On a x-cut y-propagation $LiNbO_3$ substrate, the optical electric field along the z-axis will experience largest EO effect due to its highest EO coefficient r_{33} = 30.8×10^{-12} m/V. As illustrated in Fig. 4.21, if parallel electrode gap is d, the electric field from external applied voltage V_a along z-axis is given by

$$E_z = \frac{V_a}{d} \tag{4.10}$$

The corresponding refractive index change along z-axis (i.e., extraordinary refractive index) is determined by

$$\Delta n_e = -\frac{1}{2} n_e^3 r_{33} E_z \,. \tag{4.11}$$

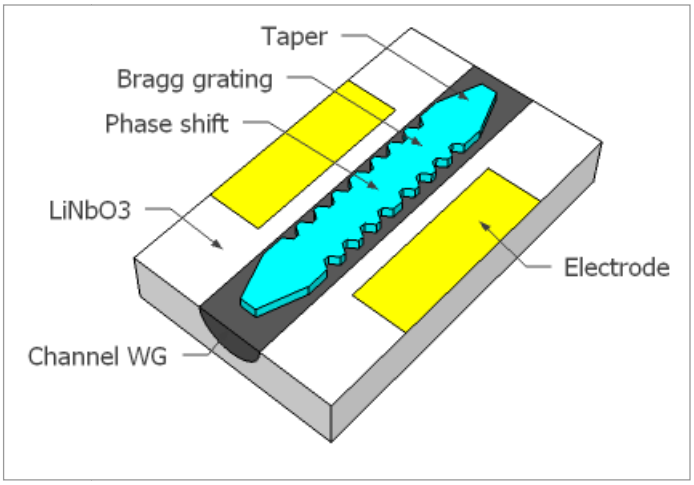

Fig. 4.21. Illustration of EO-tunable phase-shifted gratings.

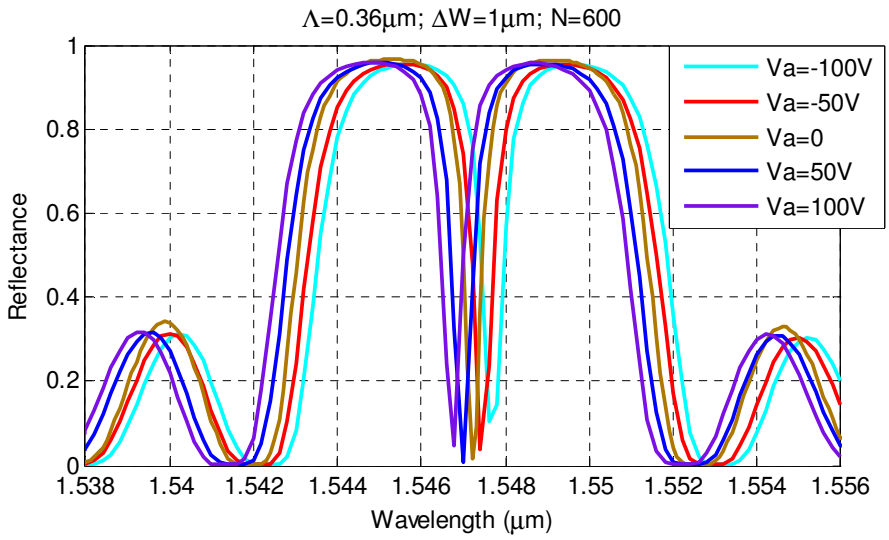

Fig. 4.22. EO-tunable phase-shifted sidewall gratings.

Assume d = 10 μm, V_a = 50 V, then Δn_e = -8.199×10^{-4}. The reflectance of phase-shifted sidewall grating biased at different voltages is plotted in Fig. 4.22. The theoretically-predicted EO tuning efficiency is about 4 pm/V.

4.2.2 Experimental measurements

A commercial optical vector analyzer (from LUNA technologies) was employed to measure spectral reflectance and transmittance of our fabricated sidewall gratings, as shown in Fig. 4.23. The LUNA has a tunable laser that covers a wavelength range from 1525 nm to 1610 nm. After proper calibration, the input light signal from the tunable laser went through paddle polarization controllers before butt-coupled to the device under test (DUT). The output light signal was collected by the imbedded detector in LUNA. Index-matching gel was applied at both end faces of the DUT to minimize fiber-coupling loss. The insertion losses of fiber-to-fiber, 45 degree polarization, and 0 degree polarization are firstly measured and saved as reference data files. The measured raw data on the sidewall gratings was processed by Jones Matrix extraction algorithm [100].

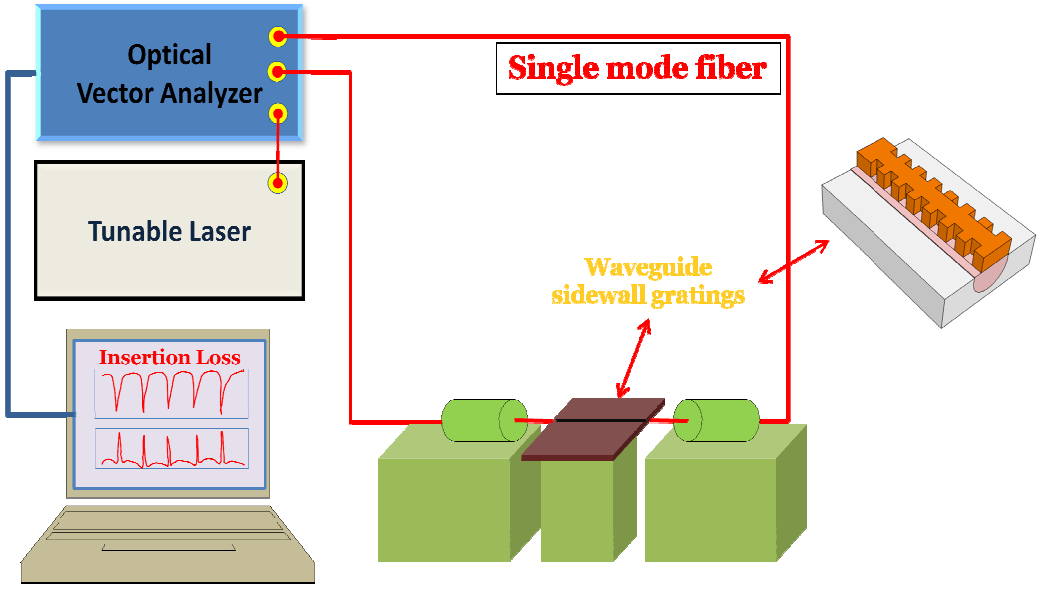

Fig. 4.23. Experimental measurement setup with optical vector analyzer.

The measured reflectance spectrum from fabricated sidewall gratings with different grating depths and grating lengths are plotted in Fig. 4.24 and Fig. 4.25. All these gratings have consistent Bragg wavelength at λ_B = 1547.5 ± 0.3 nm. For the gratings with the same length of L_g = 432 μm shown in Fig. 4.24, the reflectance bandwidth $\Delta\lambda$ increases with grating depth ΔW. However, $\Delta\lambda$ decreases with grating length L for the sidewall gratings with the same value of ΔW as seen in Fig. 4.25. It also shows that the reflectance spectrum possesses Gaussian shape if the product κL_g is much smaller than π. At larger values of κL_g, flattop spectrum is observed as in Fig. 4.24 for ΔW = 800 nm and in Fig. 4.25 for N = 1200. Due to gratings sidewall roughness, measured reflection spectra show asymmetric side-lobes, possibly caused by Fabry-Perot effects from taper end facets. It is also worthy to note, in Fig. 4.24, that larger grating depth leads to a smaller effective index, and Bragg wavelength slightly shifts to a shorter wavelength.

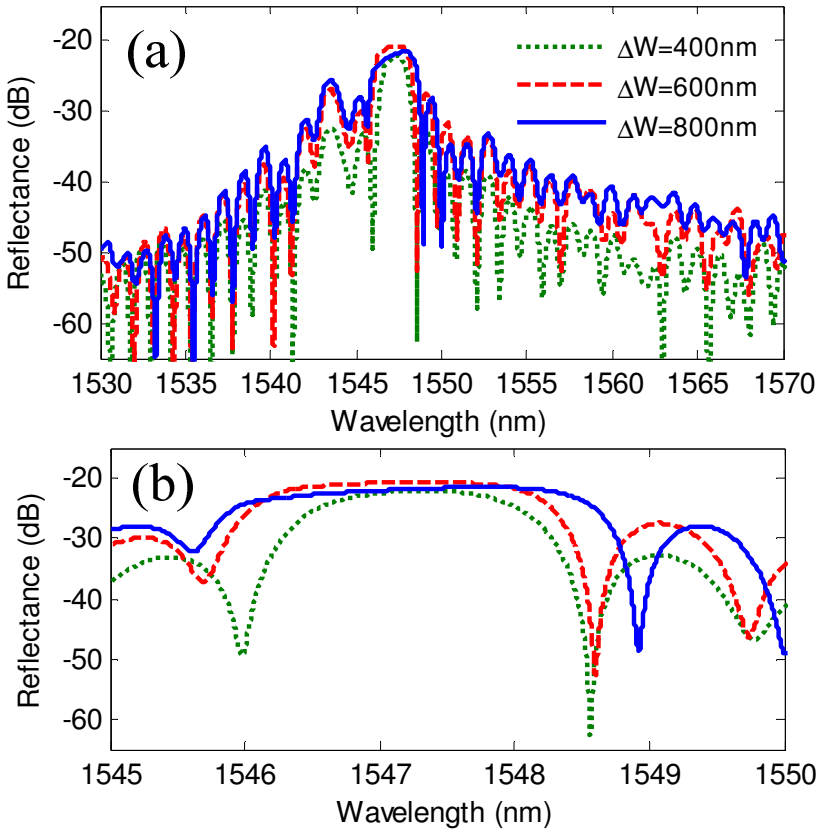

Fig. 4.24. (a) Measured reflectance at N =1200. (b) Zoom-in at 1545-1550 nm.

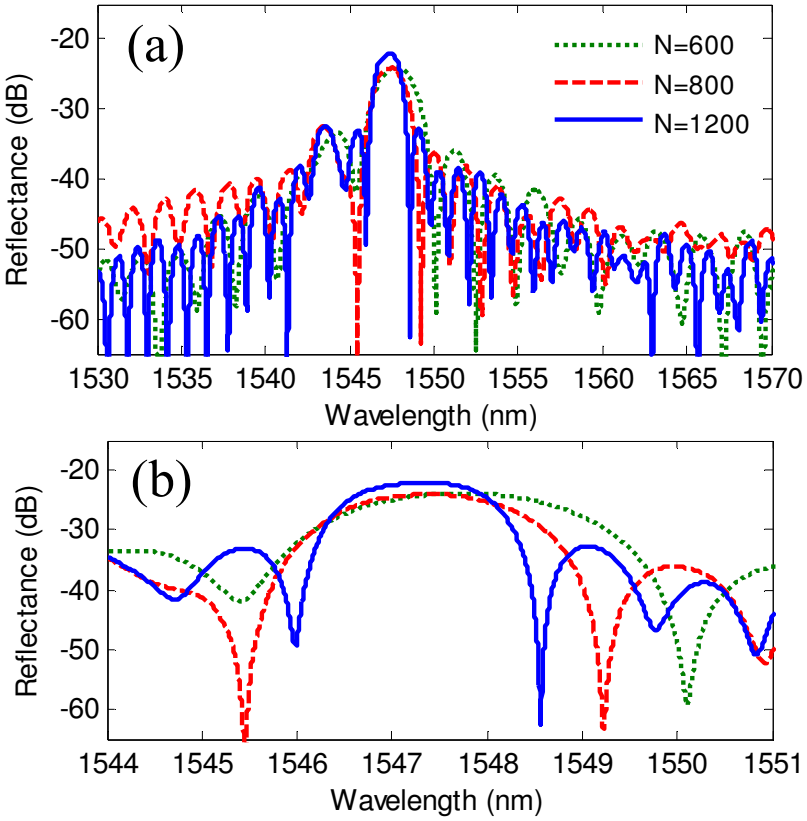

Fig. 4.25. (a) Measured reflectance at ΔW =400 nm. (b) Zoom-in at 1544-1551 nm.

Figure 4.26 plots measured bandwidth ranging from 2.4 nm to 6.7 nm. In general, the reflectance bandwidth drops as the grating length increases. If ΔW < 600 nm, the refractive index perturbation is weak, so the bandwidth is almost invariant by altering grating depth. However, when ΔW is beyond 600 nm, the bandwidth drops as the grating depth increases. These findings are excellently consistent to Eq. (2.58) where $\Delta\lambda$ is inversely proportional to L_g if $\kappa L_g << \pi$, and directly proportional to κ when $\kappa L_g >> \pi$.

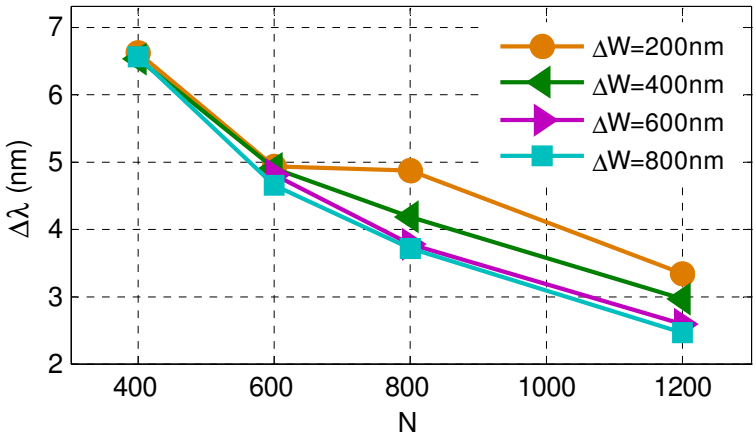

Fig. 4.26. Measured bandwidth of fabricated sidewall gratings.

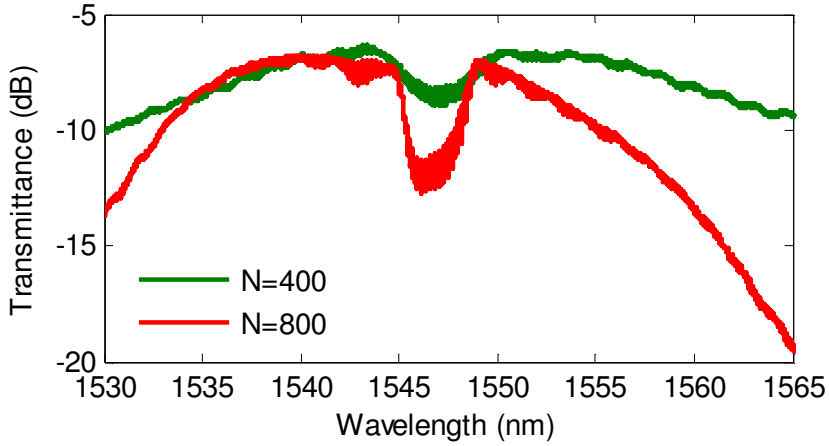

Fig. 4.27. Measured transmittance at ΔW = 800 nm.

Figure 4.28 plots measured spectrum and numerical fitting with 14 dB overall loss. Thus, the scattering loss is (14 - 8.2) = 5.8 dB, very close to the above estimated value. The fitted coupling coefficient is ~4.9 mm^{-1} for the grating in Fig. 4.28. The scattering loss in gratings is ~0.013 dB/μm for N = 1200. Both waveguide loss and scattering loss

can be reduced by smoothing $LiNbO_3$ substrate surface after Ti-diffusion and by post-fabrication trimming on As_2S_3 sidewall gratings.

Measured transmittance spectrum of fabricated sidewall gratings was displayed in Fig. 4.27. It shows an insertion loss (IL) of about 8.2 dB. Generally, the IL loss is contributed by waveguide propagation loss, out-of-plane scattering, mode transitions in tapers, Fresnel reflection at taper tips and fiber-waveguide coupling. Specifically, fiber-waveguide coupling loss is ~0.5 dB/facet [15]. Mode transition loss in the designed two-stage tapers is ~0.8 dB/taper [71]. Fresnel reflection induced loss at taper tip is ~0.3 dB/tip. Since the substrate length is 2 cm, propagation loss for the hybrid waveguide is around 2.5 dB/cm. Note about 22 dB total loss was observed for in-band reflection in Fig. 4.24, the out-of-plane scattering loss in gratings is estimated by (22 - 8.2 × 2) = 5.6 dB. This can be confirmed by numerically-fitting measured spectrum.

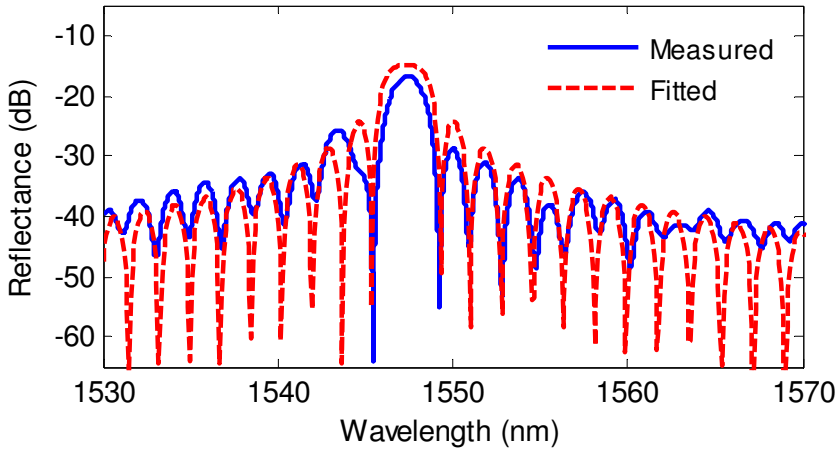

Fig. 4.28. Measured and fitted reflectance at $N = 800$ and $\Delta W = 400$ nm.

Figure 4.29 shows fitted and theoretical coupling coefficients with respect to grating depth. Coupling coefficient ranging from 2.5 mm^{-1} to 8.9 mm^{-1} was achieved. Coupling coefficient is linearly related to grating depth as expected. Fitted coupling coefficients are in good agreement with calculated values based from overlap integration.

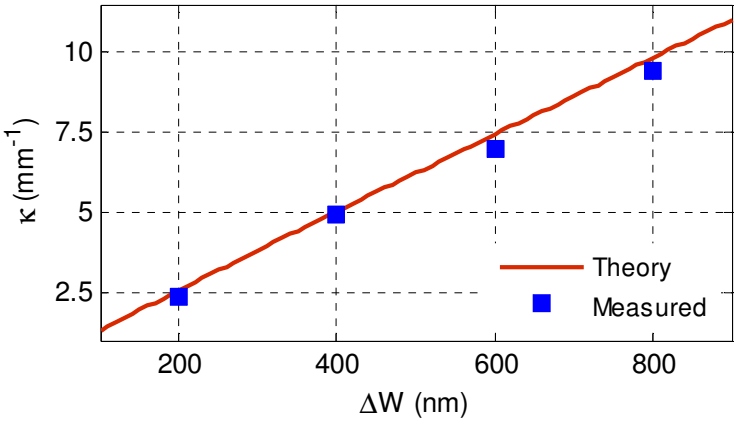

Fig. 4.29. Measured and calculated coupling coefficients.

Phase-shifted sidewall gratings were formed by introducing a quarter-wave spacer in the middle of a uniform grating. A phase-shifted grating can be treated as a microcavity resonator constructed by two distributed Bragg reflectors (DBR) [98]. Fig. 4.30 plots measured spectrum from phase-shifted sidewall gratings with different grating lengths at ΔW = 800 nm. A sharp resonance transmission peak was created near Bragg wavelength (λ_B = 1544 nm for this case). The offset between resonant wavelengths of microcavity resonator and the Bragg wavelength is possibly caused by imperfect fabrication where the spacer is not exactly quarter-wave long. This offset can be eliminated by applying post-fabrication trimming process [101]. The transmission bandwidth gets narrower for

longer gratings. For the phase-shifted grating with N = 1200 (or L_g = 432 μm), the transmission peak linewidth is ~ 0.25 nm, corresponding to a Q-factor of 6200. Resonant micro-cavities with a higher Q-factor can be obtained by using larger values of N and ΔW. High-Q is essential for resonance-based optical sensors to achieve higher sensitivity. By applying multiple quarter-wave spacers in sidewall grating array [102] or by super-positioning sidewall gratings [103], multiple-channel transmission filters that are suitable for wavelength division multiplexing (WDM) can be implemented.

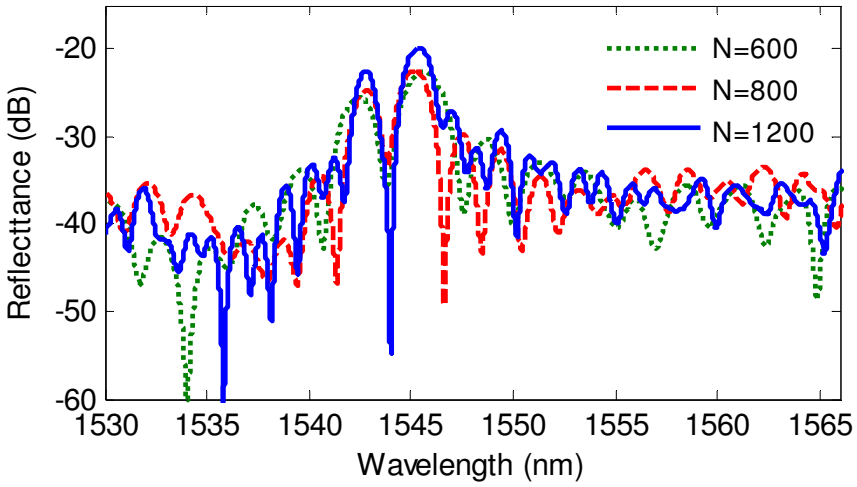

Fig. 4.30. Measured reflectance of phase-shifted gratings at ΔW = 800 nm.

4.2.3 Mid-infrared

Such sidewall gratings can be extended to mid-infrared regime by adjusting the waveguide design. Table 4.2 provides the comparison of waveguide geometries and diffusion conditions for near-infrared wavelength 1.55 μm and mid-infrared wavelength 2.05 μm. Generally, relative larger waveguide geometries and longer diffusion time are

needed for mid-infrared modes due to the larger mode area size and smaller mode effective index compared to near-infrared modes, as shown in Fig. 4.31.

Table. 4.2. Simulation Parameters for Titanium-diffused Waveguides.

λ (μm)	*Thickness* (*nm*)	*Width* (μm)	*Diffusion* (*hour*)	D_h (μm)	D_v (μm)	Δn_x	Δn_y	Δn_z
2.05	135	11	13.5	6.4030	5.3133	0.0240	0.0090	0.0090
1.55	95	7	9.5	5.3713	4.4571	0.0154	0.0072	0.0072

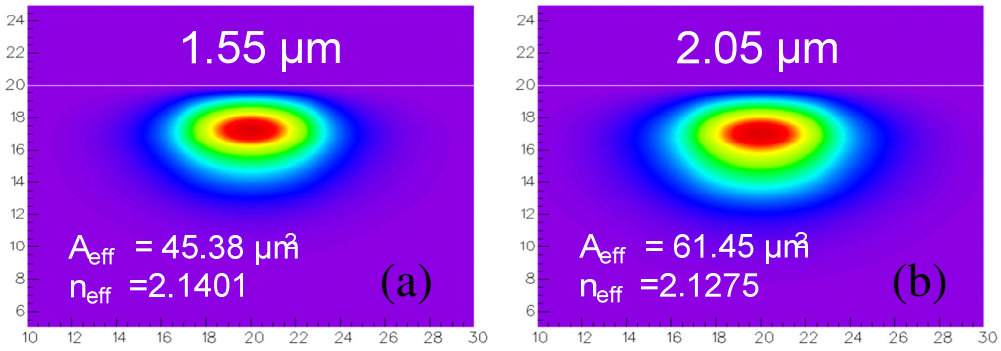

Fig. 4.31. Intensity mode profile at (a) 1.55 µm and (b) 2.05 µm.

An experimental measurement setup is built for the spectral measurement of mid-infrared sidewall gratings, as sketched in Fig. 4.32. The supercontinuum broadband laser source, supplied by NKT Photonics, has a total power of 100 mW and covers a wavelength range from 440 nm to 2.4 µm. The light beam is reflected by three high-reflection mirrors and then focused by a ZnSe lens to a single-mode fiber (SMF). Then, the light is butt-coupled into the device by precise alignment of fiber tips to waveguide end facets under a microscope. Index gel is applied to fiber waveguide gap to minimize

Fresnel reflection loss. A broadband optical spectrum analyzer (OSA) with a resolution of 7.5 GHz (i.e., 105 pm at 2.05 μm), supplied by Thorlabs, is used to monitor the transmission spectrum at output.

We have successfully measured the insertion loss of mid-infrared titanium diffused waveguide. As shown in Fig. 4.33, near 2.05 μm, the background noise floor is about -80 dBm. Fiber to fiber loss is -48 dBm and waveguide device loss is about -47 dBm. Therefore, the insertion loss of the Ti-diffused waveguide is about 1 dB.

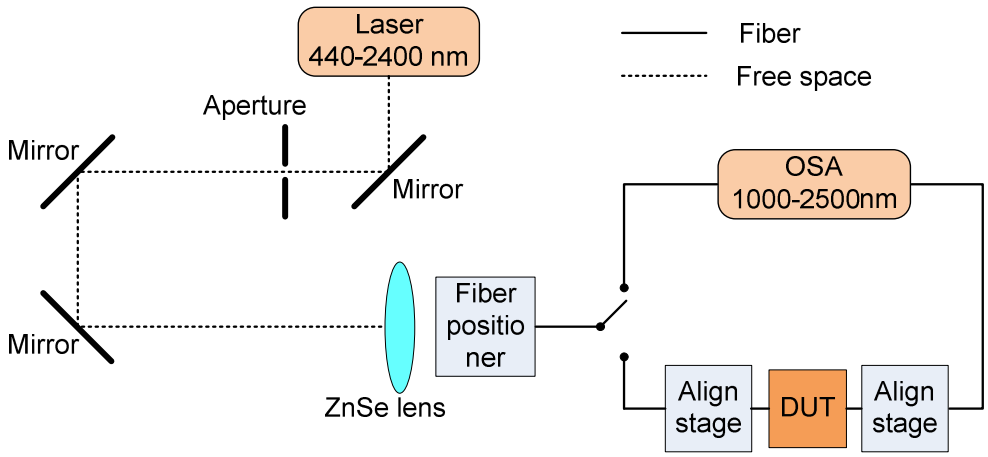

Fig. 4.32. Experimental measurement setup at mid-infrared.

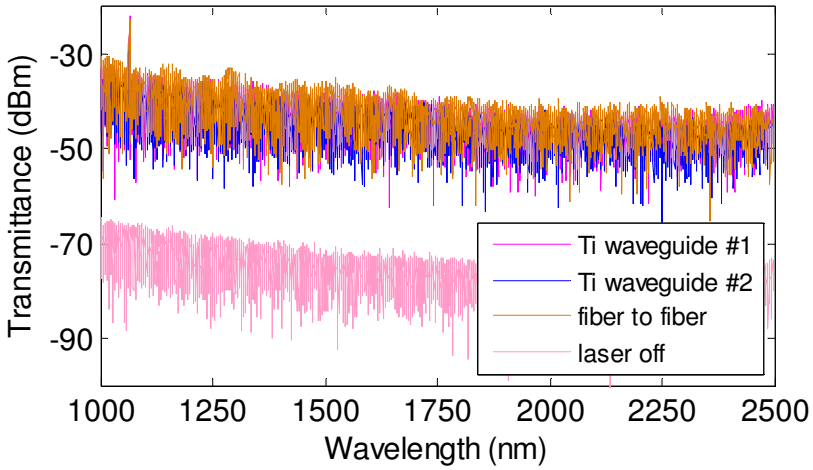

Fig. 4.33. Measured transmittance of mid-infrared Ti waveguide.

Following similar fabrication process as near-infrared gratings, mid-infrared sidewall gratings with a period at 480 nm and unperturbed width of 4.8 μm were also fabricated. Fig. 4.34 shows one of the fabricated mid-infrared sidewall gratings that are well aligned down the midline of Ti-diffused $LiNbO_3$ waveguide.

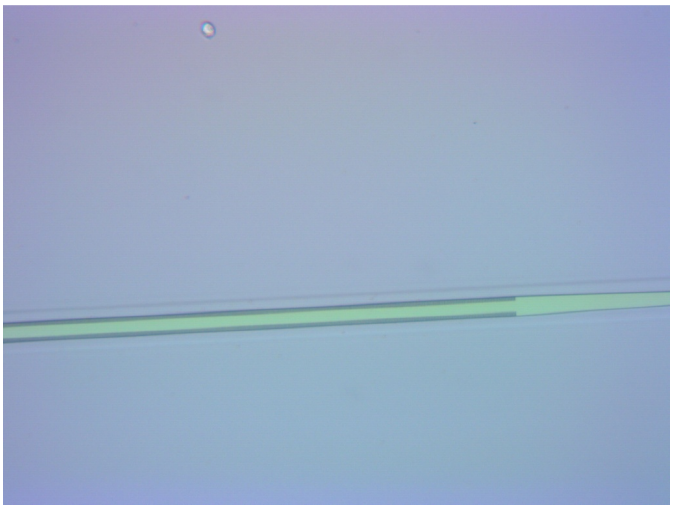

Fig. 4.34. Fabricated mid-infrared As_2S_3 sidewall gratings on Ti:$LiNbO_3$.

4.3 Sidewall Gratings in SOI Slot Waveguide

In this section, two highly sensitive compact refractive index sensors are designed based on sidewall gratings in silicon-on-insulator (SOI) slot waveguide: one resonance-shift sensor detecting the shift of resonance peak wavelength and one intensity-measurement sensor that detects the variation of light intensity at a fixed wavelength. The resonance-shift sensor is based on a single phase-shifted sidewall Bragg gratings with a high *Q*-factor. Coupled phase-shifted sidewall Bragg gratings with the spectral response of a sharp Gaussian shape is adopted by the intensity-measurement sensor. Both refractive index sensors have a minimum detection limit on the order of 10^{-6}, a linear response and a compact structure dimension as small as 11.7 μm. The resonance-shift sensor has a much wider detection range of 1.32 RIU (refractive index unit) than the intensity-measurement sensor. However, the intensity-measurement sensor has relaxed requirements for photodetector resolution and spectrum measurement. The performance parameters of designed sensors are also compared with other integrated refractive index sensors.

4.3.1 Sidewall grating in slot waveguide

In the design, a slot waveguide is formed by placing two silicon strips in parallel with a nanometer gap. Bragg gratings are patterned at the inner sidewalls of the silicon slot waveguide. Sidewall gratings in slot waveguide exhibit several advantages over surface gratings and sidewall gratings in strip or rib waveguide. Firstly, a grating in slot waveguide periodically perturbs the refractive index distribution of the guiding core

(low-index slot region) where the intensity of electric field is much higher than that in high-index region, yielding a strong coupling strength. As a result, its spectral response is extremely sensitive to the change of refractive index of the material inside the slot [52, 60]. It follows that the resonance spectrum changes almost linearly with the refractive index of slot medium. Secondly, a high *Q*-factor resonance cavity can be built using such sidewall gratings with only a few grating periods, making the device dimension very compact. Thirdly, transmission loss arising from out-of-plane scattering and mode mismatch can be reduced when the slot is filled with an analyte material. This helps to sustain a high *Q*-factor and thus high sensitivity. Additionally, such slot waveguide sidewall gratings can be readily fabricated in a few steps by standard microelectronics technologies.

In the calculation, the geometric and physical parameters of sidewall Bragg gratings in slot waveguide are firstly analyzed in terms of mode effective index, mode confinement factor and grating coupling coefficient. The mode effective index, confinement factor and electric field distribution are calculated with film mode matching tools. Material dispersions are included by applying Sellmeier equations [104].

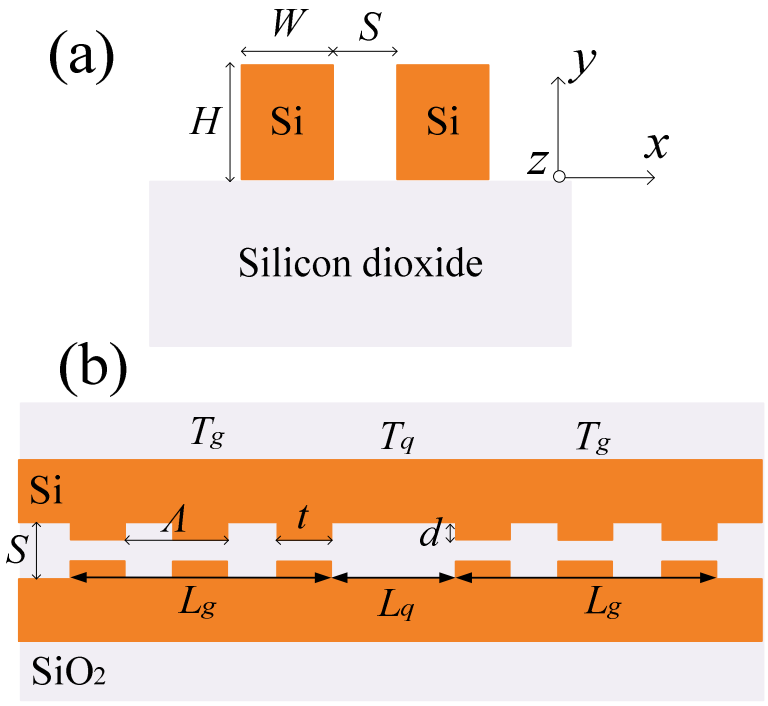

Fig. 4.35. Schematics of (a) slot waveguide and (b) phase-shifted sidewall gratings.

Before the design, the geometric and physical parameters of both slot waveguide and sidewall Bragg gratings need to be optimized to possess performance characteristics desired for optical sensing. Fig. 4.35(a) illustrates the cross-sectional view of a vertical silicon slot waveguide on silicon dioxide. For single mode propagation (TE_0), we designed the slot waveguide formed by two silicon strips with the width W = 300 nm and the height H = 320 nm. The two silicon strips are placed in parallel with an air gap S that has a variable value between 50 nm and 140 nm. We used film mode matching (FMM) tools in Fimmwave to calculate the effective index, confinement factor and transverse electric field distribution of guided modes in slot waveguide. Fig. 4.36 plots the mode effective index n_{eff} as a function of the refractive index of the material loaded in the slot

n_{slot}. The existence of refractive index of the loaded material tends to change the mode effective index in a linear fashion. The change rate is $\Delta n_{eff}/\Delta n_{slot}$ = 0.4055 for the 100 nm-slot waveguide. A larger slot width leads to a smaller effective mode index because the portion of high-index material decreases as the slot width increases. In consideration of strong mode confinement and ease of fabrication, we used S =100 nm in what follows.

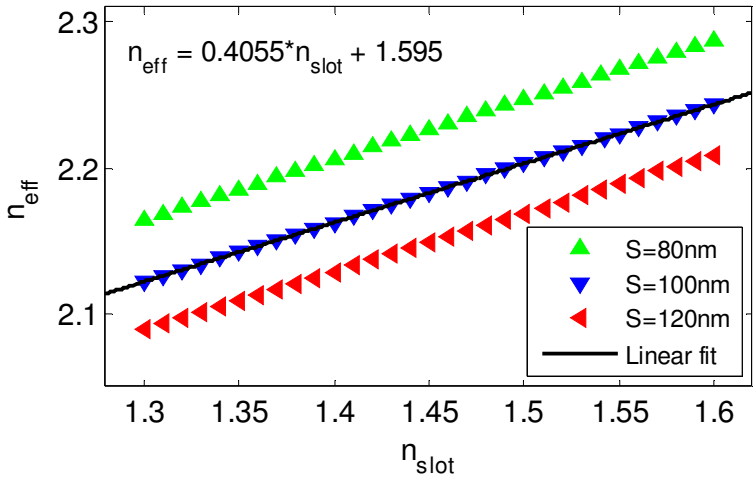

Fig. 4.36. Effective index of slot waveguide filled with different materials.

Figure 4.35(b) is top view of a phase-shifted sidewall Bragg gratings. The gratings are patterned on both inner sidewall interfaces of slot waveguide. The grating parameters are optimized in aspects of strong coupling strength, compact dimension and ease of fabrication. Grating period is determined by phase-matching condition. The phase-shifted sidewall gratings are constructed by introducing a quarter-wave spacer in the middle of the uniform grating so that a resonance microcavity is formed. This quarter-wave spacer will create a cavity resonance near the Bragg wavelength. The length of

quarter-wave spacer is given by $L_q = \lambda_B/(4n_{eff})$. For the 100 nm-slot waveguide loaded with a material with a refractive index 1.45, the corresponding mode effective index is 2.18273 at 1.55 μm. The grating period under phase-matching condition is about 355 nm. We selected Λ = 360 nm for ease of fabrication. The spectral response of a phase-shifted sidewall grating can be analyzed with the transfer matrix method (TMM). The total system transfer matrix is given by $T_{single} = T_g \cdot T_q \cdot T_g$. Complex propagation constant of guided mode is used to consider waveguide loss.

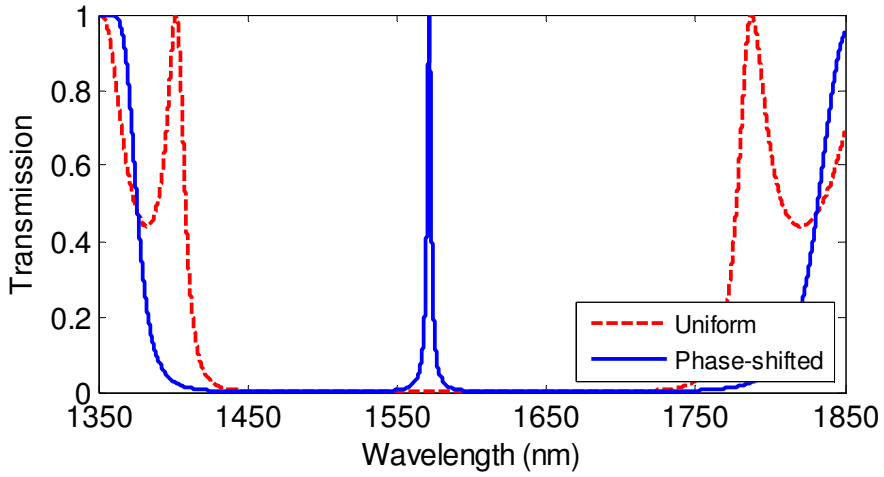

Fig. 4.37. Transmission spectrum for uniform and phase-shifted sidewall gratings.

Figure 4.37 plots superimposed transmission spectrum of a uniform sidewall grating and a phase-shifted sidewall grating in slot waveguide with N = 8 and ΔW = 30 nm. A stopband of ~385 nm centered near the Bragg wavelength λ_B = 1571.35 nm is observed from the uniform sidewall grating. This broad rejection band suggests a wide detection range for an optical sensor. In the transmission spectrum of the phase-shifted sidewall

grating, a sharp resonance peak of a Lorentzian shape with the -3dB bandwidth of ~3.1 nm is observed near Bragg wavelength. Its high transmission, narrow bandwidth and thus high *Q*-factor are key characteristics desired for an optical sensor detecting the resonance wavelength shift.

$$\Gamma = \frac{\varepsilon_0 c}{4} \frac{\iint_{slot} n(x,y) E^2(x,y) dxdy}{\iint_{\infty} P_z(x,y) dxdy} \tag{4.12}$$

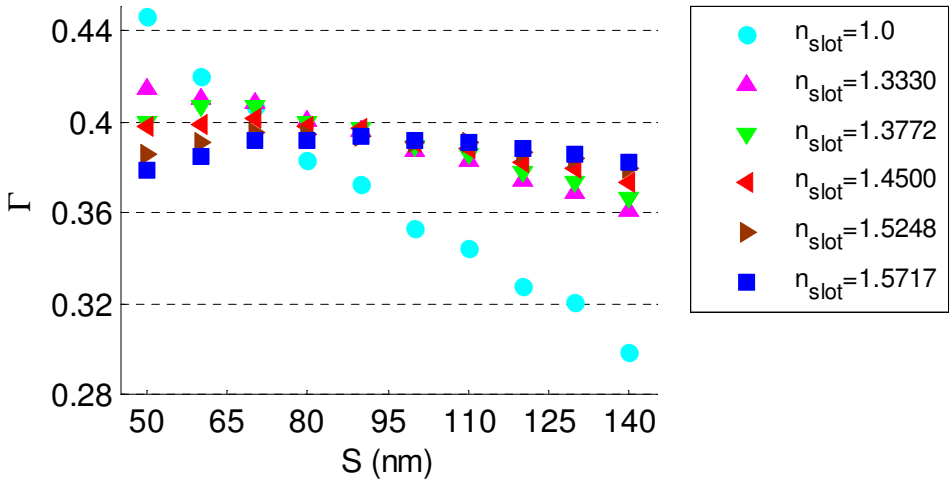

Fig. 4.38. Confinement factor of slot waveguide filled with different materials.

To sustain high transmission and thus high *Q*-factor, high-index contrast material platforms such as silicon-on-insulator (SOI) are often employed to achieve strong mode confinement. In Eq. (4.12), we defined mode confinement factor to measure how much of mode intensity is strongly confined in slot waveguide. Here, $\boldsymbol{P}_z(x, y)$ is Poynting vector and $\boldsymbol{E}(x, y)$ is transverse electric field. Fig. 4.38 plots mode confinement factor as

a function of slot width when the slot waveguide is filled with different materials. As the slot width increases, the confinement factor decreases if the loaded material has an index of refraction smaller than that of water (1.3330). For a 100 nm-slot waveguide, the confinement factor has an optimal value of (39±3)% for a diverse variety of materials including isopropyl alcohol (1.3772), index gel (1.45), chlorobenzene (1.5248) and 1, 2, 4-Dichlorobenzene (1.5717). This feature is much desired for multi-analyte sensing applications.

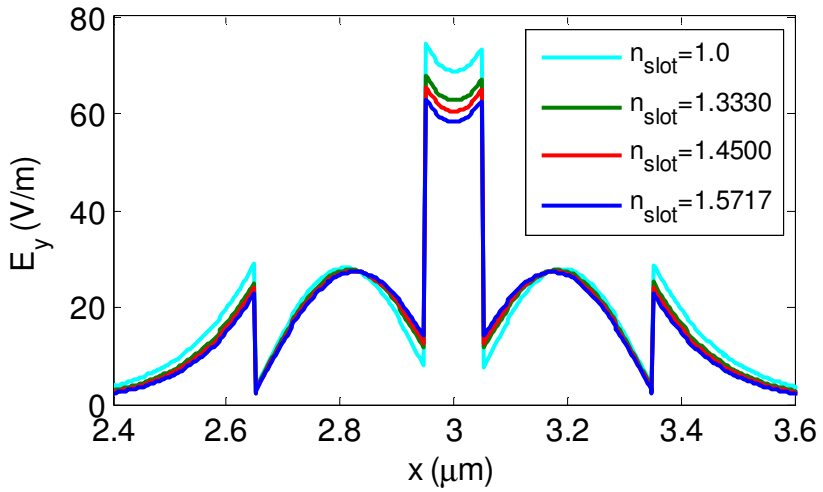

Fig. 4.39. Electric field profile of slot waveguide filled with different materials.

Unlike a surface grating or a sidewall grating in strip waveguide, a sidewall grating in slot waveguide introduces periodic perturbation directly to the guiding core other than the cladding, which leads to a stronger coupling strength. That is because the intensity of transverse electric field confined in the slot region is much higher than that in silicon

strip as seen in Fig. 4.39. Indeed, the ratio between the amplitudes of electric field confined in the slot region and that in strip region is directly proportional to the square of index contrast, so high-index material like silicon is commonly used in slot waveguide. Due to strong coupling strength, the spectral response of such sidewall gratings is extremely sensitive to the change of refractive index of the material in the slot.

To quantitatively evaluate the coupling strength, we calculated coupling coefficient by overlap integration between the distributions of electric field and refractive index over the grating regions as described by Eq. (4.13), where $\omega = 2\pi c/\lambda$ is angular frequency and ε_h is dielectric constant of high-index material. As expected, high index-contrast materials provide larger coupling coefficients. The effects of grating depth and refractive index of slot material on coupling coefficient at 1.55 μm are plotted in Fig. 4.40. The coupling coefficient increases with the increasing grating depth. Loading material in the slot will reduce coupling coefficient as it degrades the index contrast. At d = 30 nm, the change of coupling coefficient per RIU is 0.7510 μm^{-1}. However, in the following section, it will be shown that loading the slot waveguide aids to reduce transmission loss arising from out-of-plane scattering and mode mismatch.

$$\kappa = \frac{4\omega(\varepsilon_h - \varepsilon_0)}{\pi} \sin(\frac{\pi t}{\Lambda}) \sin(\frac{2\pi}{\Lambda}) \iint_{grating} |E(x, y)|^2 \, dxdy \tag{4.13}$$

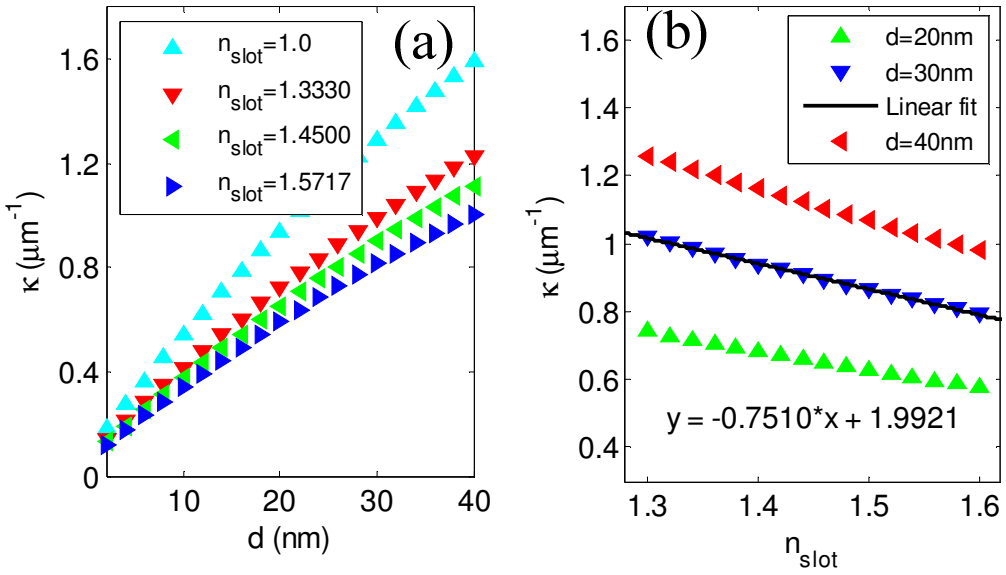

Fig. 4.40. Coupling coefficients of sidewall gratings in slot waveguide.

4.3.2 Resonance-shift sensor

By tailoring spectral response of the sidewall Bragg gratings in slot waveguide, we designed two highly sensitive compact optical refractive index sensors: one resonance-shift sensor and one intensity-measurement sensor. A spectral response with a high transmission and a narrow bandwidth is desired by a resonance-shift sensor as it detects the resonance wavelength shift. The intensity-measurement sensor measures the intensity of transmitted light at a reference wavelength, so it requires a spectral response with a sharp line shape to improve its accuracy and sensitivity.

For a phase-shifted grating, the transmission is highly limited by the loss inside the microcavity resonator formed by two uniform gratings on both sides of the quarter-wave spacer. The *Q*-factor is determined by two types of loss mechanisms: waveguide loss and coupling loss [48, 105]. The coupling loss depends on the product of grating length

and coupling coefficients and can be optimized by adjusting grating depth, duty cycle and grating length [48]. On contrast, the waveguide loss is inherent in the fabrication (sidewall roughness). As a result, the intrinsic Q-factor of a phase-shifted sidewall grating is dominated by waveguide loss that can be attributed by out-of-plane scattering during reflections or by mode mismatch at grating-waveguide interfaces. However, when the slot waveguide is filled with a material, the scattering loss will be reduced as a result of reduced index contrast. On the other hand, filling a slot waveguide also increases its mode effective index, which helps mode transition at grating-waveguide interface. Therefore, the phase-shifted sidewall grating in slot waveguide filled with an analyte material can provide a spectral response with a high transmission and high Q-factor. In general, slot waveguide exhibits a relatively higher loss than conventional silicon strip or rib waveguide. A typical value 10 dB/cm for Si slot waveguide has been reported [59, 106]. Taking account of such losses, we used α = 10 dB/cm in simulations.

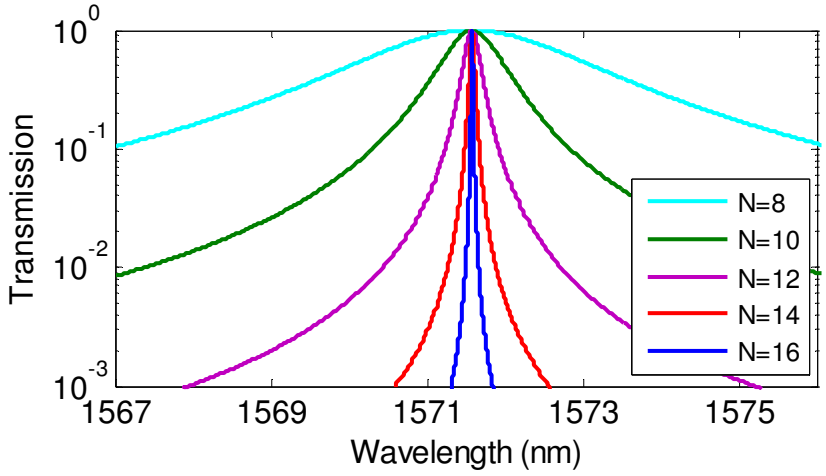

Fig. 4.41. Superimposed transmission spectrum of phase-shifted sidewall gratings.

The resonance-shift sensor is based on a single phase-shifted sidewall Bragg grating in slot waveguide. To precisely detect the shift of resonance wavelength due to a small change in the refractive index of slot material, high transmission and large Q-factor is highly desired [48, 49, 51]. The Q-factor is estimated by $Q = \lambda_B/\Delta\lambda_{fwhm}$ where $\Delta\lambda_{fwhm}$ is the full-width half-maximum (FWHM) bandwidth. The resonance peak wavelength is close to Bragg wavelength due to structure's symmetry. The FWHM bandwidth depends on the product of coupling coefficient and grating length. Since sidewall gratings in slot waveguide have strong coupling coefficients, high Q-factor can be readily achieved by adjusting the grating length and grating depth. Fig. 4.41 displays the superimposed transmission spectrum in dB of single phase-shifted sidewall Bragg gratings with different grating lengths for d = 30 nm. The resonance bandwidth drops quickly as the grating length increases. At N = 16, the bandwidth is suppressed to 20.6 pm, yielding a Q-factor as high as 7.6×10^4. Using the single phase-shifted sidewall grating with N = 16 and d = 30 nm, we designed a resonance-shift sensor.

Figure 4.42(a) shows spectral response of the designed resonance-shift sensor. The refractive index of slot medium varies from 1.35 to 1.55 with an increment of 0.02. As expected, filling the slot waveguide aids to reducing transmission loss by increasing mode effective index. The transmission loss is reduced to 0.06 dB with n_{slot} = 1.55 from 0.47 dB with n_{slot} = 1.35. As the refractive index of slot material increases, the resonance bandwidth increases from 11.04 pm at n_{slot} = 1.35 to 41.76 pm at n_{slot} = 1.55 as in Fig. 4.42(b), leading to decreased Q-factor. The decreasing of Q-factor can also be attributed by waveguide loss. For instance, the Q-factor is 9.3×10^4 at n_{slot} = 1.45 without

waveguide loss (i.e., α = 0). However, the Q-factor of this sensor is maintained in the range between 3.83×10^4 and 1.40×10^5, sufficiently high for efficient light-matter interaction.

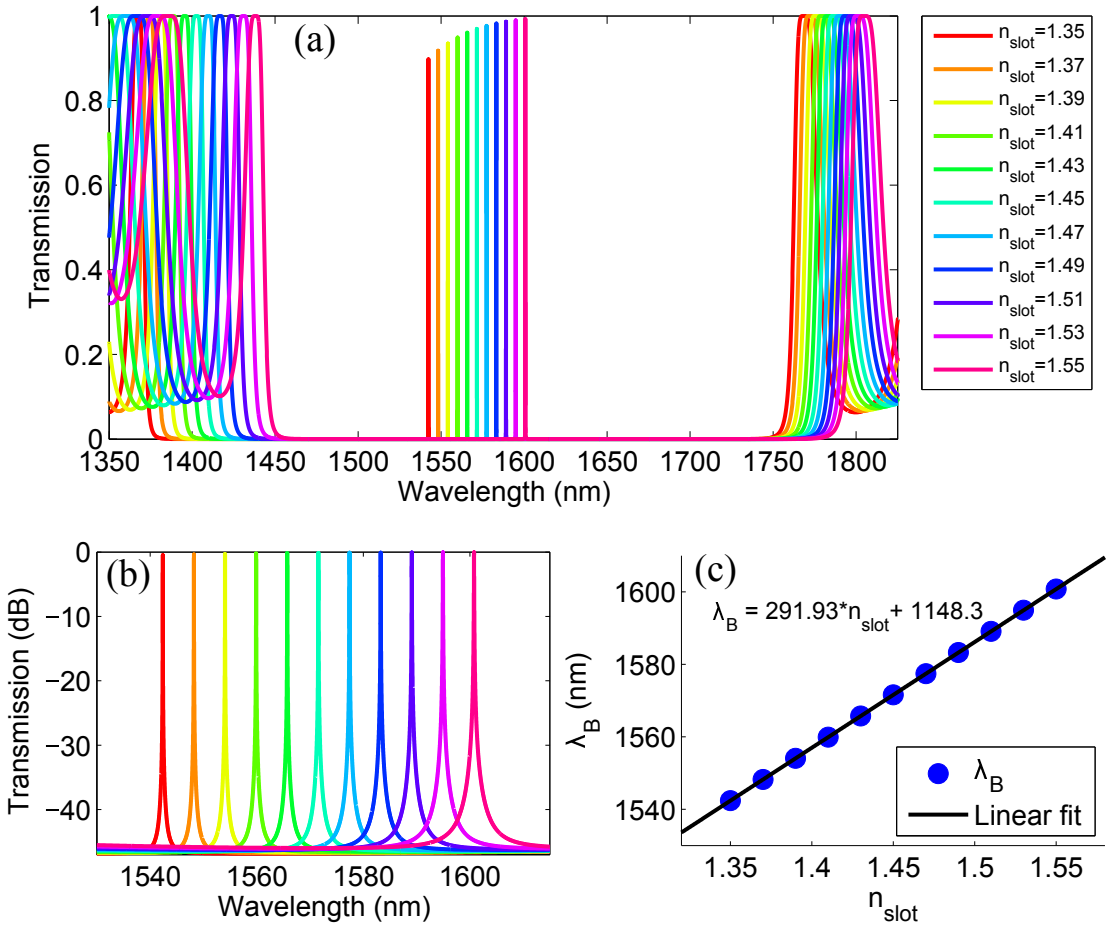

Fig. 4.42. (a) Transmission spectrum and (b) zoom in of transmission peaks for the designed resonance-shift sensor. (c) The resonance peak λ_B as a function of n_{slot}.

In Fig. 4.42(c), a linear response with the slope of $\Delta\lambda_B/\Delta n_{slot}$ = 291.93 nm/RIU is observed. Considering the fact that the smallest shift that can be measurable is one

fifteenth of the resonance peak bandwidth, this sensor has a spectral resolution at $\Delta\lambda_{min}$ = 1.3733 pm. According to Eq. (4.14), the minimum detectable refractive index change is $\Delta n_{min} = 4.7\times10^{-6}$ RIU, which is improved by one order compared with the SOI refractive index sensor in [48]. In addition, the resonance-shift sensor has a compact device dimension of only 11.7 μm.

$$\Delta n_{\min} = \frac{1}{2\Lambda}\left(\frac{\Delta n_{slot}}{\Delta n_{eff}}\right)\Delta\lambda_{\min} \tag{4.14}$$

The detection range of this refractive index sensor is wide because the resonance wavelength can shift over a broad wavelength band from 1404 nm to 1789 nm. This range suggests a possible detection range of approximately 1.32 RIU. To further extend the detection range, sensor array can be implemented by deploying multiple phase-shifted sidewall gratings side by side with successive values of grating periods (Λ_1, Λ_2, ⋯, Λ_n) on a same chip.

4.3.3 Intensity-measurement sensor

The intensity-measurement sensor detects the intensity variation of transmitted light at a fixed wavelength, so the sharpness of transmission spectrum is critical in improving the sensitivity and accuracy. We used coupled microcavity configuration to optimize the desired spectrum sharpness.

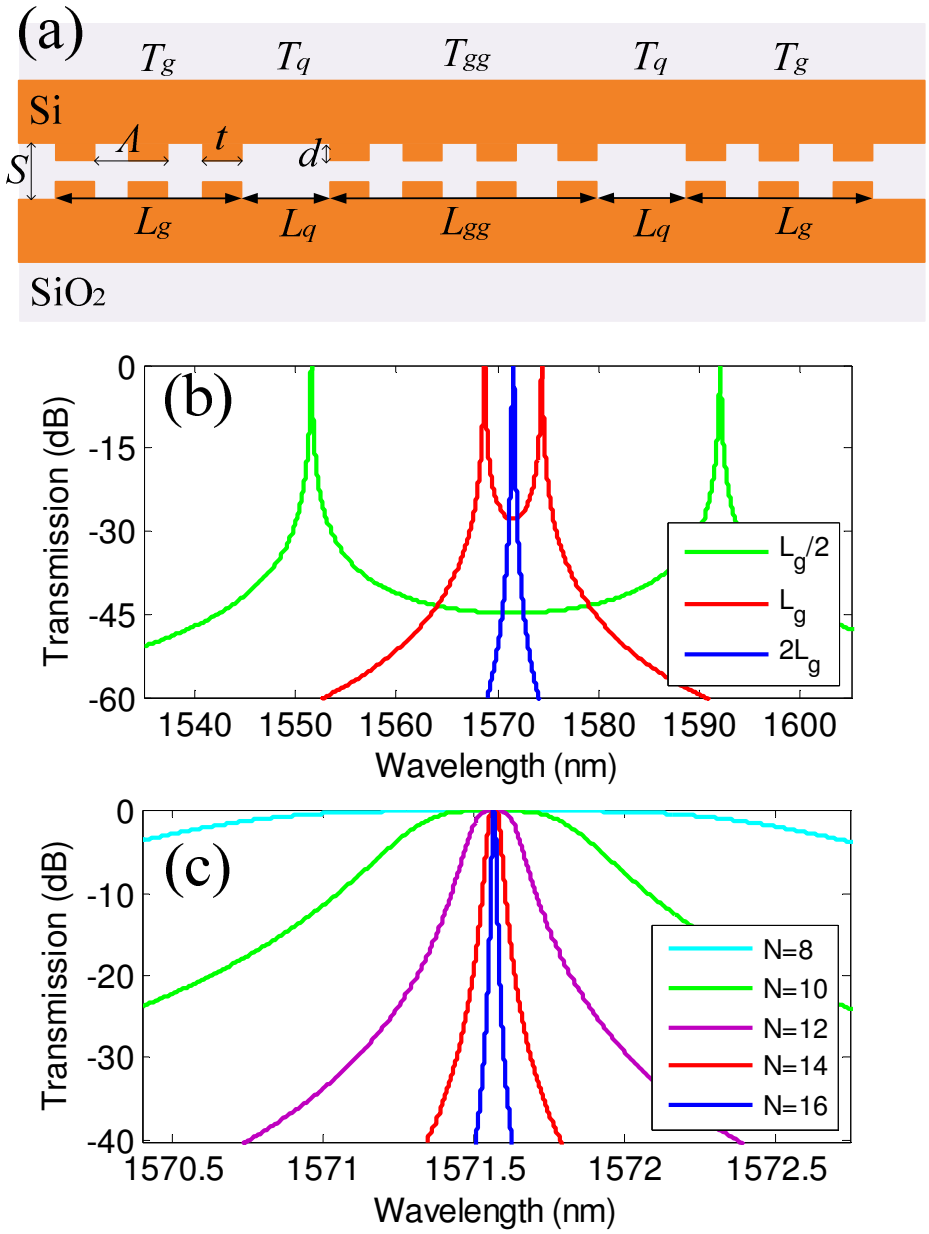

Fig. 4.43. (a) Coupled phase-shifted sidewall gratings and their transmission spectrum for (b) different L_{gg} with N = 12 and (c) different N with L_{gg} =2·L_g.

As illustrated in Fig. 4.43(a), coupled phase-shifted sidewall Bragg gratings in slot waveguide is realized by inserting two quarter-wave spacers in a uniform grating. L_{gg}

and L_g indicate the length of inner grating and outer gratings, respectively. The outer grating length is given by $L_g = N \cdot \Lambda$. Following the TMM method, the total transfer matrix of such a coupled grating structure is given by $T_{coupled} = T_g T_q T_{gg} T_q T_g$. Since $L_{gg} = 2 \cdot L_g$, we can estimate that $T_{coupled} = (Tg \cdot T_q \cdot T_g) \cdot (T_g \cdot T_q \cdot T_g) = (T_{single})^2$ by splitting the inner grating segment into halves with each having a length of L_g. Analogous to the fact that the function $f(x) = -x^4$ has sharper edge and flatter top than the function $f(x) = -x^2$ where x is a real number, coupled phase-shifted sidewall gratings exhibit better spectrum sharpness.

Figure 4.43(b) plots superimposed transmission spectrum of coupled phase-shifted Bragg gratings with different values of L_{gg}. As the length of inner grating gets close to $2 \cdot L_g$, the two resonance transmission peaks tends to emerge and form a flat-top, narrow and sharp Gaussian shape. Compared with the Lorentzian shape from a single phase-shifted Bragg grating, the flat-top feature is undesirable for an optical sensor that detects the wavelength shift, but the sharpness of Gaussian shape is favored by an intensity-measurement sensor, because it provides a large change in the light intensity if there is a small change in the refractive index of slot material. To quantitatively evaluate the sharpness, we defined the spectrum selectivity as $SS = \Delta\lambda_{-1dB} / \Delta\lambda_{-10dB}$ where $\Delta\lambda_{-1dB}$ and $\Delta\lambda_{-10dB}$ denote the -1dB bandwidth and -10dB bandwidth, respectively. The spectrum selectivity of the coupled phase-shifted sidewall Bragg gratings is 2.42 times larger than that of a single phase-shifted Bragg grating for $N = 12$.

Figure 4.43(c) shows the transmission spectrum of the coupled phase-shifted gratings with $L_{gg} = 2 \cdot L_g$ and different grating lengths. Similar to the single phase-shifted grating,

the transmission bandwidth of coupled phase-shifted gratings also decreases with the grating length. To design an intensity-measurement sensor as compact as the resonance-shift sensor, we choose $N = 12$, making the device structure dimension to be 17.64 μm.

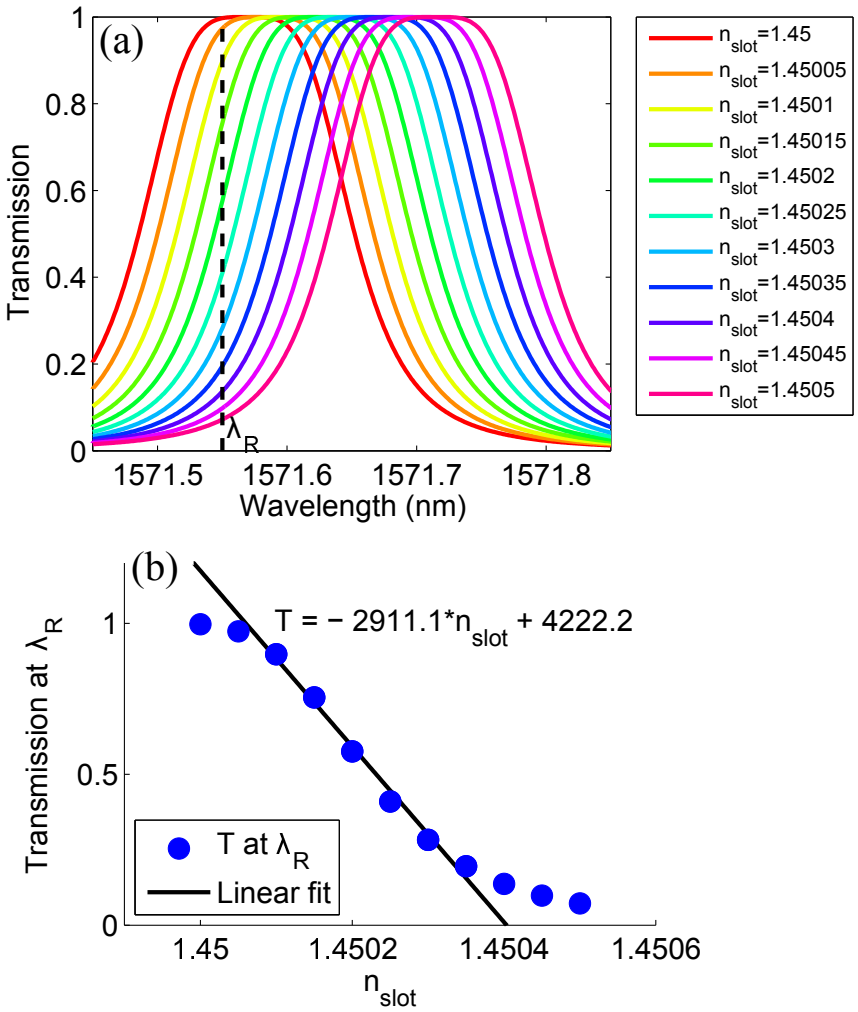

Fig. 4.44. (a) Transmission spectrum of the intensity-measurement sensor. (b) Transmission light intensity at reference wavelength λ_R as a function of n_{slot}.

The intensity-measurement sensor is designed to detect the change of light intensity at the reference wavelength λ_R = 1571.55 nm. Fig. 4.44(a) plots transmission spectrum of this sensor. The refractive index of slot medium varies from 1.45 to 1.4505 with an increment of 0.00005. The light intensity changes almost linearly at a rate of $\Delta P/\Delta n_{slot}$ = 2911.1 RIU^{-1} with the refractive index of slot medium. It is noteworthy that the waveguide loss is negligible for this sensor. Given the power measurement resolution ΔP_{min} that depends on the power fluctuation level of laser source and the dark current noise of photodetector, the detection limit can be calculated. For ΔP_{min} = 1%, the detection limit is $\Delta n_{min} = 3.4\times10^{-6}$ RIU. Because the spectral response of coupled phase-shifted Bragg gratings has a sharp Gaussian shape and the intensity varies fast with the change of refractive index of the slot medium, the detection range of the intensity-measurement sensor is limited to 0.009 RIU. However, the intensity-measurement sensor has relaxed requirements for detector resolution and intensity spectrum since the measurement is based on a single wavelength.

The device performance parameters of some integrated refractive index sensors are compared and summarized in Table 4.3. The proposed refractive index sensor based on a single phase-shifted sidewall Bragg grating in slot waveguide provides the largest *Q*-factor at $Q = 7.6\times10^4$, the highest sensitivity on the order of 10^{-6} and the smallest device dimension at 11.7 μm. Although the SOI Mach-Zehnder interferometer can have the minimum detection limit on the same order, it requires a device dimension as large as 30 mm [39]. The detection limit of the proposed resonance-shift sensor can be further improved by using relatively longer gratings to realize a microcavity resonator with a

larger *Q*-factor. The designed intensity-measurement sensor based on coupled phase-shifted sidewall Bragg gratings also has sensitivity on the order of 10^{-6} and a device structure length of 17.64 μm. Besides, the resonance-shift sensor has a linear response over a wide detection range of 1.32 RIU. The intensity-measurement sensor has a quasi-linear response over a detection range of only 0.009 RIU. For both designed sensors, extended detection range in RIU and simultaneous detection for multiple fluidic analytes are possible by implementing sensor array with successive values of grating periods.

Table. 4.3. Performance Parameters of Some Integrated Refractive Index Sensors.

Refractive index sensor	Δn_{min}	*Device dimension*	*Q-factor*
SOI Mach-Zehnder interferometer [49]	7×10^{-6}	L =30 mm	-
Hydex ring resonator [49]	1.8×10^{-5}	Radius =60 μm	12000
SOI ring resonator [51]	1×10^{-5}	Radius =5 μm (area = 100 μm^2)	20000
Si_3N_4 ring resonator in slot waveguide [63]	2.3×10^{-4}	Radius =70 μm	-
SOI ring resonator in slot waveguide [64]	4.2×10^{-5}	Radius =5 μm (area =130 μm^2)	330
Surface gratings in Si rib waveguide [47]	10^{-4}	L =173 μm	-
SOI nanowire phase-shift gratings [48]	5×10^{-5}	L =13 μm	13265
Proposed phase-shift gratings in slot waveguide	4.7×10^{-6}	L =11.7 μm	76000

CHAPTER V

SUMMARY AND CONCLUSIONS

5.1 Summary

To briefly summarize, by combining arsenic tri-sulfide and lithium niobate, a novel hybrid waveguide platform is introduced. On this platform, optical hybrid waveguide structures are firstly designed and simulated for efficient mid-infrared emission at 4.0-4.9 μm by difference frequency generation via type-I and type-IV phase-matching schemes. The designed waveguide is configured for single-mode operation for all interacting waves to enhance nonlinear process. For type-I waveguides, we predicted a DFG conversion efficiency of 0.11% W^{-1} near 4.745 μm on a 6 mm-long waveguide using 50 mW pump wave at 1.42 μm and 50 mW signal wave at 2.05 μm. The maximum conversion efficiency is 0.23% W^{-1}, limited mainly by waveguide loss. A broad mid-IR tuning range from 3.3 μm to 4.9 μm can be realized by using tunable near-infrared signal/pump lasers. For type-IV phase-matching that utilizes the largest second-order nonlinearity element of $LiNbO_3$ crystal, a normalized power conversion efficiency of 20.52%$W^{-1}cm^{-2}$ was theoretically predicted on a 1 mm-long hybrid waveguide pumped at 50 mW powers, which, to the best of our knowledge, is the highest efficiency record for mid-infrared DFG waveguides based on $LiNbO_3$ crystal. Using a tunable near-infrared pump laser at 1.38-1.47 μm or a tunable signal laser at 1.95-2.15 μm, a broad mid-infrared tuning range from 4.0 μm to 4.9 μm can be achieved. Such hybrid As_2S_3-Ti:$LiNbO_3$ optical waveguides may provide an alternative approach for broad

continuously-tunable mid-infrared emission with mW powers and sub-nanometer linewidths.

Secondly, the design, simulation, fabrication and experimental measurements for integrated sidewall gratings in hybrid arsenic tri-sulfide on titanium diffused lithium niobate optical waveguide are discussed in details. The waveguide sidewall gratings design is guided by the coupled-mode theory and transfer matrix method. Coupling coefficients is calculated by taking overlap integration over the grating region. Reflectance and its bandwidth for weak coupling and strong coupling conditions are analyzed. Such sidewall gratings are fabricated by electron beam lithography and metal liftoff process. Experimental measurements of spectral transmission and reflection of uniform gratings and phase-shifted gratings are in good agreement with the theory. Based on numerical fittings, coupling coefficients between 2.5 mm^{-1} and 8.9 mm^{-1} were abstracted, which were excellently consistent with the values calculated by overlap integration. The waveguide propagation loss was about 2.5 dB/cm and 5.6 dB scattering loss was estimated on sidewall gratings with a length of 432 μm. Both types of loss can be reduced by smoothing Ti-diffused substrate surface and by applying post-fabrication trimming on As_2S_3 gratings. A transmission peak with a 3-dB bandwidth of ~0.25 nm was observed near Bragg wavelength from phase-shifted sidewall gratings. Such integrated sidewall gratings can be applied to a diverse variety of integrated optical devices including optical filters, switches, lasers, modulators, sensors, and wavelength division multiplexing.

Finally, two highly-sensitive compact optical refractive index sensors are designed based on phase-shifted sidewall gratings in silicon-on-insulator slot waveguide. one resonance-shift sensor detecting the shift of resonance peak wavelength and one intensity-measurement sensor that detects the variation of light intensity at a fixed wavelength. The resonance-shift sensor is based on a single phase-shifted sidewall Bragg gratings with a high *Q*-factor. Coupled phase-shifted sidewall Bragg gratings with the spectral response of a sharp Gaussian shape is adopted by the intensity-measurement sensor. Both refractive index sensors have a minimum detection limit on the order of 10^{-6}, a linear response and a compact structure dimension as small as 11.7 μm. The resonance-shift sensor has a much wider detection range of 1.32 RIU (refractive index unit) than the intensity-measurement sensor. However, the intensity-measurement sensor has relaxed requirements for detector resolution and spectrum measurement. The performance parameters of designed sensors are also compared with other integrated refractive index sensors.

5.2 Conclusions

To conclude, the combination of arsenic tri-sulfide and lithium niobate (As_2S_3-Ti:$LiNbO_3$) provides a flexible design platform for numerous integrated optical devices such as optical filters, switches, modulators, polarization converters, sensors and nonlinear wavelength converters. More complex functions can also be realized by integrating both passive and active functional elements on a same chip. The efficient low-loss fiber-waveguide coupling especially enables the on-chip integration of As_2S_3-

$Ti:LiNbO_3$ platform with other electronics, sources and detectors. The side-by-side array integration of sidewall gratings on As_2S_3-$Ti:LiNbO_3$ optical waveguide can be readily implemented without introducing additional fabrication steps. Indeed, sidewall gratings are widely used in distributed feedback lasers (DFB), the most popular semiconductor laser for > 40 Gbps optical communication systems, to obtain narrow spectral linewidth (MHz), low noise, high on-off speed as well as high power levels. Phase-matched difference frequency generation provides an attractive method to generate mid-infrared wavelength because the excellent device performances of well-established near-infrared lasers can be transferred into the mid-infrared output. Such device performances include narrow linewidth, wide tunable range and high power levels, which are of paramount importance for practical mid-infrared applications such as high-resolution spectroscopy, trace gas monitoring and free space communications.

Additionally, integrated optical sensors should have a compact footprint, higher sensitivity, compatible for integration and easy of fabrication. Utilizing the strong electric fields confined in a slot waveguide, smaller device with a higher sensitivity and wider dynamic range can be created. The two designed optical refractive index sensor have sensitivity in the order of 10^{-6} and a footprint as small as 11.7 μm. The detection range is 1.32 RIU and can be further extended by implementing sensor array of sidewall gratings with varying grating periods. In practice, the sensitivity of a resonance-based optical sensor is limited by waveguide loss which is attributed by waveguide sidewall roughness. However, low-loss slot waveguide has been reported as a result of rapid

research and development in nanofabrication technologies. Therefore, it is quite feasible to implement such highly-sensitive compact refractive index sensors.

REFERENCES

[1] G. P. Agrawal, *Fiber-optic Communication Systems,* 2nd edition (John Wiley & Sons, New York, 1997).

[2] B. E. A. Saleh, M. C. Teich, *Fundamentals of Photonics,* 2nd edition (Wiley-Interscience, New York, 2007).

[3] D. L. Lee, *Electromagnetic Principles of Integrated Optics* (John Wiley & Sons, New York, 1986).

[4] T. Tsuchizawa, K. Yamada, H. Fukuda, T. Watanabe, Jun-ichi,Takahashi, M. Takahashi, T. Shoji, E. Tamechika, Sei-ichi Itabashi, and H. Morita, "Microphotonics devices based on silicon microfabrication technology," IEEE J. Sel. Top. Quantum Electron. **11**, 232-240 (2005).

[5] S. Zheng, H. chen, and A. W. Poon, "Microring-resonator cross-connect filters in silicon nitride: rib waveguide dimensions dependence," IEEE J. Sel. Top. Quantum Electron. **12**, 1380-1387 (2006).

[6] H. Inoue, K. Hiruma, K. Ishida, T. Asai, and H. Matsumura, "Low loss GaAs optical waveguides," IEEE Trans. on Electron Devices **ED-32**, 2662-2668 (1985).

[7] T. Han, S. Madden, D. Bulla, and B. Luther-Davies, "Low-loss chalcogenide glass waveguide by thermal nano-imprint lithography," Opt. Express **18**, 19286-19291 (2010).

[8] P. G. Suchoski and R. V. Ramaswamy, "Minimum-mode-size low-loss Ti:$LiNbO_3$ channel waveguides for efficient modulator operation at 1.3 μm", IEEE J. of Quantum Electron. **23**, 1673-1679 (1987).

[9] H. Ma, A. K. Jen, and L. R. Dalton, "Polymer-based optical waveguides: materials, processing, and devices," Adv. Mater. **14**, 1339-1365 (2002).

[10] A. W. Fang, H. Park, R. Jones, O. Cohen, M. J. Paniccia, and J. E. Bowers, "A continuous-wave hybrid AlGaInAs-silicon evanescent laser," IEEE Photon. Technol. Lett. **18**, 1143-1145 (2006).

[11] H. Park, A. W. Fang, O. Cohen, R. Jones, M. J. Paniccia, and J. E. Bowers, "A hybrid AlGaInAs-Silicon evanescent amplifier," IEEE Photon. Technol. Lett. **19**, 230-232 (2007).

[12] H Park, AW Fang, R Jones, O Cohen, O Raday, M. N. Sysak, M. J. Paniccia, and J. E. Bowers, "A hybrid AlGaInAs-silicon evanescent waveguide photodetector," Opt. Express **15**, 6044-6052 (2007).

[13] C. M. Jean-Francois Viens, A. Villeneuve, T. V. Galstian, E. J. Knystautas, M. A. Duguay, K. A. Richardson, and T. Cardinal, "Fabrication and characterization of integrated optical waveguides in sulfide chalcogenide glasses," J. Lightwave Technol. **17**, 1184-1191 (1999).

[14] X. Xia, Q. Chen, C. Tsay, C. B. Arnold, and C. K. Madsen, "Low-loss chalcogenide waveguides on lithium niobate for the mid-infrared," Opt. Lett. **35**, 3228-3230 (2010).

[15] Y. Zhou, X. Xia, W. T. Snider, J. Kim, Q. Chen, W.C. Tan, and C. K. Madsen, "Two-stage taper enhanced ultra-high Q As_2S_3 ring resonator on $LiNbO_3$," IEEE. Photon. Technol. Lett. **23**, 1195-1197 (2011).

[16] Q. Chen, X. Wang, and C. K. Madsen, "Phase-Matching and Parametric Conversion for the Mid-Infrared in As_2S_3 Waveguides," Opt. Photon. J. **2**, 260-264 (2012).

[17] X. Wang, A. Jiang, and C. K. Madsen, "Chalcogenide As_2S_3 sidewall Bragg gratings integrated on $LiNbO_3$ substrate," Opt. Photon. J. **3**, 78-87 (2013).

[18] W. T. Snider, Dwayne D. Macik, and C. K. Madsen, "Electro-optically tunable As_2S_3 Mach-Zehnder interferometer on $LiNbO_3$ substrate," IEEE. Photon. Technol. Lett. **24**, 1415-1417 (2012).

[19] J. Kim, W. J. Sung, O. Eknoyan, and C. K. Madsen, "Linear photonic frequency discriminator on As_2S_3-ring-on-Ti:$LiNbO_3$ hybrid platform," Opt. Express **21**, 24566-24573 (2013).

[20] W. Urban, "Physics and spectroscopic applications of carbon monoxide lasers, a review," Infrared Phys. & Technol. **36**, 465-473 (1995).

[21] M. Tacke, "New developments and applications of tunable IR lead salt lasers," Infrared Phys. & Technol. **36**, 447-463 (1995).

[22] M. Fill, P. Debernardi, F. Felder, and H. Zogg, "Lead-chalcogenide mid-infrared vertical external cavity surface emitting lasers with improved threshold: theory and experiment," Appl. Phys. Lett. **103**, 201120 (2013).

[23] C. Gmachl, F. Capasso, D. L. Sivco, and A. Y. Cho, "Recent progress in quantum cascade lasers and applications," Rep. Prog. Phys. **64**, 1533-1601 (2001).

[24] Y. Yao, X. Wang, Jen-Yu Fan, and C. F. Gmachl, "High performance 'continuum-to-continuum' quantum cascade lasers with a broad gain bandwidth of over 400 cm^{-1}," Appl. Phys. Lett. **97**, 081115 (2010).

[25] M. Kim, C. L. Canedy, W. W. Bewley, C. S. Kim, J. R. Lindle, J. Abell, I. Vurgaftman, and J. R. Meyer, "Interband cascade laser emitting at $\lambda = 3.75$ μm in continuous wave above room temperature," Appl. Phys. Lett. **92**, 191110 (2008).

[26] W. W. Bewley, C. L. Canedy, C. S. Kim, M. Kim, C. D. Merritt, J. Abell, I. Vurgaftman, and J. R. Keyer, "Continuous-wave interband cascade lasers operating above room temperature at $\lambda = 4.7$-5.6 μm," Opt. Express **20**, 3235-3240 (2012).

[27] A. Fiore, V. Berger, E. Rosencher, P. Bravetti, N. Laurent, and J. Nagle, "Phase-matched mid-infrared difference frequency generation in GaAs-based waveguides," Appl. Phys. Lett. **71**, 3622-3624 (1997).

[28] J. B. Khurgin, M. W. Pruessner, T. H. Stievater, and W. S. Rabinovich, "Suspended AlGaAs waveguides for tunable difference frequency generation in mid-infrared," Opt. Lett. **33**, 2904-2906 (2008).

[29] L. Goldberg, W. K. Burns, and R. W. McElhanon, "Difference-frequency generation of tunable mid-infrared radiation in bulk periodically poled $LiNbO_3$," Opt. Lett. **20**, 1280-1282 (1995).

[30] O. Tadanaga, T.Yanagawa, Y. Nishida, H. Miyazawa, K. Magari, M. Asobe, and H. Suzuki, "Efficient 3-μm difference frequency generation using direct-bonded quasi-phase-matched $LiNbO_3$ ridge waveguides," Appl. Phys. Lett. **88**, 061101 (2006).

[31] M. Asobe, O. Tadanaga, T. Yanagawa, T. Umeki, Y. Nishida, and H. Suzuki, "High-power mid-infrared wavelength generation using difference frequency generation in damage-resistant Zn:$LiNbO_3$ waveguide," Electron. Lett. **44**, 288 (2008).

[32] K. F. Buchter, H. Herrmann, C. Langrock, M. M. Fejer, and W. Sohler, "All-optical Ti:PPLN wavelength conversion modules for free-space optical transmission links in the mid-infrared," Opt. Lett. **34**, 470-472 (2009).

[33] W. Chen, J. Cousin, E. Poullet, J. Burie, D. Boucher, X. Gao, M. W. Sigrist, and F. K. Tittel, "Continuous-wave mid-infrared laser sources based on difference frequency generation," C. R. Phys. **8**, 1129 (2007).

[34] T. Hastings, M. H. Lim, J. G. Goodberlet, and H. I. Smith, "Optical waveguides with apodized sidewall gratings via spatial-phase-locked electron-beam lithography," J. Vac. Sci. Technol. B **20**, 2753-2757 (2002).

[35] X. Wang, S. Grist, J. Flueckiger, N. A.F. Jaeger, and L. Chrostowski, "Silicon photonic slot waveguide Bragg gratings and resonators," Opt. Express **21**, 19029-19039 (2013).

[36] X. Wang, W. Shi, H. Yun, S. Grist, N. A.F. Jaeger, and L. Chrostowski, "Narrow-band waveguide Bragg gratings on SOI wafers with CMOS-compatible fabrication process," Opt. Express **20**, 15547-15558 (2012).

[37] M. Belt, J. Bovington, R. Moreira, J. F. Bauters, M. J.R. Heck, J. S. Barton, J. E. Bowers, and D. Blumenthal, "Sidewall gratings in ultra-low-loss Si_3N_4 planar waveguides," Opt. Express **21**, 1181-1188 (2013).

[38] L. Zhu, Y. Huang, W. M.J. Green, and A. Yariv, "Polymeric multi-channel bandpass filters in phase-shifted Bragg waveguide gratings by direct electron beam writing," Opt. Express **12**, 6372-6376 (2004).

[39] F. Prieto, B. Sepulveda, A. Calle, A. Llobera, C. Dominguez, A. Abad, A. Montoya, and L. M. Lechuga, "An integrated optical interferometric nanodevice based on silicon technology for biosensor applications," Nanotechnology **14**, 907-912 (2003).

[40] D. Hradetzky, C. Mueller, and H. Reinecke, "Interferometric label-free biomolecular detection system," J. Opt. A: Pure Appl. Opt. **8**, S360-S364 (2006).

[41] J. Homola, "Present and future of surface plasmon resonance biosensors," Anal. Bioanal. Chem. **377**, 528-539 (2003).

[42] P. P. P. Debackere, S. Scheerlinck, P. Bienstman, and R. Baets, "Surface plasmon interferometer in silicon-on-insulator: novel concept for an integrated biosensor," Opt. Express **14**, 7063–7072 (2006).

[43] R. Magnusson, D. Wawro, S. Zimmerman, Y. Ding, M. Shokooh-Saremi, K. J. Lee, D. Ussery, S. Kim, and S. H. Song, "Leaky mode resonance photonics: technology for biosensors, optical components, MEMS, and plasmonics," Proc. SPIE **7604**, 76040M (2010).

[44] D. D. Wawro, S. Tibuleac, R. Magnusson, and H. Liu, "Optical fiber endface biosensor based on resonances in dielectric waveguide gratings," Proc. SPIE **3911**, 86-94 (2000).

[45] H. Kikuta, N. Maegawa, A. Mizutani, K. Iwata, and H. Toyota, "Refractive index sensor with a guided-mode resonant grating filter," Proc. SPIE **4416**, 219-222 (2001).

[46] Y. Huang, G. Pandraud, and P. M. Sarro, "Reflectance-based two-dimensional TiO_2 photonic crystal liquid sensors," Opt. Lett. **37**, 3162-3164 (2012).

[47] V. M. N. Passaro, R. Loiacono, G. D'Amico, and F. De Leonardis, "Design of Bragg grating sensors based on submicrometer optical rib waveguides in SOI," IEEE Sensors J. **8**, 1603-1611 (2008).

[48] P. Prahbathan, V. M. Murukeshan, Z. Jing, and P. V. Ramana, "Compact SOI nanowire refractive index sensor using phase shifted Bragg gratings," Opt. Express **17**, 15330-15341 (2009).

[49] A. Yalcin, K. C. Popat, J. C. Aldridge, T. A. A. Desai, J. Hryniewicz, N. Chbouki, B. E. Little, O. King, V. Van, S. Chu, D. Gill, M. A. Washburn, M. S. Unlu, and B. B. Goldberg, "Optical sensing of biomolecules using microring resonators," IEEE J. Sel. Top. Quantum Electron. **12**, 148-155 (2006).

[50] C. Y. Chao, W. Fung, and L. J. Guo, "Polymer microring resonators for biochemical sensing applications," IEEE J. Sel. Top. Quantum Electron. **12**, 134-142 (2006).

[51] K. De Vos, I. Bartolozzi, E. Schacht, P. Bienstman, and R. Baets, "Silicon-on-insulator microring resonator for sensitive and label-free biosensing," Opt. Express **15**, 7610-7615 (2007).

[52] V. R. Almeida, Q. F. Xu, A. Barrios, and M. Lipson, "Guiding and confining light in void nanostructure," Opt. Lett. **29**, 1209-1211 (2004).

[53] T. Fujisawa and M. Koshiba, "Guided modes of nonlinear slot waveguides," IEEE Photon. Technol. Lett. **18**, 1530-1532 (2006).

[54] Z. Zheng, M. Iqbal, and J. Liu, "Dispersion characteristics of SOI-based slot optical waveguides," Opt. Commun. **281**, 5151-5155 (2008).

[55] T. Fujisawa and M. Koshiba, "Polarization-independent optical directional coupler based on slot waveguides," Opt. Lett. **31**, 56-68 (2006).

[56] T. Baehr-Jones, M. Hochberg, G. Wang, R. Lawson, Y. Liao, P. A. Sullivan, L. Dalton, A. K.-Y. Jen, and A. Scherer, "Optical modulation and detection in slotted silicon waveguides," Opt. Express **13**, 5216-5226 (2005).

[57] C. A. Barrios, "High-performance all-optical silicon micro switch," Electron. Lett. **40**, 862-863 (2004).

[58] C. A. Barrios and M. Lipson, "Electrically driven silicon resonant light emitting device based on slot-waveguide," Opt. Express **13**, 10092-10101 (2005).

[59] T. Baehr-Jones, M. Hochberg, C. Walker, and A. Scherer, "High-Q optical resonators in silicon-on-insulator-based slot waveguides," Appl. Phys. Lett. **86**, 081101 (2005).

[60] F. D. Olio and V. M. N. Passaro, "Optical sensing by optimized silicon slot waveguides," Opt. Express **15**, 4977-4993 (2007).

[61] H. Sun, A. Chen, and L. R. Dalton, "Multiple slot waveguides for enhanced biochemical sensing," in IEEE/LEOS International Conference on Optical MEMS and Nanophotonics, 21-22 (2009).

[62] A. Kargar and H. Guo, "Optical surface sensing by bent slot waveguide," in Proceedings of the 5th IEEE International Conference on Nano/Micro Engineered and Molecular Systems, 306-308 (2010).

[63] C. A. Barrios, K. B. Gylfason, B. Sanchez, A. Griol, H. Sohlstrom, M. Holgado, and R. Casquel, "Slot-waveguide biochemical sensor," Opt. Lett. **32**, 3080-3082, (2007).

[64] T. Claes, J. C. Molera, K. D. Vos, E. Schacht, R. Baets, and P. Bienstman, "Label-free biosensing with a slot-waveguide-based ring resonator in silicon on insulator," IEEE Photon. J. **1**, 197-204 (2009).

[65] J. T. Robinson, L. Chen, and M. Lipson, "On-chip gas detection in silicon optical microcavities," Opt. Express **16**, 4296-4301 (2008).

[66] C. F. Carlborg, K. B. Cylfason, A. Kazmierczak, F. Dortu, P. M. J. Bañuls, C. A. Maquieira, G. M. Kresbach, H. Sohlström, T. Moh, L. Vivien, J. Popplewell, G. Ronan, C. A. Barrios, G. Stemme, and W. van der Wijngaart, "A packaged optical slot waveguide ring resonator sensor array for multiplex label-free assays in labs-on-chips," Lab Chip **10**, 281-290 (2010).

[67] A. Ikhlef, R. Hedara, and M. Chikh-Bled, "Uniform fiber Bragg grating modeling and simulation used matrix transfer method," Int. J. Comput. Sci. **9**, 368-374 (2012).

[68] K. Zinoviev, L. G. Garrascosa, J. S. Rio, B. Sepulveda, C. Dominguez, and M. Lechuga, "Silicon photonic biosensors for lab-on-a-chip applications," Adv. Opt. Technol. **2008**, 383927 (2008).

[69] D. J. Griffiths, *Introduction to Electrodynamics*, 4th edition (Addison-Wesley, 2012).

[70] Link: http://refractiveindex.info/

[71] X. Xia, Y. Zhou, and C. K. Madsen, "Analysis of As_2S_3-Ti:$LiNbO_3$ taper couplers using supermode theory," Opt. Photon. J. **2**, 344-351 (2012).

[72] Link: http://en.wikipedia.org/wiki/Transfer-matrix_method_(optics)

[73] H. Nishihara, M. Haruna, and T. Suhara, *Optical Integrated Circuits, McGraw-Hill Optical and Electro-optical Engineering Series* (McGraw-Hill Book Company, New York, 1987).

[74] Link: http://www.jeol.co.jp/en/science/eb.html

[75] X. Xia, "Arsenic trisulfide on lithium niobate devices for infrared integrated optics," PhD dissertation, Texas A&M University, College Station, TX, 2011.

[76] J. L. Jackel, V. Ramaswamy, and S. P. Lyman, "Elimination of out-diffused surface guiding in titanium-diffused $LiNbO_3$," Appl. Phys. Lett. **38**, 509-511 (1981).

[77] S. Forouhar, G. E. Betts, and W. S.C. Chang, "Effects of water vapor on modes in Ti-indiffused $LiNbO_3$ planar waveguides," Appl. Phys. Lett. **45**, 207-209 (1984).

[78] G. Griffiths and R. Esdaile, "Analysis of titanium diffused planar optical waveguides in lithium niobate," IEEE Quant. Electron. J. **20**, 149-159 (1984).

[79] Y. Ruan, W. Li, R. Jarvis, N. Madsen, A. Rode, and B. Luther-Davies, "Fabrication and characterization of low loss rib chalcogenide waveguides made by dry etching," Opt. Express **12**, 5140-5145 (2004).

[80] S. Ramachandran and S. G. Bishop, "Low loss photoinduced waveguides in rapid thermally annealed films of chalcogenide glasses," Appl. Phys. Lett. **74**, 13-15 (1999).

[81] C. Tsay, Y. Zha, and C. B. Arnold, "Solution-processed chalcogenide glass for integrated single-mode mid-infrared waveguides," Opt. Express **18**, 26744-26753 (2010).

[82] T. Han, S. Madden, D. Bulla, and B. Luther-Davies, "Low loss chalcogenide glass waveguides by thermal nano-imprint lithography," Opt. Express **18**, 19286-19291 (2010).

[83] C. Vieu, F. Carcenac, A. Pepin, Y. Chen, M. Mejias, A. Lebib, L. Manin-Ferlazzo, L. Couraud, and H. Launois, "Electron beam lithography: resolution limits and applications," Appl. Surface Science **164**, 111-117 (2000).

[84] D. N. Nikogosyan, *Nonlinear Optical Crystals: A Complete Survey* (Springer, New York, 2005).

[85] V. R. Almeida, X. Qianfan, C. A. Barrios, and M. Lipson, "Guiding and confining light in void nanostructure," Opt. Lett. **29**, 1209-1211 (2004).

[86] Y. R. Shen, *the Principles of Nonlinear Optics* (John Wiley & Sons, New York, 1984).

[87] T. Chen, J. Sun, L. Li, and J, Tang, "Proposal for efficient Terahertz-wave difference frequency generation in an AlGaAs photonic crystal waveguide," IEEE J. of Lightwave Technol. **30**, 2156-2162 (2012).

[88] W. C. Tan, M. E. Solmaz, J. Gardner, R. Atkins, "Optical characterization of a-As_2S_3 thin films prepared by magnetron sputtering," J. of Appl. Phys. **107**, 033524 (2010).

[89] E. Yamazaki, A. Takada, T. Morioka, "Noise figure of parametric wavelength conversion with quasi-phase-matched $LiNbO_3$ waveguide," IEEE J. Sel. Top. Quantum Electron. **12**, 536-543 (2006).

[90] R. Ding, T. Baehr-Jones, W. J. Kim, X. Xiong, R. Bojko, J. M. Fedeli, M. Fournier, and M. Hochberg, "Low-loss strip-loaded slot waveguides in silicon-on-insulator," Opt. Express **18**, 25061-25067 (2010).

[91] T. H. Stievater, R. Mahon, D. Park, W. S. Rabinovich, M. W. Pruessner, J. B. Khurgin, and C. J. K. Richardson, "Mid-infrared difference-frequency generation in suspended GaAs waveguides," Opt. Lett. **39**, 945-948 (2014).

[92] D. F. Logan, M. Giguere, A. Villeneuve, and A. S. Helmy, "Widely tunable mid-infrared generation via frequency conversion in semiconductor waveguides," Opt. Lett. **38**, 4457-4460 (2013).

[93] P. Abolghasem, D. Kang, D. F. Logan, M. Lungwitz, and A. S. Helmy, "Widely tunable frequency conversion in monolithic semiconductor waveguides at 2.4 μm," Opt. Lett. **39**, 3591-3594 (2014).

[94] P. Prabhathan, V. M. Murukeshan, and Z. Jing, "Compact resonant Bragg grating filters using submicron silicon-on-insulator (SOI) waveguide for optical communication network," Proc. SPIE **7847**, 74870H (2010).

[95] H.-C. Kim, K. Ikeda, and Y. Fainman, "Tunable transmission resonant filter and modulator with vertical gratings," J. Lightwave Technol. **25**, 1147-1151 (2007).

[96] H.-C. Kim, K. Ikeda, and Y. Fainman, "Resonant waveguide device with vertical gratings," Opt. Lett. **32**, 539-541 (2007).

[97] A. Lupu, K. Muhieddine, E. Cassan, and J.-M. Lourtioz, "Dual transmission band Bragg grating assisted asymmetric directional couplers," Opt. Express **19**, 1246-1259 (2011).

[98] A. Yariv, and A. P. Yeh, *Photonics: optical electronics in modern communications,* 6th edition (Oxford University Press, New York, 2007).

[99] L. Pierno, M. Dispenza, A. Secchi, A. Fiorello, and V. Foglietti, "A lithium niobate electro-optic tunable Bragg filter fabricated by electron beam lithography," J. Opt. A: Pure Appl. Opt. **10**, 064017 (2008).

[100] J. Kim, D. B. Adams, and C. K. Madsen, "Device-under-test Jones matrix extraction algorithm with device TE/TM reference frame," IEEE Photon. Technol. Lett. **24**, 88-90 (2012).

[101] A. Canciamilla, F. Morichetti, S. Grillanda, P. Velha, M. Sorel, V. Singh, A. Agarwal, L. C. Kimerling, and A. Melloni, "Photo-induced trimming of chalcogenide-assisted silicon waveguides," Opt. Express **20**, 15807-15817 (2012).

[102] J. Sun, Purnawirman, E. S. Hosseini, J. D.B. Bradley, T. N. Adam, G. Leake, D. Coolbaugh, and M. R. Watts, "Uniformly spaced λ/4-shifted Bragg grating array with wafer-scale CMOS-compatible process," Opt. Lett. **38**, 4002-4004 (2013).

[103] M. J. Strain, S. Thomas, D. S. MacIntyre, and M. Sorel, "Multi-wavelength filters in silicon using superposition sidewall Bragg grating devices," Opt. Lett. **39**, 413-416 (2014).

[104] D. Marcuse, *Light Transmission Optics* (Van Nostrand Reinhold, New York, 1982).

[105] X. Wang, S. Grist, J. Flueckiger, N. A. F. Jaeger, and L. Chrostowski, "Silicon photonic slot waveguide Bragg gratings and resonators," Opt. Express **21**, 19029-19039 (2013).

[106] R. Ding, T. Baehr-Jones, Woo-Joong Kim, X. Xiong R. Bojko, Jean-Marc Fedeli, M. Fournier, and M. Hochberg, "Low-loss strip-loaded slot waveguides in silicon-on-insulator," Opt. Express **18**, 25061-25067 (2010).

APPENDIX A

SHADOW MASK DEPOSITION ASSEMBLY

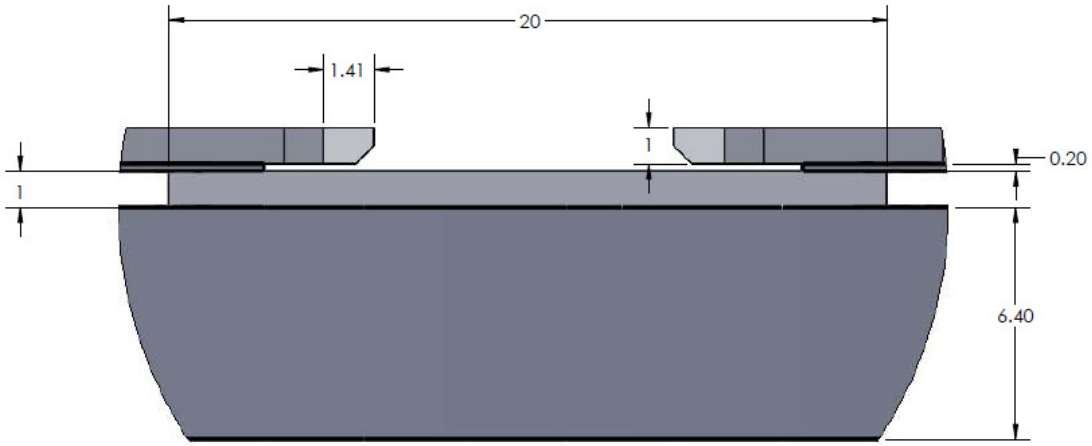

DETAIL A
SCALE 8 : 1

SPACER GEOMETRY

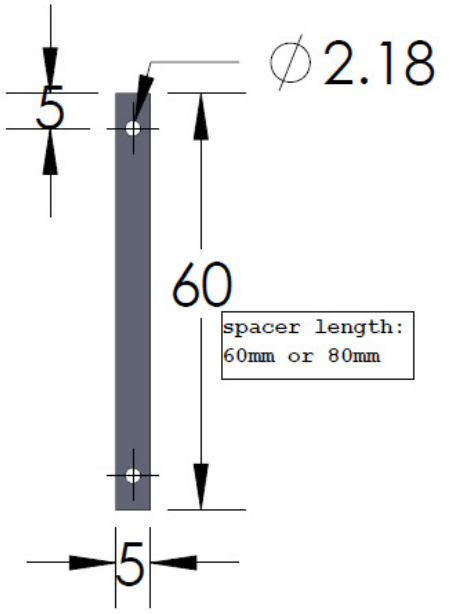

SPACER		
Material: Teflon or Peek		
#	Length	Thickness
2x	60mm	0.1mm
2x	60mm	0.2mm
2x	80mm	0.1mm
2x	80mm	0.2mm

SHADOW MASK GEOMETRY

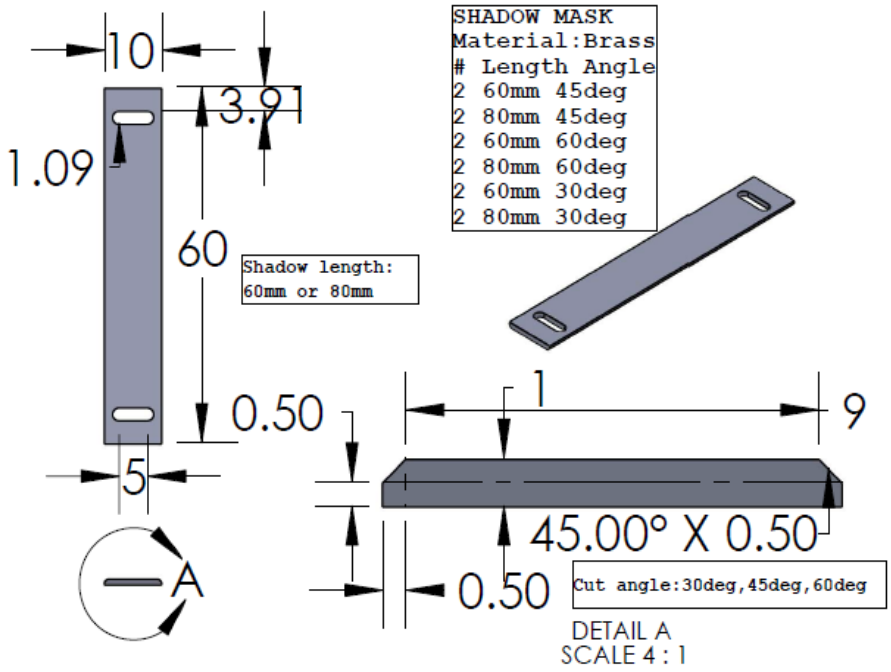

WAFER HOLDER GEOMETRY